

Design strategies and application of stimuli-responsive nanoparticles for cancer diagnosis and therapy

by

Ramesh Marasini

B.Sc., Tribhuvan University, Nepal, 2009

M.Sc., Tribhuvan University, Nepal, 2013

AN ABSTRACT OF A DISSERTATION

Submitted in partial fulfillment of the requirements for the degree

DOCTOR OF PHILOSOPHY

Department of Chemistry
College of Arts and Sciences

KANSAS STATE UNIVERSITY
Manhattan, Kansas

2020

Abstract

Small molecule anticancer drugs are the first-line therapy used in clinical cancer management which has shown success in the killing of rapidly dividing cancer cells. However, nonspecific distribution of these small molecular therapeutics has adverse side effects reducing the quality of life. Therefore, in the past few decades, massive interest and investment have been given in cancer nanomedicine with the hope to reduce drug-associated toxicity by targeting cancer cells in a heterogeneous tumor environment. Nanomedicine is the drug-containing nanostructured construct with a large surface-to-volume ratio, which has plenty of room to load drugs and other necessary constituents to design it as target-specific. Towards the endeavor of precise anticancer drug delivery to tumors, significant efforts have been given to obtain an optimized nanocarrier system to co-operate or bypass biological barriers further advancing the therapeutic and diagnostic efficiency of drugs. The main objective of this dissertation is to explore the different strategies of nanomaterials for drug delivery *via* light-triggered and magnet sensitive design considerations discussed in **chapter 1**. The synthesized nanomaterials were extensively studied and evaluated for their chemistry and biological functions for *in vitro* cancer therapy and *in vivo* diagnosis. In **chapter 2**, we developed the optimum surfactant packing strategy for light-responsive gold nanoparticles (NPs) for photothermal therapy (PTT) of melanoma. Results showed that 5 kDa polyethylene glycol (PEG) coated gold nanorod provided the highest colloidal stability and maximum photothermal efficiency compared to the low (2 kDa) and high mass of PEG (10 kDa) used when treated with near-infrared (NIR) laser. Taking one step further, in **chapter 3**, we encapsulated NIR light-responsive indocyanine class of dye (IR-820) into polymeric NPs for the PTT of breast cancer. The optical properties of dye were preserved to obtain better photothermal efficiency than free IR-820 at an equivalent concentration of dye after laser treatment. Moreover, the molecular mechanism of PTT revealed that the dye loaded NPs induced

cell death primarily through apoptosis, a preferred cell-death pathway over necrosis. In **chapter 4**, we designed peptide conjugated lipid-polymer NPs for p32 targeted drug delivery and tracked NIR dye-labeled NPs *in vivo* using an optical imaging system. The targeted NPs were accumulated 2-fold higher than non-targeted counterparts in the murine osteosarcoma model suggesting the diagnostic potential of targeted NPs. In **chapter 5**, we developed magnet responsive iron chelated paramagnetic polymeric NPs with high colloidal stability and longitudinal relaxivity of $10.5 \text{ mM}^{-1}\text{s}^{-1}$ as compared to the Magnevist[®] $3.98 \text{ mM}^{-1}\text{s}^{-1}$ (a clinical gadolinium contrast agent) and enhanced contrast efficacy *in vivo* at clinical magnetic resonance imaging (3 T) system showing its promise as a blood pool contrast agent in disease detection. The nanoconstructs described herein addresses the current limitations of conventional nanoparticles *via* different design considerations. The significant findings such as targeted drug delivery with improved therapeutic and diagnostic efficacy of each system are highlighted and discussed throughout the dissertation. These results could open the avenues for systemic investigations and lay the foundation for the design of cancer nanomedicine to accelerate clinical translation.

Design strategies and application of stimuli-responsive nanoparticles for cancer diagnosis and therapy

by

Ramesh Marasini

B.Sc., Tribhuvan University, Nepal, 2009

M.Sc., Tribhuvan University, Nepal, 2013

A DISSERTATION

submitted in partial fulfillment of the requirements for the degree

DOCTOR OF PHILOSOPHY

Department of Chemistry
College of Arts and Sciences

KANSAS STATE UNIVERSITY
Manhattan, Kansas

2020

Approved by:

Major Professor
Prof. Santosh Aryal

Copyright

©Ramesh Marasini 2020.

Abstract

Small molecule anticancer drugs are the first-line therapy used in clinical cancer management which has shown success in the killing of rapidly dividing cancer cells. However, nonspecific distribution of these small molecular therapeutics has adverse side effects reducing the quality of life. Therefore, in the past few decades, massive interest and investment have been given in cancer nanomedicine with the hope to reduce drug-associated toxicity by targeting cancer cells in a heterogeneous tumor environment. Nanomedicine is the drug-containing nanostructured construct with a large surface-to-volume ratio, which has plenty of room to load drugs and other necessary constituents to design it as target-specific. Towards the endeavor of precise anticancer drug delivery to tumors, significant efforts have been given to obtain an optimized nanocarrier system to co-operate or bypass biological barriers further advancing the therapeutic and diagnostic efficiency of drugs. The main objective of this dissertation is to explore the different strategies of nanomaterials for drug delivery *via* light-triggered and magnet sensitive design considerations discussed in **chapter 1**. The synthesized nanomaterials were extensively studied and evaluated for their chemistry and biological functions for *in vitro* cancer therapy and *in vivo* diagnosis. In **chapter 2**, we developed the optimum surfactant packing strategy for light-responsive gold nanoparticles (NPs) for photothermal therapy (PTT) of melanoma. Results showed that 5 kDa polyethylene glycol (PEG) coated gold nanorod provided the highest colloidal stability and maximum photothermal efficiency compared to the low (2 kDa) and high mass of PEG (10 kDa) used when treated with near-infrared (NIR) laser. Taking one step further, in **chapter 3**, we encapsulated NIR light-responsive indocyanine class of dye (IR-820) into polymeric NPs for the PTT of breast cancer. The optical properties of dye were preserved to obtain better photothermal efficiency than free IR-820 at an equivalent concentration of dye after laser treatment. Moreover, the molecular mechanism of PTT revealed that the dye loaded NPs induced

cell death primarily through apoptosis, a preferred cell-death pathway over necrosis. In **chapter 4**, we designed peptide conjugated lipid-polymer NPs for p32 targeted drug delivery and tracked NIR dye-labeled NPs *in vivo* using an optical imaging system. The targeted NPs were accumulated 2-fold higher than non-targeted counterparts in the murine osteosarcoma model suggesting the diagnostic potential of targeted NPs. In **chapter 5**, we developed magnet responsive iron chelated paramagnetic polymeric NPs with high colloidal stability and longitudinal relaxivity of $10.5 \text{ mM}^{-1}\text{s}^{-1}$ as compared to the Magnevist[®] $3.98 \text{ mM}^{-1}\text{s}^{-1}$ (a clinical gadolinium contrast agent) and enhanced contrast efficacy *in vivo* at clinical magnetic resonance imaging (3 T) system showing its promise as a blood pool contrast agent in disease detection. The nanoconstructs described herein addresses the current limitations of conventional nanoparticles *via* different design considerations. The significant findings such as targeted drug delivery with improved therapeutic and diagnostic efficacy of each system are highlighted and discussed throughout the dissertation. These results could open the avenues for systemic investigations and lay the foundation for the design of cancer nanomedicine to accelerate clinical translation.

Table of Contents

Table of Contents	viii
List of Figures	xii
List of Tables	xiv
Acknowledgments.....	xv
Dedication	xvii
Chapter 1 - Introduction.....	1
1.1 History of nanotechnology.....	1
1.2 Use of nanotechnology in medicine.....	3
1.2.1 Nanomaterials in therapeutics	3
1.2.2 Nanomaterials in diagnostic imaging.....	4
1.3 Challenges of nanomaterials for clinical translation.....	6
1.3.1 Nanomaterials properties	6
1.3.2 Biological complexity for drug delivery	7
1.3.2.1 Formation of protein corona and reticuloendothelial system sequestration.....	7
1.2.2.2 Complex tumor-microenvironment	8
1.2.2.3 Intracellular environment	10
1.3.3 Reproducibility and scale-up production	11
1.4 Scope of the dissertation	12
1.4.1 Central objective	13
1.4.2 Photoresponsive nanomaterials	13
1.4.3 Magnet-responsive nanomaterials.....	14
Chapter 2 - The influence of polyethylene glycol passivation on the surface plasmon resonance induced photothermal properties of gold nanorods	15
2.1 Introduction.....	16
2.2 Experimental Section	19
2.2.1 Chemicals and cell lines.....	19
2.2.2 Synthesis of AuNR	19
2.2.3 Surface functionalization of AuNRs	20
2.2.4 Characterization of functionalized AuNRs	21

2.2.5 NIR photothermal efficiency	22
2.2.6 Molecular dynamics simulations	22
2.2.6.1 Molecular models.....	24
2.2.6.2 Molecular dynamics methods	25
2.3 Results and Discussion	26
2.3.1 Synthesis and surface functionalization of gold nanorods.....	26
2.3.2 Characterization of functionalized AuNRs	26
2.3.3 NIR photothermal efficiency	28
2.3.4. Thermal conductivity calculations	31
2.3.5 Cellular uptake study	33
2.3.6 NIR mediated phototoxicity study	35
2.4 Conclusion	36
Chapter 3 - Indocyanine-type infrared-820 encapsulated polymeric nanoparticle assisted photothermal therapy of cancer	38
3.1 Introduction.....	39
3.2 Materials and Methods.....	41
3.2.1 Chemicals and reagents.....	41
3.2.2 Preparation of IR-820 encapsulated nanoparticles.....	42
3.2.3 Characterization of nanoparticles.....	43
3.2.4 Cellular biocompatibility and NIR mediated phototoxicity study	46
3.2.5 Intracellular uptake study.....	47
3.2.6 Investigation of the mechanism of cell death induced by PTT	48
3.2.7 Data and statistical analysis.	49
3.3 Results and Discussions	49
3.3.1 Physiochemical characterization.....	49
3.3.2 IR-820 mediated photothermal efficiency	52
3.3.3 Biocompatibility and cellular internalization study.....	54
3.3.4 NIR mediated phototoxicity study	55
3.3.5 Evaluation of mechanism for IR-820 PLGA NPs induced phototoxicity.....	57
3.4 Conclusion	59

Chapter 4 - Synthesis and characterization of a tumor-seeking LyP-1 peptide integrated lipid– polymer composite nanoparticle.....	60
4.1 Introduction.....	61
4.2 Materials and Methods.....	63
4.2.1 Chemicals and reagents.....	63
4.2.2 Cell lines and animal tumor model	64
4.2.3 Synthesis of LyP-1 conjugated lipid	64
4.2.4 Preparation of LyP-1 conjugated lipid-polymer composite nanoparticles.....	65
4.2.5 Characterization of nanoparticles.....	66
4.2.6 Drug loading and release study.....	67
4.2.7 Cellular biocompatibility and cytotoxicity study.....	68
4.2.8 Intracellular uptake study.....	69
4.2.9 Fluorescence-activated cell Sorting (FACs) study.....	69
4.2.10 Biodistribution and <i>in vivo</i> imaging.....	70
4.2.11 Data and statistical analysis	71
4.3 Results and Discussion	71
4.3.1 Chemical characterization of LyP-1 lipid	71
4.3.2 Physiochemical characterization of NPs.....	72
4.3.3 Biocompatibility Study.	75
4.3.4 Cellular cytotoxicity study.....	76
4.3.5 Cellular uptake studies	77
4.3.6 <i>In-vivo</i> biodistribution study	80
4.4 Conclusion	84
Chapter 5 - Iron (III) chelated paramagnetic polymeric nanoparticle as next-generation T ₁ - weighted MRI contrast agent.....	85
5.1 Introduction.....	86
5.2 Materials and Methods.....	89
5.2.1 Material and chemical.....	89
5.2.2 Cell line and animal model	89
5.2.3 Preparation of paramagnetic polymeric nanoparticles.....	90
5.2.4 Characterization of Fe-PLGA	90

5.2.5 MRI phantom study of Fe-PLGA	92
5.2.6 <i>In vitro</i> biocompatibility study.....	93
5.2.7 <i>In vitro</i> cellular uptake study	93
5.2.8 <i>In vivo</i> MRI study	94
5.3 Result and Discussion	94
5.3.1 Limitations of currently used CAs in medical imaging	94
5.3.2 Morphology, size, and charge distribution of Fe-PLGA NPs.....	95
5.3.3 Ferric chloride loading and release study	96
5.3.4 <i>In vitro</i> cellular interaction study	100
5.3.5 Assessment of magnetic properties <i>in vitro</i>	101
5.3.6 <i>In vivo</i> vascular imaging	104
5.4 Conclusion	106
Chapter 6 - Summary and Outlook	107
References.....	109
Appendix A - Supporting information from Chapter 2	130
Appendix B - Supporting information from Chapter 4.....	131
Appendix C - Supporting information from Chapter 5.....	133
Appendix D - List of abbreviation	134
Appendix E - List of publications.....	137
Appendix F - Copyright permissions.....	138

List of Figures

Figure 1.1 Timeline showing the development of nanotechnology.....	2
Figure 2.2 Timeline showing the development of nanomedicine.....	5
Figure 1.3 Schematic showing the physiology of solid tumor encompassing with fibroblast, stromal cells, and the gradient of oxygen level along with necrotic and hypoxic regions ...	11
Figure 1.4 Scope of the dissertation to develop nanomaterials for cancer diagnosis and therapy	12
Figure 2.1 Schematic showing the effect of surface passivation of gold nanorod with PEG molecules of various molecular mass (2, 5, 10 kDa) on plasmonic heating.....	18
Figure 2.2 Schematic showing the synthesis and surface passivation of gold nanorod with PEG molecules of various molecular mass	21
Figure 2.3 Physiochemical characterization of AuNRs before and after surface functionalization	27
Figure 2.4 Photothermal properties of raw and PEG-functionalized AuNRs.....	29
Figure 2.5 LSPR response and alteration in the AuNR aspect ratio after NIR exposure of raw and PEG passivated AuNRs	30
Figure 2.6 Molecular dynamics simulation of heat conduction through PEG brushes	33
Figure 2.7 Cellular uptake efficiency of Raw and PEG-functionalized AuNRs with mouse melanoma cell line	34
Figure 2.8 <i>In vitro</i> photothermal effect of raw and PEG-functionalized AuNRs against the B16-F10 cells	36
Figure 3.1 Morphology, size, and photostability of IR-820-PLGA NPs.....	50
Figure 3.2 IR-820 loading and release study	52
Figure 3.3 Comparative photothermal efficiency of free IR-820 dye and IR-820 PLGA NPs	53
Figure 3.4 Optical response and alteration in the size of IR-820 PLGA NPs after laser exposure	54
Figure 3.5 Cellular interaction study in MCF-7 cells	56
Figure 3.6 NIR mediated phototoxicity study and its mechanism of cell death in MCF-7 cells..	58
Figure 4.1 Graphical representation of DSPE-PEG and LyP-1 conjugate synthesis and NPs fabrication process.	65
Figure 4.2 Chemical characterization of synthesized LyP-1-DSPE-PEG.	73

Figure 4.3 Physiochemical characterization, drug loading, and release study of NPs	74
Figure 4.4 Stability study of drug and dye.....	75
Figure 4.5 Comparative cellular interaction study of control NP and LyP-1 NP against mouse fibroblast (NIH/3T3) and osteosarcoma (K7M2) cells.....	78
Figure 4.6 Cellular internalization study in cancerous and non-cancerous cells.....	79
Figure 4.7 Fluorescent activated cell sorting (FACS) experiment for quantification of internalized NPs	81
Figure 4.8 <i>In-vivo</i> biodistribution of NPs using fluorescence imaging	83
Figure 5.1 Physiochemical characterization of iron (III) chelated polymeric NPs	97
Figure 5.2 Stability and loading/release study of iron (III) chelated polymeric NPs	99
Figure 5.3 Oxidation of ascorbic acid catalyzed by Fe ³⁺	100
Figure 5.4 <i>In vitro</i> biocompatibility studies and cellular uptake study.....	102
Figure 5.5 Relaxivity study of iron (III) chelated polymeric NPs in the low and ultra-high magnetic fields.....	103
Figure 5.6 <i>In vivo</i> time-dependent T ₁ weighted magnetic resonance image of mice at 3 T.....	105

List of Tables

Table 2.1. Thermal conductivity calculation in molecular dynamics simulations for PEG brushes of different PEG molecular masses and chain densities on a gold surface.....	32
Table 5.1. Composition of simulated body fluid in order of mixing reagents. Samples A–C are prepared under ambient conditions while samples D–F at 37 °C while stirring.	92

Acknowledgments

Thanks to everyone who supported my academic journey including my high school teachers, advisors, administrators, friends, and family members. Thanks for your love and support throughout this journey from Gulmi to Palpa, Gulmi to Kathmandu, and Gulmi to Kansas, USA. You all wonderful souls are deeply acknowledged.

During the time of my Ph.D. studies, I have received excellent help and support from numerous people, including my colleagues in the lab, Chemistry Department, and the staff at the NICKS. Especially, I would like to express my sincere gratitude to my Advisor, Dr. Santosh Aryal, who has guided me throughout my work. Your support and guidance have been held near and dear since the first day in Manhattan. By providing a friendly and informal atmosphere, you made hard work seem much easy. I owe much of my confidence to you. You allowed me to blossom into my best self and I could not be more grateful. From the bottom of my heart, Thank you!

I would also like to thank my current and previous committee members: Dr. Stefan Bossmann, Dr. Christine Aikens, Dr. Robert DeLong, and Dr. Emily McLauren for their continued support and suggestions throughout the duration of my graduate career. Thank you, Dr. Mark Haub, for being the chairperson of my defense.

I am grateful to Professor Jeff Comer at NICKS for his encouragement and enthusiasm to support me as a trainee. It was always a real pleasure working with him. His input regarding the molecular aspects of laser treatment, including excellent scrutinizing of manuscripts, has been invaluable. Dr. Mark Weiss, Department of Anatomy and Physiology for friendship and fruitful collaboration in stem cell work, Professor David Biller, Department of Radiology, for facilitating to use of clinical MRI.

With the most sincerity, I would like to acknowledge the past and current members of the Aryal group- Dr. Arunkumar Pitchaimani, Dr. Tuyen Nguyen, Mukund Koirala, Soma Sekhar Sriadibhatla, Sagar Rayamajhi, Colin Ferrel, Jessica Marchitto, Cesar Aparicio, and Layah Johnsosn. You have been like family to me and I always look forward to seeing you. Thank you, everyone, for being a part of my Ph.D. journey and making every moment of graduate school so special. I am thankful to have all of you around.

My profound gratitude and deep appreciation for my family. Mom and Dad, you have given me a lifetime of encouragement, unconditional love, and your sacrifice to educate me. Thank you for never doubting my potential and sticking with me through the many crazy years of school! To my beloved brother Madan for your love and support. An overwhelming amount of gratitude must be given to my loving friend, Pratikshya. I will be forever grateful for the countless hours you have listened to me practice presentations, talk about my hurdles at work, and calmed my nerves. Without your support, this work would never have been accomplished. Thank you for consistently giving motivation and courage to push boundries. Most importantly, I am thankful to Eric, who has given a new dimension to my life. It is amazing what a smile can do to you!

Dedication

This thesis is dedicated to my parents

Lekhnath Marasini and Laxmi Marasini

One day I hope to be as calm as buwa (dad) when things don't quite go to plan

and

To my advisor

Dr. Santosh Aryal

Without whom this day would never come.

Chapter 1 - Introduction

1.1 History of nanotechnology

The term ‘nanotechnology’ covers the discipline that has very old historic roots from ancient roman civilization dating from the 5th century using the ‘Lycurgus Cup’, Chinese porcelain also known as ‘Famille Rose’ to the microstructure of wootz steel used in ‘Khukuri’ or ‘Damascus’ blades (made from wrought iron along with charcoal and additives like glass, woods, etc.) in ancient Indo-continental region.¹⁻⁵ Similarly, altering the size of gold and silver particles created colors in the stained glass windows visible in churches produced during medieval times.⁶⁻⁹ On the other hand, Charak Samhita is the oldest Ayurvedic epic in the Indo-continental region that describes the use of minted novel metals with the paste of traditional medicine for the treatment of human diseases.^{2,5,10,11} The concept of breaking down of particle size is well documented in Charak Samhita for metals or nonmetals.¹² The creators back then just did not know that the process they used to make beautiful items led to a change in the composition of the materials that they were working with. Therefore, nanotechnologies are around us in history (**Figure 1.1**).

The word ‘nano’ was derived from the Greek word meaning ‘dwarf’ or something very small depicting today’s one thousand millionths of a meter (10^{-9} m) size. The nanometer (nm) size can be compared with a single human hair that is about 100,000 nm thickness and the deoxyribonucleic acid (DNA) double helix has a radius of 1nm. The modern nanoscience can be defined as the branch of science that study structures and molecules on the scale of subnanometer from 1-100 nm and technology that uses a structural arrangement of atoms or molecules to particular applications, for example, medicines or devices is called nanotechnology. According to the Encyclopedia of Britannica, ‘nanotechnology is the manipulation, and manufacture of materials and devices on the scale of atoms or small groups of atoms.’¹³ According to the National Nanotechnology Initiative

of the United States, ‘nanotechnology is a science, engineering, and technology conducted at the nanoscale (1-100 nm), where unique phenomena enable novel applications in a wide range of fields, from chemistry, physics and biology, to medicine, engineering, and electronics.’¹

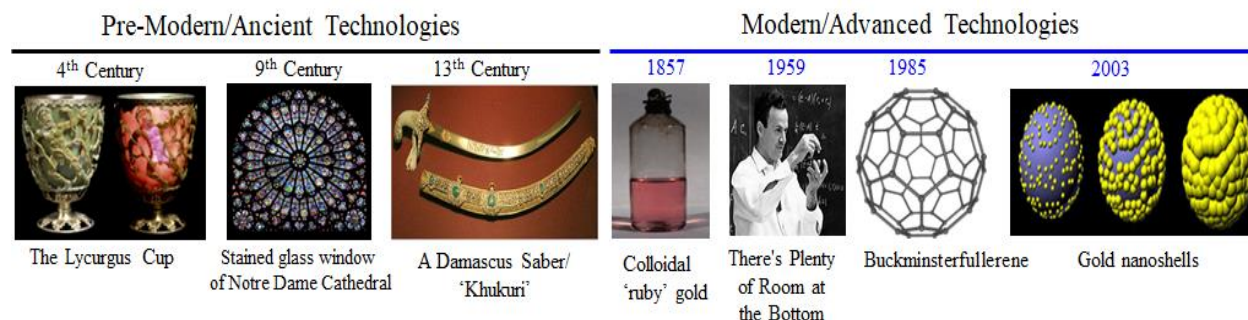


Figure 1.1 Timeline showing the development of nanotechnology (ref 1, 2, 4, 5)

The modern era of nanotechnology began with the knowledge of colloidal Rubby gold by Michael Faraday showing nanostructured gold when shine with light produces different-colored solutions.¹⁴ The modern concept behind nanoscience began with the pioneer physicist Richard P. Feynman's speech entitled ‘There’s Plenty of Room at the Bottom’ on December 26, 1959, during the American Physical Society meeting at Caltech where he discussed the concept of manipulating matter at the atomic level.¹⁵ This novel idea opened up new means of rational and Feynman’s hypotheses have since been proved. It was further developed with the first use of the ‘nanotechnology’ word by scientist Norio Taniguchi while describing the semiconductor processes that occurred approximately a nanometer (**Figure 1.1**). Due to the convergence of experimental advances in the development of the scanning tunneling microscope in 1981 and the discovery of fullerenes in 1985, the rocket rate growth of nanoscience and nanotechnology is exponential with about 1300 nanotech products available now for the public.¹ Therefore, findings and results from nano-research significantly influence our living conditions and the culture of our society. What is researched in the laboratory today could completely reshape our everyday lives tomorrow.

1.2 Use of nanotechnology in medicine

Nanotechnology holds great promise to convert nanoscience theory to applications creating new materials with improved properties by controlling, assembling, measuring, and manufacturing materials at the nanometer scale.¹⁶ The use of nanotechnology in medicine where the material in sub 100 nm are investigated for possible preventive, diagnostic, and therapeutic applications is called ‘nanomedicine’. The ability to tune the size to nanoscale and manipulating individual atoms and molecules opens new avenues for exceptional properties of materials at the molecular level. The most significant feature of nanomedicine is its flexibility of surface modification, due to large surface-to-volume ratio, with a variety of ligands (peptide, small molecule, nucleic acids, antibodies), large room to incorporate payloads (both water-soluble and –insoluble), the know-how of tuning pharmacokinetics and pharmacodynamics of active ingredient, and the platform for combining diagnostics with therapy in a single session. Varieties of organic (polymers, peptides, nucleic acids) and inorganic (iron, gold, silver, carbon) based nanomaterials have been extensively explored as nanomedicine for disease diagnosis, treatment, or combination of both.^{17–21}

1.2.1 Nanomaterials in therapeutics

The biomedical application of nanoparticles (NPs) started with the use of nanoconjugates after the discovery of immunogold labeling in the 1970s.²² Subsequently, several NPs have paved their way broadening the medical tools and techniques for the prevention, monitoring, control, and treatment of disease in the clinics. Many nanomaterials are showing promising candidacy for their successful clinical translation because of (1) controlled and flexible physicochemical properties (size, shape, material, density, and surface charge), (2) protect the active ingredient from degradation while traveling in the body, and (3) be able to deliver its cargo precisely to the site of action while avoiding off-target effects. Therefore, the use of a nano-sized delivery device provides

an innovative means of transportation for small molecule free drugs to pass through the complex biological system and overcome the limitations of conventional formulations. With the aforementioned benefits, the era of clinical use of nanomedicine began in 1995. The first nanomedicine called DOXIL[®] was approved by the United States Food and Drug Administration Agency (US-FDA) which is composed of polyethylene glycol (PEG) containing liposomal doxorubicin (DOX). The active component of DOXIL[®] is DOX, a clinical anticancer drug, loaded into the liposomal core. The use of DOXIL[®] in cancer treatment has shown significant improvement over small molecule free DOX by suppressing toxicities and extending the overall pharmacokinetic profile. For example, in the case of DOXIL[®] when free DOX is crystallized and enveloped in a liposomal lipid bilayer vesicle with PEG decorated outside, the circulation half-life increases from 5 mins to 55 h.²³ Followed by DOXIL[®], several other nanomedicines containing protein (Abraxane[®]), lipid (Abelcet[®]), polymer (Eligard[®]), crystal (Tricor[®]), viral (Gendicine[®]), nucleic acid (Onpatro[®]), and inorganic components (Feridex[®]) were successfully translated to the clinics.²⁴ So far, more than 70 nanomedicines, either diagnostic or therapeutics, have been developed and commercially available for various disease management globally. Recent data shows more than 50 nanomedicines were approved within the USA along with hundreds of other nanoformulations entering various stages of clinical developments (**Figure 1.2**).²⁴⁻²⁶

1.2.2 Nanomaterials in diagnostic imaging

Diagnostic medical imaging has become an essential tool to identify disease pathology based on anatomical or functional evaluations. With the increasing need for diagnostic imaging in disease management, imaging modalities in current use include X-ray radiography, computed tomography (CT), positron emission tomography (PET), magnetic resonance imaging (MRI),

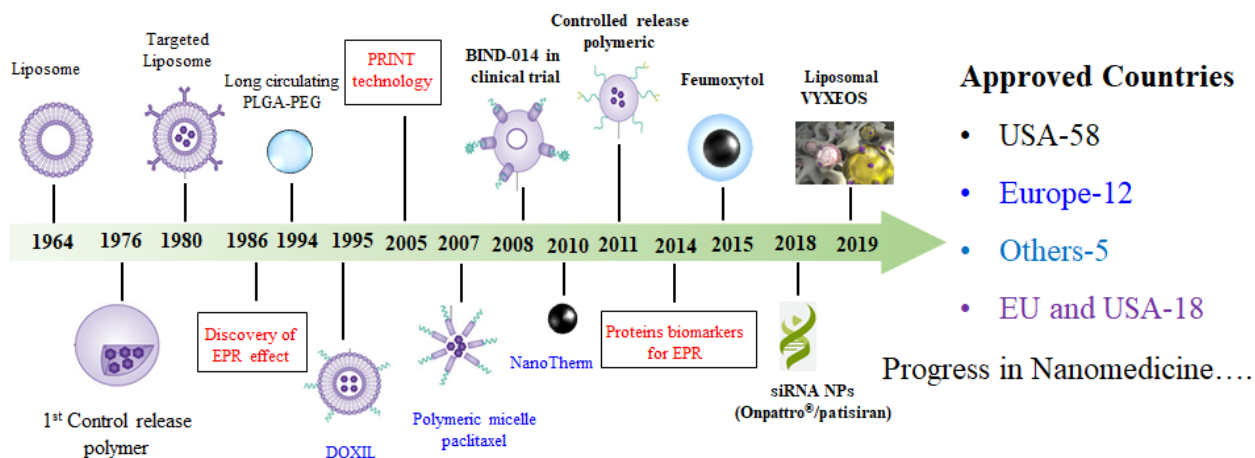


Figure 2.2 Timeline showing the development of nanomedicine (ref 19, 20, 21)

single-photon emission computed tomography (SPECT), optical imaging, and ultrasound.²⁷ To improve lesion detection, more than one imaging modality is routinely used for clinical analysis and medical intervention. To enhance the efficiency of imaging modalities, small molecules and molecular complexes are used as probes or contrast agents. These imaging probes or contrast agents are employed to assist for a better visualization of abnormality allowing the diagnosis of previously undetectable pathologies of the traditional imaging techniques. The advantages of using imaging probes are further advanced by incorporating into nanomaterials with the hope of improvement in sensitivity, stability, and plasma residence times as compared to the small molecules counterparts that exhibit fast metabolism and have non-specific distribution, and potential undesirable toxicities. The incorporation of a small-molecule probe into nanomaterials have stimulated the efforts in improving disease detection and imaging due to unique passive, active, and physical targeting properties. Nanodiagnostic agents have been used in cancer detection, enzyme activity evaluation, instant/in-situ cell labeling and tracking, lymph node detection, and monitoring therapeutic response.²⁸⁻³¹ Compared with small molecule contrast agents, nanodiagnostic agents offer surface labeling with specific ligands to improve the toxicity

profile and imaging properties.^{30,32–34} Additional benefits of nanoparticle imaging include functional visualization and monitoring of biological processes, such as macrophage detection in atherosclerotic lesions using CT, and molecular imaging of angiogenesis by MRI.³⁵ Furthermore, the longer plasma residence time of nanoparticles improve biodistribution with a greater lesion to background contrast signal.^{36,37} For example, Pitchaimani et al. have significantly improved the plasma retention time of gadolinium-based contrast agents (GBCAs) when encapsulated into liposome up to 11.6 h compared to a few minutes of clinical small molecule GBCAs.³⁶ This improvement provides a sufficient diagnostic window for the radiologist to detect the lesions. Additionally, the shape and size of the nanoparticles can be manipulated to optimize the loading of imaging agents, and their inherent physical properties can also be changed to meet disease-specific needs.³⁸

1.3 Challenges of nanomaterials for clinical translation

1.3.1 Nanomaterials properties

Many nanomaterials are showing promising candidacy for their successful clinical translation because of several attractive features: (i) small dimensions (1–200 nm), (ii) controlled and flexible physicochemical properties (size, shape, material, density, and surface charge), (iii) strong affinity for target recognition, and (iv) high payload delivery with the potential for combinatorial delivery (imaging probe, dual drugs).^{17,39–46} The size of nanomaterials is advantageous as it is sufficiently large to carry much more payload localizing at the desired location than a small molecule while retaining the ability to travel through the bloodstream, unlike much larger structures. Additionally, they offer the ability to selectively enter into the desired location, for example, tumors more specifically than molecular agents or larger particles such as microparticles because of leaky vasculature *via* enhanced permeability and retention effect (EPR).

Indeed, EPR can provide nanomaterials access to a disease site, which can then allow binding to diseased cells.

Nanomaterials that are being developed for clinical translation usually display several potential qualities that solely depend on their physicochemical properties. Bio-nano interaction place a crucial role in determining the fate of nanoparticles *in-vitro* and *in-vivo*. From the outset in nanomedicine development, it is important to consider the relationship between disease pathophysiology and the heterogeneity of the disease and the importance of physicochemical characteristics of different nanomaterials (shape, size, charge) under investigation to overcome complex biological barriers to enable improved targeting to diseased tissue and/or reduced accumulation in non-target organs.

1.3.2 Biological complexity for drug delivery

1.3.2.1 Formation of protein corona and reticuloendothelial system sequestration

Despite their promising results in the preclinical animal models, the therapeutic impact of nanomedicine in cancer often fail in the clinical trials. This failure rate could be attributed to the poor design, the complexity of the biological environment, and the lack of relevant preclinical animal models. Nanomedicine upon administration immediately encounters immune cells leading to the opsonization and the formation of the protein corona.⁴⁷ As a result of these interactions, the designed and expected properties of the nanomedicine are changed inside complex body biology. However, the extent and constituents of proteins corona depend on the fundamental physicochemical properties of nanoparticles such as shape, size, and surface chemistry employed with the involvement of the common proteins including complement proteins, serum albumin, apolipoproteins, and antibodies. Because of protein corona formation, the expression of ligands on the surface of nanoparticles is masked rather than their pristine surface and therefore alters its

pharmacokinetic profile. Salvati et al. have reported that when a transferrin receptor targeting ligand (transferrin) functionalized silica nanoparticle was used to study the targeting efficiency toward lung cancer cell, the result showed that no matter if polyethylene glycol, a biocompatible polymer that is believed to minimize the formation of the protein corona, was used or not, the targeting specificity of nanoparticle formulations was lost upon the exposure to biological serum.⁴⁸ This unwanted corona formation brings significant changes to the synthetic characteristics of nanomedicine. Thus, the unforeseen biological process leads to the sequestration of nanomedicine after recognition by macrophages and scavenger endothelial cells of the reticuloendothelial system. The sequestration results in a high accumulation of nanomedicine in organs such as the liver and spleen, unfortunately, preventing the journey of nanomedicine to reach to the targeted location. More than 31.30% of targeted and 62.33% non-targeted gold nanoparticles (55nm) intravenously injected dose were found in reticuloendothelial system organs such as the liver and spleen.⁴⁹ With this extensive hindrance and excretion, as reported in a meta-analysis demonstrating that about 1% of the total dose administered actually reaches the target tissue.^{50,51} On the other hand, opsonization is more problematic for diagnostic nanomedicine because of signal quenching effect in optical imaging,^{52,53} and reducing the relaxivity of MRI contrast agents due to transmetallation with endogenous ions present in the body.^{54,55}

1.2.2.2 Complex tumor-microenvironment

The solid tumor mass consists of a heterogeneous population of cancer cells along with a variety of resident and infiltrating host cells, secreted factors, and extracellular matrix proteins collectively forming tumor microenvironment (TME).⁵⁶ Such complex cellular networks and distinct physiological conditions such as a lowered interstitial pH, a higher glutathione concentration, interstitial pressure gradients, or an increased level of certain enzymes such as

matrix metalloproteinases. This unique cellular and physiological condition of the tumor (**Figure 1.3**) makes it very difficult to deliver drugs into the cancer cells, which is why about 0.7- 1% of the injected dose is reported to be delivered to the tumor from metadata analysis.²⁵ However, there is some debate among scientists in the way how to best interpret the delivery of nanoparticles to the solid tumor. Recently, Price et al. revisited the meta-analysis of data collected by Wilhelm et al. and found that when standard pharmacokinetics, by using the ratio of area under the curve in the tumor (AUC_{tumor})/area under the curve of blood (AUC_{blood}) are used to assess nanoparticles tumor delivery, was about 100-fold greater as compared to the traditional approach of nanoparticles percentage injected dose (%ID) used by Wilhelm et al.^{50,57}

Tumor-associated cellular heterogeneity: The dense network of tumor-associated cells surrounds the actual tumor cell making highly challenging for the extravasation of nanomedicine. In a study conducted by Kano et al. demonstrated only the minimal benefit of liposomal doxorubicin (DOXIL[®]) in a pancreatic cancer-bearing rodent model.⁵⁸ However, Carbal et al. showed that when DOXIL[®] is used in combination with transforming growth factor- β (TGF- β) signaling inhibitor that resulted significantly increased penetration, accumulation, and antitumor efficiency in a murine pancreatic tumor model.⁵⁹ On the other hand, tumor-associated immune cells including T-cell, B-cell, natural killer cell, macrophages, dendritic cells, and neutrophils play a crucial role in carcinogenesis and cancer progression while actively involved for degrading nanomedicines before it reaches to the cancer cells. Therefore, Dai et al. have reported that 90% of intratumoral nanoparticles were found to be residing in tumor-associated macrophages leading to just 0.001%-0.003% nanoparticle injected dose found in cancer cells of human ovarian SKOV-3 xenograft mouse model.⁴⁹

Complex tumor physiology: Physical and chemical features of TME such as low pH, hypoxia, high interstitial pressure, and fibrosis are also critical players.⁶⁰ These factors are thoroughly linked to every step in the progression, metastasis, and metabolism of tumors. Changes in the complex TME are always in a dynamic process and provide augmented growth for tumor progression and therapeutic resistance. For example, the acidic pH of the tumor extracellular matrix compared to the pH in normal tissues creates a gradient of pH which limits the delivery of payload by altering the charge present in the carrier and drug. Similarly, abnormal vasculature builds an aggressive TME with hypoxia (a pathological condition depicting the oxygen gradient) and altered interstitial fluid pressure.^{61,62} The high interstitial fluid pressure in the TME is considered as the crucial barrier in solid tumors that can obstruct payload delivery to tumors. Consequently, these cells become more aggressive and resistance to therapies.^{61,63,64}

1.2.2.3 Intracellular environment

The safe journey of nanomedicine inside cells is a key step to its success, considering nanocarriers are intended to deliver specific molecules (drugs and contrast agents) to the cytosol, nucleus, or other specific intracellular sites.⁶⁵⁻⁶⁷ The fate of nanoparticles into cells is cell types dependent and mainly governed by the non-specific or specific/receptor-mediated binding manner. Subsequently, bound nanoparticles trigger the cellular endocytic pathway for nanoparticle's efficient and controlled trafficking into cell crossing cell membranes into specialized intracellular compartments mediated mainly by a network of cellular endosomes along with the Golgi apparatus, endoplasmic reticulum, and lysosomes.⁶⁸ During this process, the nanoparticles get trapped in the acidic endosomal compartments (pH~5-6) and then continue to fuse to the lysosome where the pH further drops to ~4.5 and the presence of enzymes begin to act on nanoparticle's digestion and degradation.⁶⁹ As a result, the active payload is also degraded with its carrier before reaching the site of action.

Tumor microenvironment

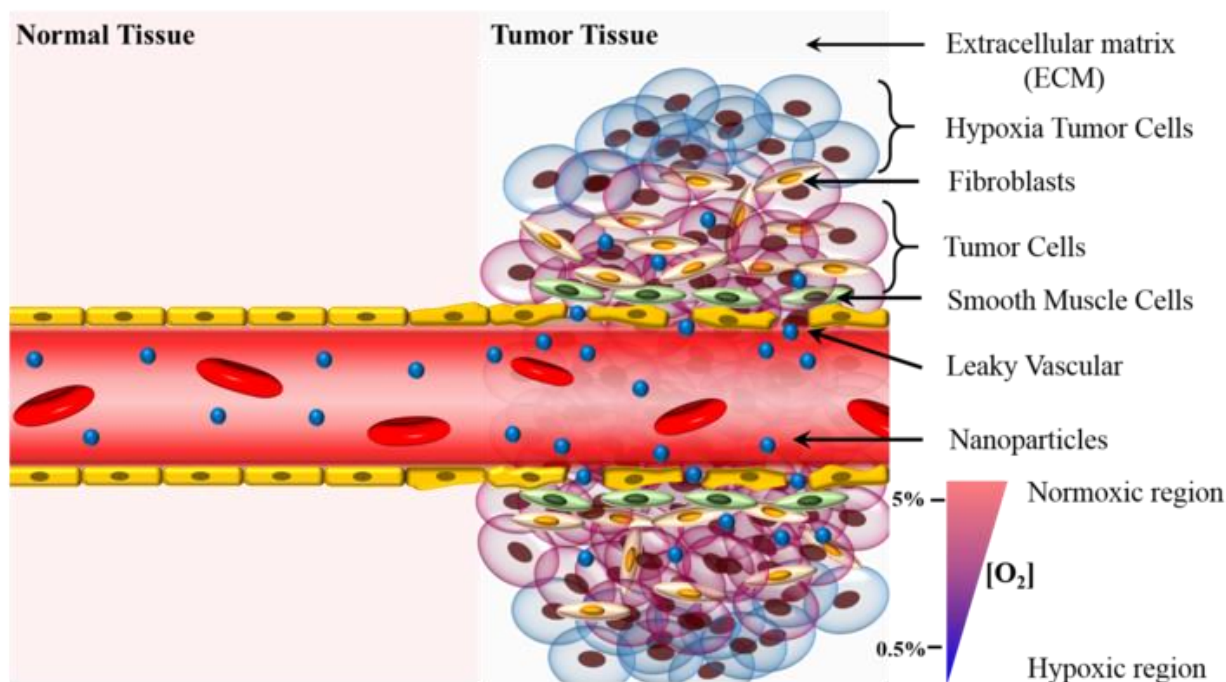


Figure 1.3 Schematic showing the physiology of solid tumor encompassing with fibroblast, stromal cells, and the gradient of oxygen level along with necrotic and hypoxic regions. Figure courtesy of Dr. Tuyen Nguyen.

1.3.3 Reproducibility and scale-up production

In the face of the arsenal of nanomedicines currently under preclinical development or various clinical trials, their clinical translations have not progressed as rapidly as the results of the preclinical study would have suggested. The successful translation of nanomedicine is an expensive and long process. As a basic requirement for its clinical translation, the preparation protocol must be feasible for large scale production while consistently maintaining the same high level of quality and batch-to-batch reproducibility to the set specifications. With the addition of more components such as surface modification, targeting motif, imaging agent, and drug in a single formulation (i.e., multifunctional nanomedicine) and multistep production process pose challenges for scale-up production with good manufacturing production, increases the cost of production, and makes the quality control evaluation

of such products more difficult. Therefore, it has been shown in a quadrennial review report published by the National Nanotechnology Initiative showed that 70% of nano-patents are non-reproducible which could be due to the broad composition of matter claims during the patent process and not appreciating the subtleties drug-specific development of nanomedicine.⁷⁰

1.4 Scope of the dissertation

In the past few decades, we observed massive interest and investment in nanomedicine. Over the years, significant efforts have been given to obtain an optimized nanocarrier system to co-operate or bypass biological barriers further advancing the therapeutic and diagnostic efficiency of payload (drugs and imaging agents). Although an extensive amount of research has been dedicated to developing a nanocarrier system, however, only a few of nanomedicine find their way

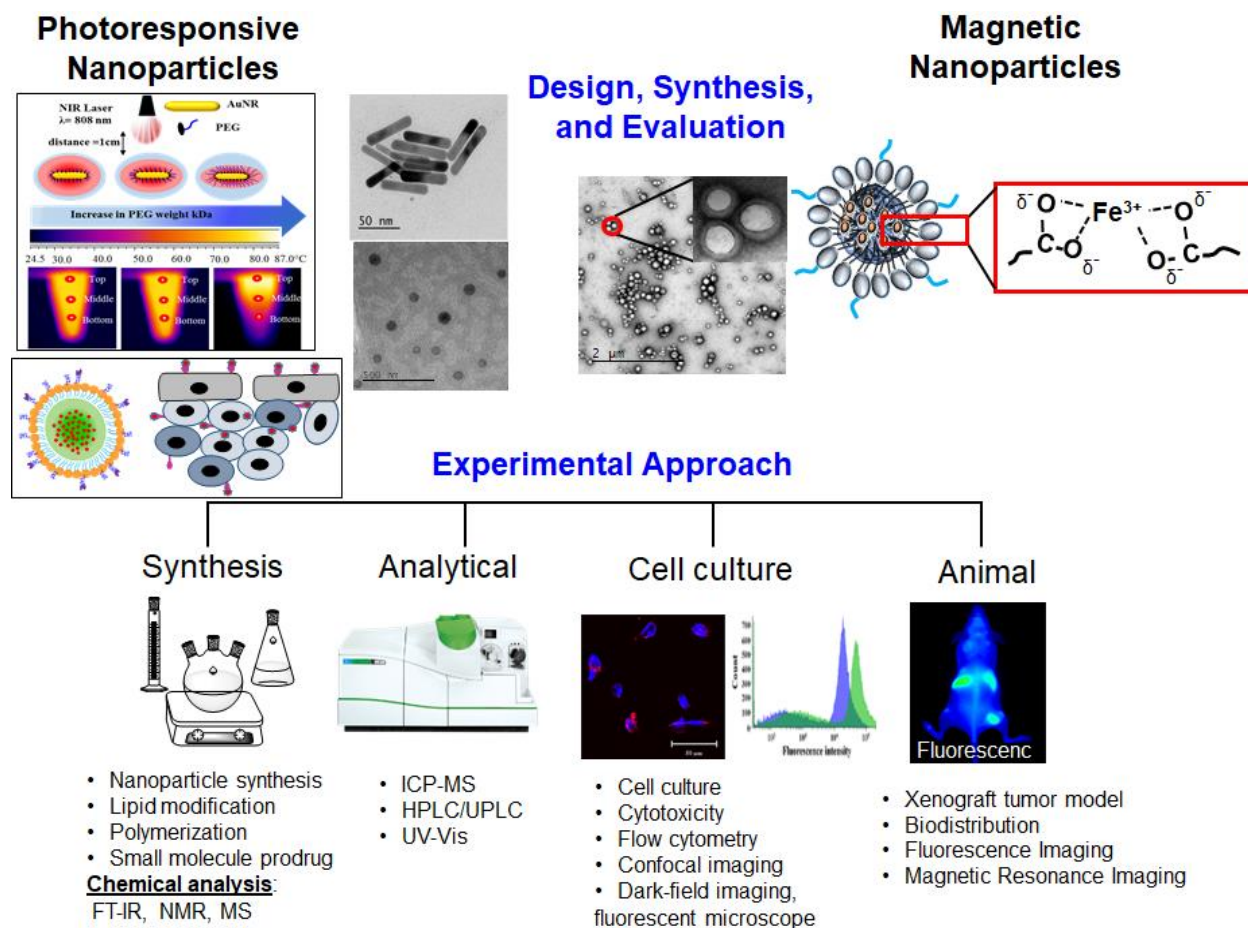


Figure 1.4 Scope of the dissertation to develop nanomaterials for cancer diagnosis and therapy

to the clinic. The lack of sufficient clinical translation of nanomedicine is a direct consequence of the nanoparticle's inability to overcome many of the above-mentioned nanomaterial properties and biological complexity. Integrating quantitative non-invasive imaging techniques in nanomedicine development offers attractive possibilities to address these issues.

1.4.1 Central objective

The main objective of this dissertation is to explore the different strategies of nanomaterials engineering for targeted drug delivery *via* light-triggered and magnet sensitive design (**Figure 1.3**). The designed nanomaterials were extensively studied and evaluated for their biological functions in terms of cancer diagnosis using paramagnetic and fluorescent-labeled nanomaterials and therapy using photoresponsive nanomaterials. *Via* the new design considerations, the nanoconstructs described herein addresses the current limitations of the conventional nanoparticle. The significant findings of each system will be highlighted and discussed throughout this dissertation.

1.4.2 Photoresponsive nanomaterials

Under the photoresponsive nanomaterials, drug delivery systems which are made up of rod-shaped gold nanoparticles decorated peripherally by polyethylene glycol (PEG) sheath was developed (**Chapter 2**). The engineered nanoconstruct exhibited combinatorial actions, upon illumination with NIR laser light, including targeting and therapy for skin cancer. As a one step forward, NIR light-sensitive small-molecule fluorescent probe called IR-820 dye loaded into the core of poly(lactic-co-glycolic acid) (PLGA) nanomaterial was designed for both photothermal and optical imaging to enhance the effectiveness of non-invasive cancer diagnosis and therapy in a single session (**Chapter 3**). This project was further extended to see how the presence of targeting ligand changes the targeting and biodistribution patterns using LyP-1 peptide on the surface while drug as DOX or NIR imaging probe as 1,1'-dioctadecyl-3,3',3'-

tetramethylindotricarbocyanine iodide (DiR) dye was designed. In this approach, a tumor-targeting strategy was used to enhance the accumulation of nanoparticles into the tumor region by receptor-mediated interactions. By conjugating LyP-1 peptide with carboxylated terminated lipid-PEG molecule and loading DiR in the PLGA polymeric core, we successfully tunned the nanomaterial into the tumor region. The tumor region accumulation of engineered nanoconstruct is about three times higher than that of the non-targeted control nanoparticles using tumor-bearing mice model (**Chapter 4**).

1.4.3 Magnet-responsive nanomaterials

On the other hand, under the magnetic responsive nanomaterials, a paramagnetic iron chelated polymeric nanoconstruct was fabricated to enhance bright contrast as a next generation of MRI contrast agents to substitute potentially toxic clinically used gadolinium-based agents for cancer diagnosis. In this approach, the carboxylic acid terminated polymeric nanoparticle surface was chelated with ferric iron (**Chapter 5**). The use of iron to lower down the longitudinal relaxivity of MRI has huge advantages to overcome toxicity associated with Gd-based contrast agents. This study has resulted in an optimized iron chelated polymeric nanoconstruct for tunable longitudinal (T_1) relaxivity performance under *in vitro* and *in vivo* conditions. This strategy allowed to a next-generation contrast agent from the exogenous metal component, resulting in a high longitudinal relaxivity contrast agent for improved MR imaging of disease pathology.

Chapter 2 - The influence of polyethylene glycol passivation on the surface plasmon resonance induced photothermal properties of gold nanorods

*Chapter 2, in full, is a reprint of the material form **Nanoscale**, 2018, DOI: [10.1039/C8NR03026J](https://doi.org/10.1039/C8NR03026J)*

The molecular simulation work presented here was done in collaboration with Dr. Jeff Comer.

Abstract

Gold nanorods (AuNRs) possess unique photothermal properties due to their strong plasmonic absorption in the near-infrared region of the electromagnetic spectrum. They have been explored widely as an alternative or complement to chemotherapy in cancer treatment. However, its use as an injectable medicine is greatly hindered by its stability in biological media. Therefore, studies were focused on improving the stability of AuNRs by introducing biocompatible surface functionalization such as polyethylene glycol (PEG) coatings. However, these coatings can affect heat conduction and alter their photothermal behavior. Herein, we studied how functionalization of AuNRs with PEG chains of different molecular weights determined the temperature distribution of suspensions under near-infrared irradiation, cell uptake *in vitro*, and hyperthermia-induced cytotoxicity. Thermogravimetric analysis of the PEG-conjugated AuNRs exhibited slightly different PEG mass fractions of 12.0%, 12.7%, and 18.5% for PEG chains with molecular weights of 2, 5, and 10 kDa, implying distinct structures for the PEG brushes. When exposed to near-infrared radiation, we found greater temperatures and temperature gradients for longer PEG chains, while rapid aggregation was observed in unmodified (Raw) AuNRs. The effect of the PEG coating on heat transport was investigated using molecular dynamics simulations, which revealed the atomic-scale structure of the PEG brushes and demonstrated lower thermal conductivity for PEG-

coated AuNRs than for unmodified AuNRs. We also characterized the uptake of the AuNRs into mouse melanoma cells *in vitro* and determined their ability to kill these cells when subjected to near-infrared radiation. For all PEG-coated AuNRs, exposure to 10 s of near-infrared radiation significantly reduced cell viability relative to unirradiated controls, with this viability further decreasing with increasing AuNR doses, indicating potential phototherapeutic effects. The 5 kDa PEG coating appeared to yield the best performance, yielding significant phototoxicity at even the lowest dose considered (0.5 $\mu\text{g/mL}$), while also exhibiting high colloidal stability, which could help in rationale design consideration of AuNR for NIR induced photothermal therapy.

2.1 Introduction

Gold nanorods (AuNRs) have the potential to become a powerful tool in bio-imaging, cancer-targeting, and cancer therapy, owing to the ease with which their surface chemistry can be modified and their ability to strongly absorb radiation in various regions of the electromagnetic spectrum.⁷¹⁻⁷⁷ The absorption of near-infrared radiation (NIR) by AuNRs transforms light energy into thermal energy, which has been extensively exploited in hyperthermia-based therapy, so-called photothermal therapy.^{78,79} In the NIR region, specifically at $\lambda=808$ nm, light penetration is optimal due to minimal absorption from tissue chromophores and water. Therefore, surface plasmon resonance (SPR) induced heating is key to clinical therapy applications of AuNR involving superficial tumors, as well as those located deep within the bodily tissue (using optical fibers).^{80,81}

The large optical cross-sections of AuNR with tunable longitudinal surface plasmon resonance (LSPR) in the NIR makes them outstanding agents for photothermal therapy.^{76,79,82,83} Given the large surface-area-to-volume ratio of AuNRs and the strong affinity of sulfur for gold surfaces, AuNRs can be conjugated with biomolecules like proteins, DNA, siRNA, and small-molecule drugs.⁸⁴⁻⁸⁷ Therefore, AuNRs can be engineered to deliver therapeutics and to absorb

NIR radiation for the ablation of tumor cells, also known as cellular hyperthermia.⁸⁸ Selectivity is achieved by directional control or by using fiber optic positioning of the incoming radiation. For a tumor that is deeply situated inside the body, local cellular hyperthermia is achieved by the administration of AuNR and the local application of a pulsed or continuous-wave laser source.^{89–}
⁹⁴ NIR laser pulses absorbed by AuNR excite free electrons in the plasmon band, creating a pulse of hot electrons. The hot electron pulse cools rapidly through electron–phonon interactions by colliding with the gold lattice, heating it to thousands of degrees (depending on laser power) within ~1 ps.⁹⁵ Heat is then transferred from the nanorod to its surroundings through phonon–phonon interactions on a time scale of ~100 ps, resulting in an increase in temperature of the surrounding medium by tens of degrees.^{96–98} The enhanced heat in local tissue surrounding, in turn, causes cell death. This treatment modality, also known as plasmonic photothermal therapy, provides an attractive method for the treatment of solid tumors in a minimally invasive manner.^{24, 25} El-Sayed et al. studied the feasibility of *in vivo* NIR photothermal therapy using AuNRs in mice bearing subcutaneous squamous cell carcinoma xenografts.⁹⁹ AuNRs were conjugated to thiol-terminated polyethylene glycol (PEG-SH) having a molecular mass of 5 kDa to increase biocompatibility, suppress immunogenic responses, and to decrease adsorption to the negatively charged luminal surface of blood vessels. A Greater than 96% decrease in average tumor growth was observed within 13 days.^{100–103} Similarly, using AuNRs functionalized with Arg–Gly–Asp peptides (RGD), studies have demonstrated the inhibition of cancer cell migration by targeting integrins.¹⁰⁴ Although the plasmonic properties of AuNRs have been highly exploited in biomedical research and applications, major concerns for achieving optimum photothermal effects are the colloidal stability of AuNRs in biological media and the blocking of heat transport from the surface of AuNRs to the surrounding medium by thick coatings. Therefore, suitable surface functionalization

is necessary for stable, biocompatible, and long-circulating nanoparticles.^{77,105–107} Preferably, the surface passivating material should first have a strong affinity for the nanoparticle surface and also provide them with tunable chemical functionality, good colloidal stability, and biocompatibility.⁷⁷ PEG is a common material for the passivation of gold nanoparticles in physiological environments, yielding high colloidal stability, biocompatibility, long blood circulation time, and preferential accumulation in tumors.^{99,103,108,109} However, heat transfer from AuNRs induced by NIR radiation is greatly affected by the physical properties of the surface-conjugated material. In particular, PEG passivation heavily influences thermal conductivity at the gold–solvent interface, thereby altering photothermal effects at the macroscopic and microscopic levels.^{110,111} A recent report from C. J. Murphy and coworkers demonstrated a decrease in the thermal conductivity of AuNR coated with the quaternary ammonium surfactant cetyltrimethylammonium bromide (CTAB) when the

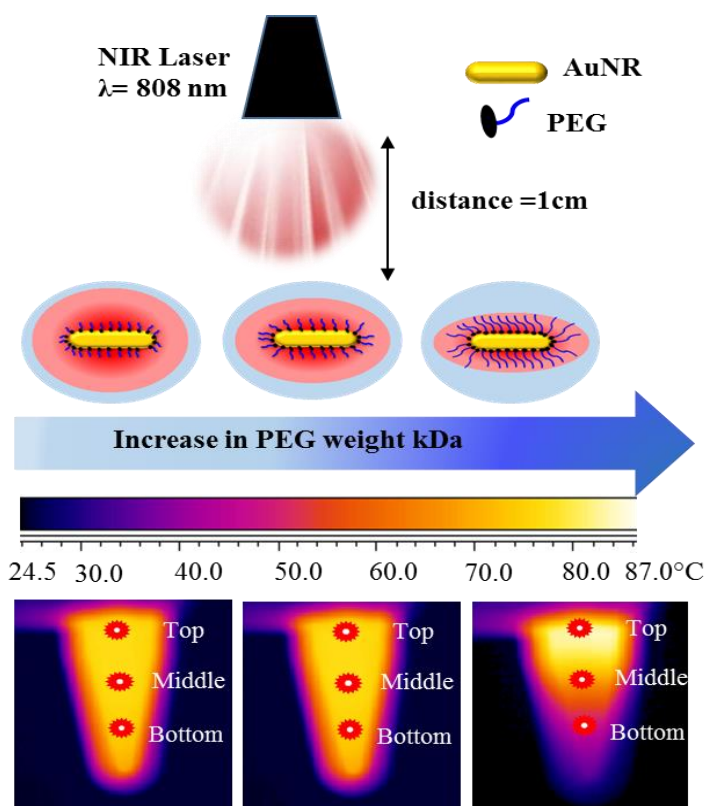


Figure 2.1 Schematic showing the effect of surface passivation of gold nanorod with PEG molecules of various molecular mass (2, 5, 10 kDa) on plasmonic heating

the concentration of the surfactant is above the critical micelle concentration.¹¹² The authors further extended their study by coating the AuNR surface layer-by-layer with polyelectrolytes and found an increase in thermal conductivity and heat capacity. It is clear that optimizing the physical properties of the surface-conjugated ligand is important for the therapeutic outcomes. Herein, we investigated the jacketing effect of the PEG coating on photothermal cell ablation by varying the chain length of PEG conjugated to the surface of AuNR. AuNRs passivated with PEG of different molecular masses (2, 5, and 10 kDa) were studied in detail under NIR irradiation using a diode laser ($\lambda = 808$ nm). Considering the higher NIR exposure for the surface cells versus that for deep tissue, we used a B16-F10 mouse melanoma cell line as an *in vitro* model to evaluate the therapeutic effectiveness of AuNRs.

2.2 Experimental Section

2.2.1 Chemicals and cell lines

Gold (III) chloride trihydrate ($\text{HAuCl}_4 \cdot 3\text{H}_2\text{O}$, 99.99%), cetyl tri-methyl ammonium bromide (CTAB, 99%), sodium borohydride (98%), L-ascorbic acid (99%), silver nitrate (99%), tris-hydrochloride (tris-HCl, 99%), and 3-(4,5-methyl thiazol-2-yl)-2, 5-diphenyltetrazolium bromide (MTT) were purchased from Sigma-Aldrich (Milwaukee, WI, USA). Polyethylene glycol carboxylic thiols (HOOC-PEG-SH) with average molecular masses of 2, 5, and 10 kilodaltons (kDa) were purchased from creative PEGWorks (North Carolina, USA). All other chemicals and reagents were of analytical grade and used as received from Fischer Scientific, USA. The mouse melanoma cell line B16-F10 was procured from ATCC and maintained in Dulbecco's modified Eagle's medium (DMEM) supplemented with 10% (v/v) fetal bovine serum (FBS) and penicillin/streptomycin (100 $\mu\text{g}/\text{mL}$) at 37 °C in a 5% CO_2 environment.

2.2.2 Synthesis of AuNR

NIR responsive AuNRs were synthesized using the seed-mediated growth method as described

previously.^{83,102} In brief, the seed solution was prepared by adding 250 μ L of HAuCl₄ (0.01 M) into 10 mL of CTAB (0.1 M) under stirring. To this solution, 600 μ L of freshly prepared ice-cooled NaBH₄ (0.01 M) was quickly injected and stirred for two minutes. For the growth solution, 2 mL of HAuCl₄ (0.01 M) and 0.4 mL of AgNO₃ (0.01 M) were added to 40 mL of CTAB (0.1 M) solution. The pH of the solution was adjusted to 1.0–2.0 using HCl (1.0 M) and subsequently, 0.32 mL of ascorbic acid (0.1 M) was added to the solution under gentle mixing until the solution turned colorless. To form the AuNRs, 0.096 mL of the aged seed solution (2.5 h) was added to the growth solution under gentle mixing and incubated overnight at 26 °C as shown in **Figure 2.2**. The as-prepared AuNR solution capped with CTAB was stored at 4 °C for further use.

2.2.3 Surface functionalization of AuNRs

Before surface modification, the excess CTAB present in the AuNR was removed by repeated centrifugation at 12,000 rpm for 10 mins. The AuNR pellet was re-dispersed in Mili-Q water and washed two times using the same conditions. After purification, the washed raw AuNR pellets were re-dispersed in 1 mL of tris-HCl (50 mM) (hereafter termed “Raw AuNR”) and subsequently subjected to surface modification with the thiolated PEG (PEG-SH) of different molecular masses. For the process, 1 mL of PEG-SH (2, 5, or 10 kDa) with a concentration of 1 mg/mL dispersed in the 50 mM Tris-HCl buffer (pH = 5) were used to functionalize the surface of purified AuNR (50 mg/mL in PBS) by rotating for 1 hour at room temperature. The resulting AuNRs are hereafter referred to as “AuNR-PEG-2,” “AuNR- PEG- 5,” and “AuNR-PEG-10” as shown in **Figure 2.2**. The number 2, 5, and 10 in the nomenclature of each sample represents the corresponding molecular mass of the surface-conjugated PEG chains in kDa. The excess of unreacted PEG was removed by centrifugation at 12000 rpm for 10 minutes, and the pellet was re-dispersed in 1 \times PBS to make a final volume of 1 mL.

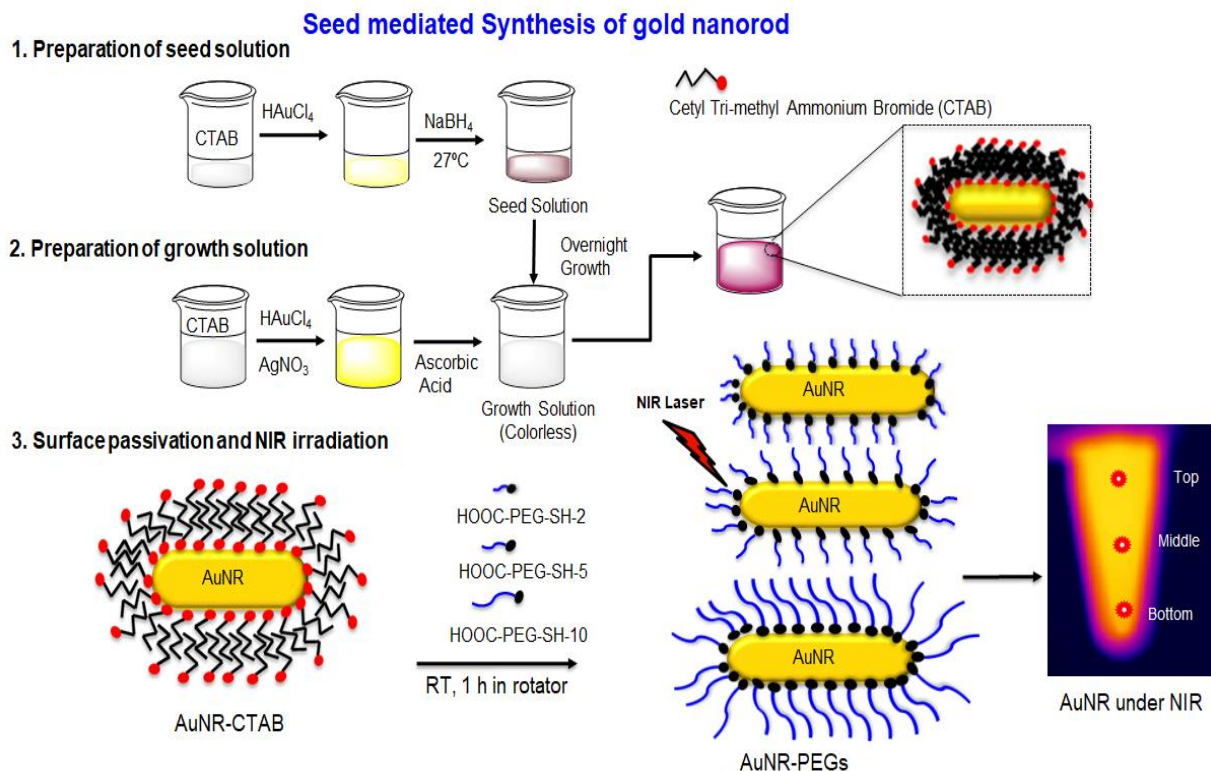


Figure 2.2 Schematic showing the synthesis and surface passivation of gold nanorod with PEG molecules of various molecular mass (2, 5, 10 kDa).

2.2.4 Characterization of functionalized AuNRs

The surface plasmon resonance spectra of the as-prepared and surface modified AuNRs were analyzed using a UV-Vis spectrophotometer (BIOMATE-3S, Thermo Scientific) with 1.0 mm path length quartz cuvettes. The size and surface morphology were analyzed using a transmission electron microscope (FEI Technai G2 spirit Bio TWIN). The concentration of gold in all formulations were determined using inductively coupled plasma-mass spectroscopy (ICP-MS, Perkin Elmer, NEXion 350×) following standard protocol.^{106,113} The hydrodynamic size, surface charge, and zeta potential analysis of the different AuNR formulations were carried out using dynamic light scattering (DLS, Zetasizer Nano ZSP, Malvern, Worcestershire, UK). Fourier transform infrared spectroscopic (FT-IR) analysis was performed to analyze surface chemistry of AuNRs using a Nicolet™ iS™ 50 FT-IR Spectrometer (Thermo Fisher).

2.2.5 NIR photothermal efficiency

The photothermal effects of Raw AuNR and PEGylated AuNRs suspensions were determined in a cell-free environment. Briefly, a fixed concentration of Raw, AuNR-PEG-2, AuNR-PEG-5, and AuNR-PEG-10 (20 $\mu\text{g}/\text{mL}$) was irradiated using a continuous-wave NIR diode laser with a vacuum wavelength of 808 nm (0.6 mm spot focus size, power of $21.1\text{W}/\text{cm}^2$) for 0, 30, 60, 90, and 120 s. The distance of the laser spot and AuNR suspension was maintained 1 cm for all samples (**Figure 2.1**). During the irradiation, the temperature of AuNR suspensions in $1\times$ PBS was monitored by capturing images every 10 seconds using forward-looking Infrared (FLIR) thermal imaging system. For quantitative analysis, ThermoCAMTM Researcher Professional 2.8 SR1 software (FLIR system) was used to record the temperature at three different locations of suspension (top, middle, and bottom) during NIR irradiation demonstrated in **Figure 2.1**.

2.2.6 Molecular dynamics simulations

The molecular models for performing the thermal conductivity calculations were constructed and equilibrated as described in the Supporting Information. Briefly, we created three simulation systems mimicking the Raw AuNR, AuNR-PEG-2, AuNR-PEG-5 materials used the experiments. The numbers of PEG chains per unit area of the gold surface were estimated from the geometry of the AuNRs and the mass fraction of PEG determined by electron microscopy and thermogravimetric analysis, respectively. Atomistic simulations of the AuNR-PEG-10 systems were deemed infeasible due to the size of the simulation system required for properly simulating PEG chains of that length. Each system contained a gold slab¹¹⁴, water, and (except for the Raw system) thiol-terminated PEG chains¹¹⁵ of the appropriate molecular masses (2 or 5 kDa). We did not attempt to model CTAB in the simulation systems since the thermogravimetric analysis showed that the mass fraction of CTAB on the Raw AuNR surfaces was relatively small. All

simulation systems had approximately the same size ($5.1 \times 5.3 \times 17.8 \text{ nm}^3$) after equilibration at 300 K and atmospheric pressure. The thiolated PEG chains were relaxed in 100 ns of simulation using the program NAMD¹¹⁶ with the thiol groups in their reduced form, allowing the brush to self-assemble into a realistic arrangement before the sulfur atoms were fixed to represent covalent attachment. Subsequently, the calculations of thermal conductivity were performed using the molecular simulation program LAMMPS.¹¹⁷ The thermal conductivity through the system was calculated by the algorithm of Müller-Plathe.¹¹⁸ A constant heat current ($2.1\text{--}2.4 \mu\text{W}$) was imposed between the center of the system (where the gold slab was located) and the extreme ends of the system by exchange of kinetic energies every 100 simulation steps. The resulting temperature distribution (considering 20 segments of the system along the z-axis) was measured after the system reached a steady state. Due to limitations of the Müller-Plathe algorithm's implementation in LAMMPS, covalent bonds to hydrogen and water molecules were made flexible during these simulations, requiring a 1 fs time step. The force field parameters used with NAMD were converted to LAMMPS format using a custom script. The simulations were run at constant volume with the overall temperature maintained at 300 K by a Nosé-Hoover thermostat, which was previously shown not to affect the thermal conductivity calculations.¹¹⁸ Each of the simulations was run more than 4 ns, with the convergence of the temperature distribution apparent after 0.5 ns. The thermal conductivity was calculated from the portion of the simulations for $t > 1 \text{ ns}$ by $\lambda = QLz / (4A \Delta T \Delta t)$, where Q is the total thermal energy transferred by the algorithm during the relevant simulation time Δt , Lz is the z dimension of the simulation system (Lz/2 is the distance between the centers of the hot and cold segments), A is the cross-sectional area of the system in the xy plane, and ΔT is the average temperature difference between the hot and cold segments in the steady-state.

2.2.6.1 Molecular models

Three molecular models were created to study the thermal conductivity of the polyethylene glycol (PEG) brushes. Each system was based on a five-layer slab of 1800 gold atoms with lateral dimensions of $5.075 \times 5.274 \text{ nm}^2$. The upper and lower surfaces of the slab consisted of Au {111} crystal facets. The surfaces of the nanorods are expected to be more complex than flat fcc {111} facets; however, the simple Au {111} representation is likely sufficient for the goal of the simulations, namely calculating the thermal conductivity through the PEG brushes. Owing to periodic boundary conditions, the Au {111} surfaces were effectively infinite in extent in the xy plane. Different numbers of thiolated PEG ($\text{CH}_3(\text{OCH}_2\text{CH}_2)_n\text{-SH}$) molecules of different lengths were added for each system as described below. Water molecules were added to both sides of the slab, yielding system dimensions of about 17.8 nm along the z-axis.

System A contained only the gold slab and water, to mimicking the Raw AuNR system. **Systems B and C** were constructed to model the experiments involving thiolated PEG having molecular masses of 2 and 5 kDa, respectively. We placed thiolated PEG molecules, $\text{CH}_3(\text{OCH}_2\text{CH}_2)_n\text{-SH}$ with $n = 45$ and 112 , onto both the upper and lower gold surfaces. The areal density of thiolated PEG chains on the gold surfaces was calculated to approximately reproduce its value in the experiments. The specific surface area of the gold nanorods, $\sigma \approx 20.7 \text{ m}^2/\text{g}$, was estimated from their approximate dimensions (10 nm in diameter, 51 nm in length) and the density of solid gold at standard conditions. The approximate densities of PEG chains were calculated to be $N/A = 1.98$ and 0.86 nm^{-2} for the 2 and 5 kDa PEG systems using the formula $N/A = \alpha / [(1-\alpha)\sigma M]$, where $\alpha = 12\%$ and 12.7% were the mass fractions of PEG in the AuNR as determined by thermogravimetric analysis and $M = 2$ and 5 kDa were the molecular masses of the PEG chains. The PEG molecules were initially oriented so that the thiol groups were only a few ångströms from the gold surface.

2.2.6.2 Molecular dynamics methods

Interatomic interactions with the gold surface were represented according to the GoIP-CHARMM force field,¹¹⁴ which includes virtual surface atoms that favor atom adsorption atop the gold atoms and charged particles rigidly attached to gold atoms that endow polarizability.¹¹⁹ The charge of the latter particles was $0.3e$, while the gold atoms carried charges of $-0.3e$. PEG was represented according to the carefully validated CHARMM model.¹²⁰ The force field parameters of the thiol group were obtained by applying the CHARMM General Force Field (CGenFF) version 3.0.1 web interface to a thiolated PEG molecule and integrating the resulting CGenFF parameters with the CHARMM PEG model.

Equilibration of the simulation systems was performed by the program NAMD 2.12,¹¹⁶ using a 2 fs time step, rigid water molecules,¹²¹ rigid covalent bonds involving hydrogen,¹²² and particle-mesh Ewald electrostatics.¹²³ All atoms of gold remained fixed to their initial positions (an ideal fcc crystal), except for the polarization particles, which were able to rotate about the gold atom centers *via* rigid bonds. The mass of the polarization particles was set to 1.0 Da so that their bonds to the gold atoms would be kept rigid without modification of the NAMD source code. Lennard-Jones forces and direct Coulomb forces have smoothly truncated a distance of 9 to 10 Å. The temperature was maintained at 300 K by a Langevin thermostat. The pressure was maintained at 1.01325 bar by a Langevin piston,¹²⁴ which allowed only the z dimension of the simulation cell to fluctuate. The size of the system in the xy plane remained fixed, consistent with the size of the ideal Au {111} layers. Each system was equilibrated for 100 ns to allow the PEG chains to relax. The PEG chains were initially in a grid arrangement. However, wishing to obtain realistic arrangements of the thiolated PEG chains, we did not covalently attach the thiols to the Au {111} surfaces, but simulated them in their reduced state, permitting slow diffusion of the thiol terminal groups across the surfaces. Nonetheless, all of the PEG

chains remained adhered to the surface by a strong noncovalent thiol–gold interaction.¹¹⁴ The resulting structures had disordered arrangements of PEG chains, presumably more realistic than the initial grid arrangement. The gold slabs were subsequently removed and filled in with additional water. The reason to remove the gold slab was to simplify the thermal conductivity calculations and remove the influence of the thermal conductivity of the gold model because it is unlikely that the fixed gold atoms of the GolP-CHARMM force field accurately represent heat conduction through gold. In all subsequent simulations, the sulfur atoms of the PEG molecules were restrained to their final positions before the gold slab was removed. Each system underwent energy minimization and a further 0.2 ns of equilibration after removal of the gold slab.

2.3 Results and Discussion

2.3.1 Synthesis and surface functionalization of gold nanorods

NIR-responsive AuNRs were synthesized using seed-mediated growth methods.⁸⁵ The formation of AuNR was confirmed by observing its morphology using transmission electron microscopy and reading its longitudinal (LSPR) and transverse surface plasmon resonance (TSPR). The synthesized AuNRs were monodisperse with an aspect ratio of 5.1 ± 0.83 and an average length of 51.2 ± 5.53 nm with a width of 10.02 ± 2.17 nm (**Figure 2.3 A**). The LSPR and TSPR peaks of the as-synthesized AuNRs were found to be 840 nm and 510 nm, respectively. After functionalization with thiolated PEG of different molecular masses, LSPR peaks were found to be 850, 840, and 850 nm for AuNR-PEG-2, AuNR-PEG-5, and AuNR-PEG-10, respectively. Nonetheless, the TSPR peak remained at 510 nm before and after PEGylation (**Figure 2.3 B**).

2.3.2 Characterization of functionalized AuNRs

The surface coating efficiency of PEG onto the AuNRs surfaces was confirmed by

measuring the hydrodynamic diameter using DLS. The hydrodynamic size of the CTAB stabilized AuNR was found to be 50.7 ± 0.2 nm in diameter, which when passivated with PEG reached 79.36 ± 0.14 , 85.0 ± 1.2 , and 80.0 ± 0.13 nm for AuNR-PEG-2, AuNR-PEG-5, and AuNR-PEG-10, respectively (**Figure 2.3 C**). Additionally, the zeta potentials of Raw AuNR changed from positive 53.7 ± 3.5 mV to negative -21.5 ± 0.4 , -24.5 ± 0.5 , and -28.3 ± 0.4 mV for AuNR-PEG-2, AuNR-PEG-5, and AuNR-PEG-10. These changes in zeta potential are indicative of successful surface functionalization (**Figure 2.3 D**). The surface-functionalized PEG shows higher colloidal stability at 4°C over the period (**Appendix A-Figure 2.3 S1**). With PEG modification supported by the DLS and zeta results, we moved to characterize the density of the surface coatings. Thermogravimetric analysis was

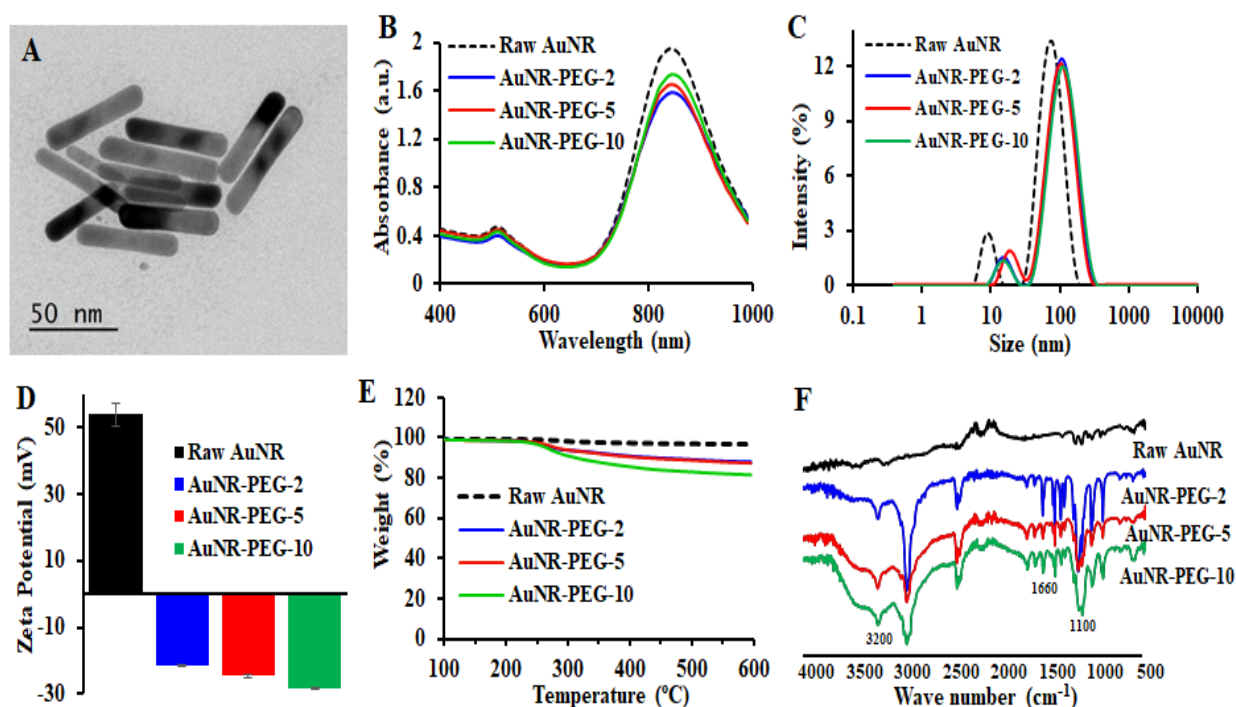


Figure 2.3 Physicochemical characterization of AuNRs before and after surface functionalization. (A) A representative transmission electron micrograph of as-synthesized AuNRs. (B) Surface plasmon resonance spectrum of NIR-responsive AuNRs before and after surface functionalization using PEG molecules of different molecular weights (viz., 2, 5, 10 kDa). (C) and (D) are the hydrodynamic size and zeta potential before and after PEG functionalization. (E) Thermogravimetric analysis for the quantitative determination of PEG functionalization. (F) FTIR spectrum of the AuNRs verifying PEG conjugation on the surface of the AuNRs. The number 2, 5, and 10 in the nomenclature of each sample represents the corresponding molecular mass weight of the PEG molecules in kDa.

performed in an inert environment and the mass of remaining metallic gold was recorded to permit calculation of the mass ratio between PEG and gold in the AuNRs. It is worth noting that metallic gold remains in the sample holder whereas the PEG completely decomposes as CO₂ and other volatile compounds. Therefore, from the residual percentage of metallic gold, the mass fractions of PEG in AuNR-PEG-2, AuNR-PEG-5, and AuNR-PEG-10 were found to be 12.0%, 12.7%, and 18.5%, respectively (**Figure 2.3 E**). We further translated these percentages into the number of PEG molecules per AuNR and found 3478, 1307, and 1088 molecules of PEG, corresponding to 2000, 5000, and 10,000 Da PEG, respectively. The functionalization of the AuNRs by PEG was further corroborated by FTIR analysis (**Figure 2.3 F and Appendix A-Figure 2. S2**). The FTIR spectrum of Raw AuNR, AuNR-PEG-2, AuNR-PEG-5, and AuNR-PEG-10 strongly support the surface modification with the thiol PEGs. The peak at 1100 cm⁻¹ is due to the etheral C-O stretching of the PEG molecule while the peak at 1600 cm⁻¹ is attributed to C=O stretching of the carboxyl group. The broad and very wide peak ranging from 2400 to 3400 cm⁻¹ is due to the hydrogen-bonded carboxyl group showing the surface-functionalized with PEG moiety.

2.3.3 NIR photothermal efficiency

The photothermal efficiency of the Raw AuNR, AuNR-PEG-2, AuNR-PEG-5, and AuNR-PEG-10 were investigated under 808 nm NIR laser irradiation. All samples suspended in an aqueous solution were irradiated at the continuous wave constant diode laser power of 21.2 W/cm² in a cell-free environment where the change in temperature versus time was noted using a thermal imaging system (Forward Looking Infrared systems). As shown in **Figure 2.4**, a time-dependent increase in temperature was observed in all samples. For Raw AuNR, the temperature of the suspension reached up to 56.3 ± 2.9 °C under NIR laser. In the case of AuNR-PEG-2, AuNR-PEG-5, and AuNR-PEG-10, the change in temperature were 47.1 ± 1.1, 57.1 ± 2.7, and 69.2 ± 2.7

°C, respectively. However, during NIR exposure, a change in the color of the Raw AuNR suspension was observed, which was confirmed by recording the change in LSPR (**Figure 2.5**). This is presumably due to the fact that the colloidal stability of AuNR is greatly affected by the local temperature, and high local temperature makes Raw AuNR unstable in the suspension (**Scheme 2.1**). To further elucidate the effect of NIR laser exposure on different PEG-modified AuNRs, we conducted a photothermal experiment where we measured the temperature at the top (point of laser contact), middle, and bottom of the AuNR suspension. The distance between the top, middle, and bottom positions were approximately 10 mm in depth. **Figure 2.4** demonstrates that the temperature distribution was highly non-uniform in the case of AuNR-PEG-10, with a substantial change in temperature from 69.2 ± 2.7 °C at the top (at the point of laser contact) to 18.2 ± 0.8 °C at the bottom. The other AuNRs show more uniformity in temperature. These results

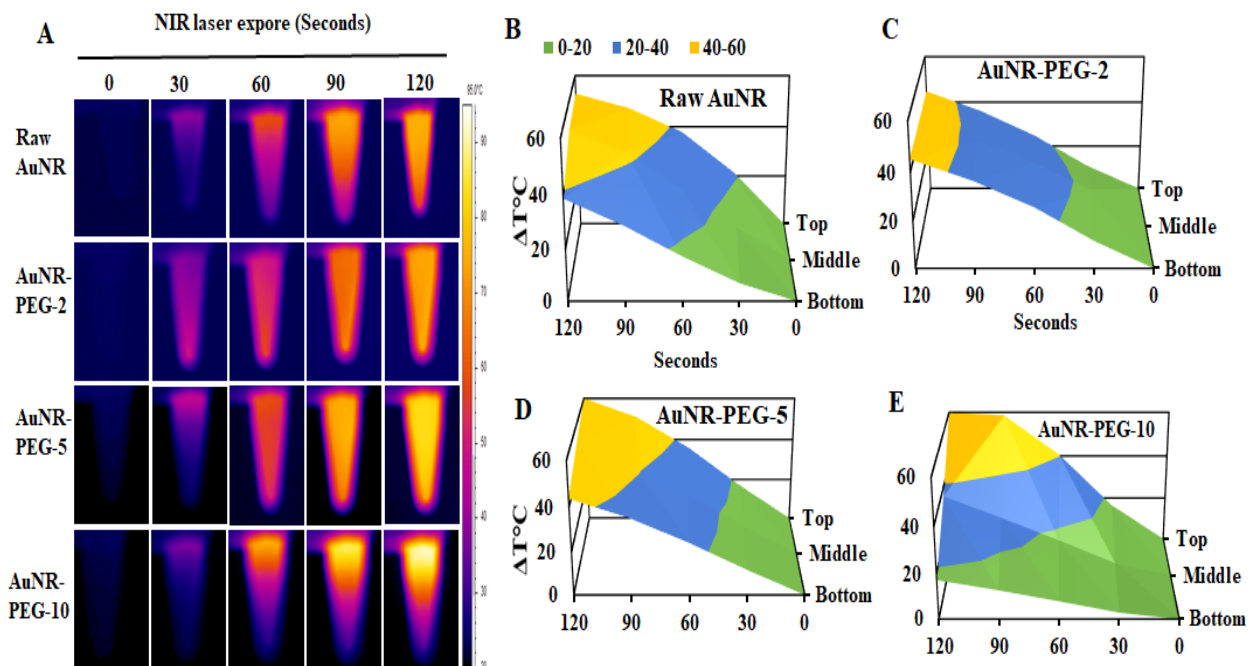


Figure 2.4 Photothermal properties of raw and PEG-functionalized AuNRs. (A) Various AuNR aqueous suspensions were irradiated with a near-infrared laser ($\lambda = 808$ nm, 21.2 W/cm²) for 120 seconds and the evolution of temperature throughout the suspension was recorded using a FLIR thermal camera system. (B), (C), (D), and (E) are the 3D temperature plots showing the average change in temperature as a function of time measured at the top, middle, and bottom of the AuNR suspension of raw AuNRs, AuNR-PEG-2, AuNR-PEG-5, and AuNR-PEG-10, respectively.

suggest that higher molecular mass PEG may thermally insulate the AuNRs, supporting a higher temperature gradient. Changes in the structural integrity and plasmonic properties of the AuNRs after NIR irradiation were investigated using transmission electron microscopy and UV-Vis spectrometry. As shown in **Figure 2.5 A**, the Raw AuNR and AuNR-PEG-2 show significant changes in their LSPR peaks after NIR irradiation, which is possibly due to the temperature-induced erosion of the AuNRs. For AuNR-PEG-5 and AuNR-PEG-10, the LSPR signals were quite stable even after NIR irradiation, which confirms the thermal stability of AuNRs after PEG grafting without negatively affecting their photothermal properties.

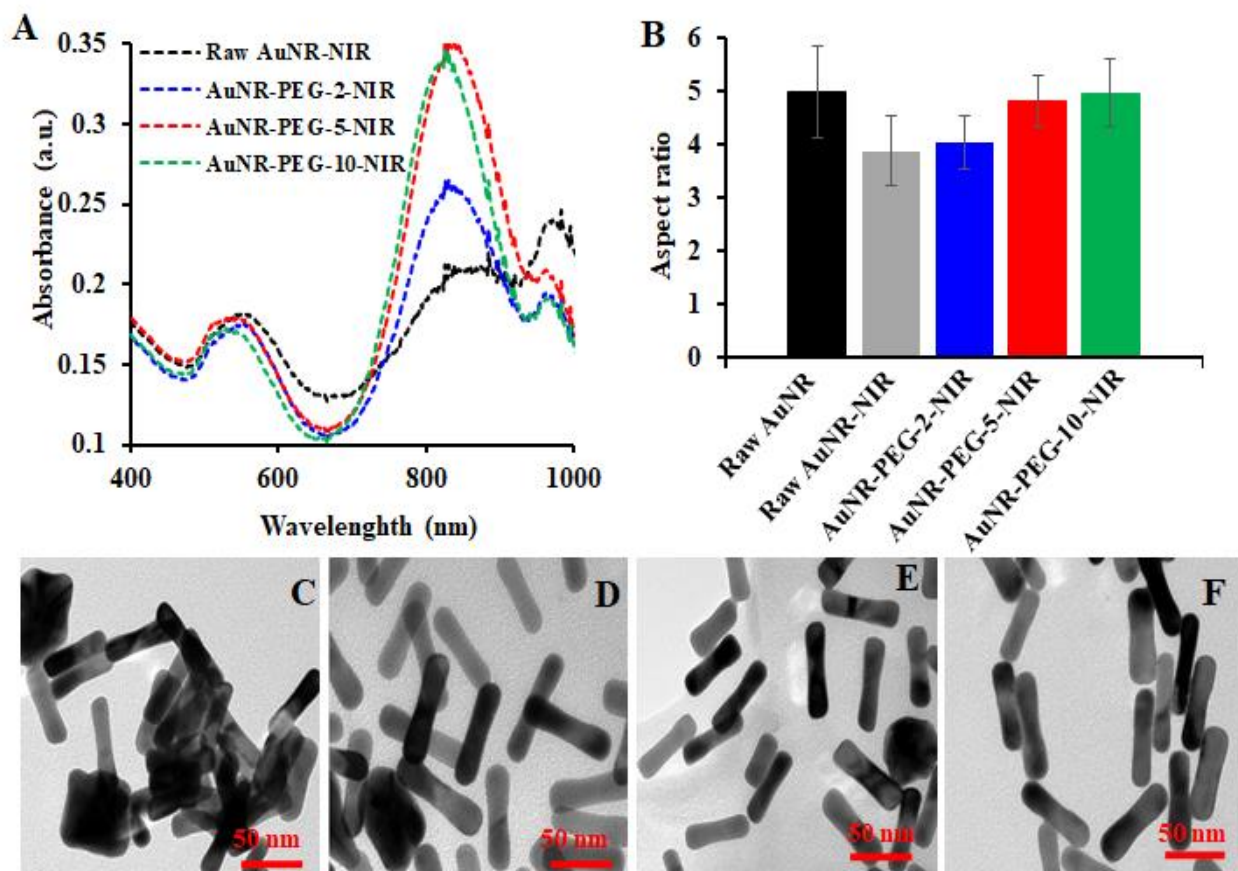


Figure 2.5 LSPR response and alteration in the AuNR aspect ratio after NIR exposure of raw and PEG passivated AuNRs. (A) UV-Vis spectrum showing changes in LSPR after NIR heating of both raw and PEG passivated AuNRs. (B) The average aspect ratio of both raw and PEG-functionalized AuNRs after NIR heating. (C) Raw AuNR-NIR, (D) AuNR-PEG-2-NIR, (E) AuNR-PEG-5-NIR, and (F) AuNR-PEG-10-NIR are the representative transmission electron micrographs. The aspect ratio was calculated by measuring the length and width of 100 nanorods per sample. Scale bar: 50 nm

2.3.4 Thermal conductivity calculations

To better understand how the PEG coatings affected the heat conduction from the AuNR surfaces, we performed molecular dynamics simulations of PEG-conjugated gold surfaces and calculated the thermal conductivity through the PEG brushes. To make the simulations feasible and simplify the analysis, we did not model complete AuNRs, but simply considered the structure of the PEG brush on flat slabs of gold. First, we compared the conductivity of a bare gold slab (**Table 2.1, System A**) to two models coated with PEG-SH molecules of different masses, mimicking the experiments. **Systems B and C** were conjugated with 2 and 5 kDa PEG molecules at densities of 1.98 and 0.86 molecules/nm², respectively, representing two types of nanorods used in the experiments (AuNR-PEG-2 and AuNR-PEG-5) (**Figure 2.6**). After relaxation, the 2 kDa PEG brushes appeared as shown in **Figure 2.6 A**. In this case, the 2 kDa PEG chains completely crowd the surface, leaving little access to water. Indeed, the graph of the water density, **Figure 2.6 B**, shows essentially no water within 4 nm of the gold surface, while the density of PEG near the gold surface is roughly the value of solid PEG. On the other hand, at the lower density of 5 kDa PEG molecules in **System C**, we observed less crowding of PEG near the surface, with significant amounts of water penetrating the brush. Because of the greater length of the PEG molecules, the brush in **System C** extended farther from the gold surface than of **System B**, reaching beyond 8 nm from the surface. The thermal conductivity of the two PEG-containing systems and the bare gold system and the bare gold system were calculated as described previously and detailed in the Methods Section, by applying a constant heat current between a segment of the system near $z = 0$ and a segment of the system near $z = \pm 8.9$ nm.¹¹⁸ Due to the use of periodic boundary conditions, the positions $z = \pm 8.9$ nm are equivalent and in physical contact. The exact heat current depended slightly on the number of water molecules in each segment of the system, but in all cases, the average was in the range of

2.1–2.4 μW . The average temperature distributions for the bare and PEG-coated slabs after reaching the steady-state are shown in **Figure 2.6 C**. In the case of the bare slab, the calculation was simply a measurement of the thermal conductivity of bulk model water being a uniform medium; the temperature distribution appears linear. The thermal conductivity, as determined by the slope of this distribution is $1.03 \pm 0.02 \text{ W}/(\text{m}\cdot\text{K})$, shown in **Table 2.1**, is about 60% larger than that for real water at the same temperature¹²⁵ which is not surprising due to the fact that the flexible TIP3P water model used in the simulations has a higher self-diffusion coefficient than real water.¹²⁶

Simulation system	PEG molecular mass [kDa]	PEG chain density [nm^{-2}]	Thermal conductivity [$\text{W}/(\text{K}\cdot\text{m})$]
A	-	0.0	1.03 ± 0.02
B	2.0	1.98	0.45 ± 0.01
C	5.0	0.86	0.40 ± 0.01

Table 2.1 Thermal conductivity was calculated in molecular dynamics simulations for PEG brushes of different PEG molecular masses and chain densities on a gold surface.

The temperature distribution of the PEG-coated gold surfaces (**Figure 2.6 C**) is not uniform, due to the heterogeneity of these systems. The slope of the temperature profile is greatest for $1.4 < |z| < 4.8 \text{ nm}$, which also corresponds to the region of greatest PEG density (**Figure 2.6 B**). The net temperature changes through the PEG brushes and water layer were 84 and 89 $^{\circ}\text{C}$, more than twice that in the pure water system (39 $^{\circ}\text{C}$), leading to proportionately smaller conductivities. Although the temperature fell below 0 $^{\circ}\text{C}$ (**Figure 2.6 B**) in some places, freezing was not and cannot be observed in these simulations.¹²⁷ The simulations support the notion that PEG conjugation acts to thermally insulate the gold nanorods from their environment, in agreement with the larger temperature gradients observed for the PEGylated nanorods in the experiment.

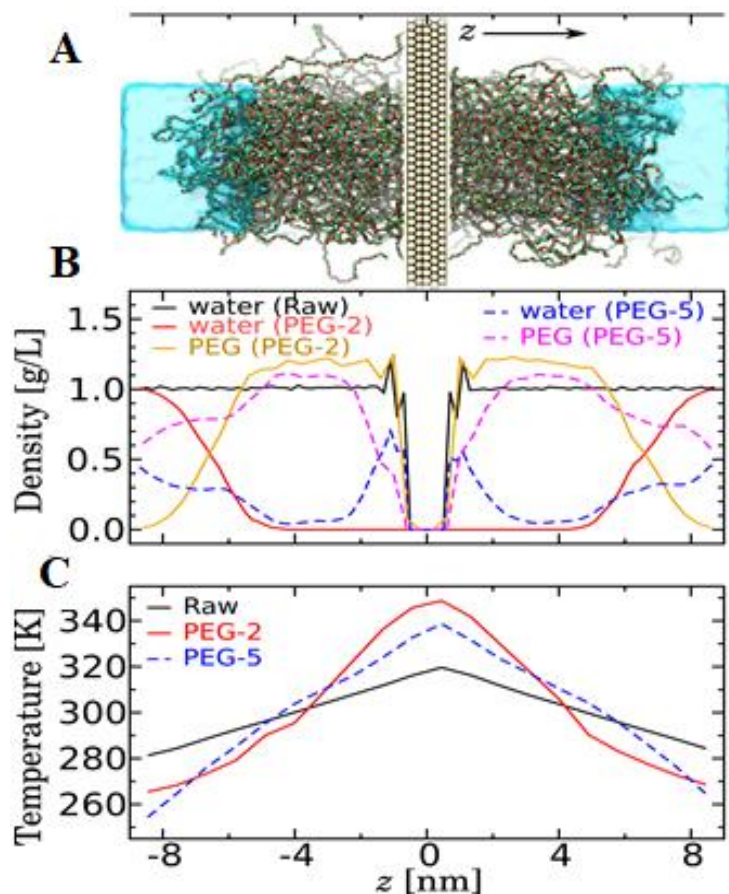


Figure 2.6 Molecular dynamics simulation of heat conduction through PEG brushes. (A) Snapshot of simulation System B for gold conjugated with 2 kDa PEG. The gold slab is shown as pale-yellow spheres. The thiolated PEG molecules, illustrated in a bond's representation, are colored by atom type (C, green; O, red; S, yellow). For clarity, H atoms are not shown, and the explicit water molecules are illustrated as a cyan surface. Due to the use of periodic boundary conditions, the left and right ends of the system are in physical contact, and the PEG-coated gold surfaces have an effectively infinite extent in the xy plane. (B) The mass density of water and PEG as a function of the z coordinate for **Systems A** (Raw), **B** (2 kDa PEG), and **C** (5 kDa PEG). The z scale is faithfully aligned with the image in panel A. (C) Steady-state temperature distribution in simulations where a constant heat current was induced in the system, permitting the thermal conductivity to be calculated. The larger temperature differences observed for the PEG-containing systems imply smaller thermal conductivities.

2.3.5 Cellular uptake study

The cellular internalization efficiencies of Raw and PEG-modified AuNRs were investigated in mouse melanoma cell line B16-F10 using hyperspectral dark-field microscopy and ICP-MS. ICP-MS was used to evaluate the amount of gold taken up by cells after 6 and 24 h of

exposure. After 6 h of incubation, the cellular uptake efficiencies of Raw AuNR, AuNR- PEG-2, AuNR- PEG-5, and AuNR-PEG-10 were found to be 44, 23, 32, and 30%, respectively (**Figure 2.7 A**). For 24 h of incubation, the cellular uptake efficiency of Raw AuNR, AuNR- PEG-2, Raw AuNR, AuNR- PEG-2, AuNR- PEG-5, and AuNR-PEG-10 were found to be 48, 28, 30, and 32%, respectively. The results indicate that the number of AuNRs taken up by B16-F10 cells is significantly greater for Raw AuNRs than for PEG-functionalized AuNRs. It is evident that PEGylation reduces the endocytosis of NPs and thus reduces its cellular internalization. No significant change was observed between different PEG-modified AuNRs even after 6 and 24 h incubation. It has previously been suggested that AuNRs are taken up *via* endocytosis and

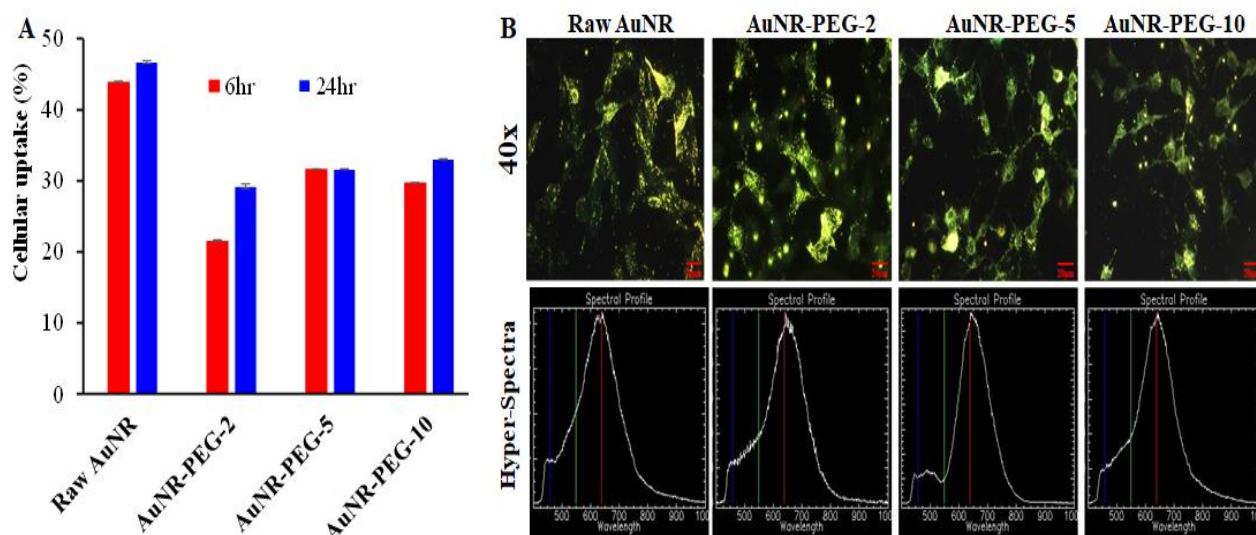


Figure 2.7 Cellular uptake efficiency of Raw and PEG-functionalized AuNRs with mouse melanoma (B16-F10) cell line. (A) Quantitative cellular uptake of AuNR at incubation times of 6 and 24 h measured by ICP-MS and (B) Darkfield hyperspectral microscopic images of B16- F10 cells treated with AuNRs, and corresponding hyperspectral graph (lower panel) indicating the structural integrity of AuNRs inside the cells. Both LSPR and TSPR are visible, which is characteristic of AuNRs.

localized in endosomes within the cell.¹²⁸ Further qualitative analysis with hyperspectral dark-field imaging shows that Raw and PEG-modified AuNRs were taken up by the cells without significant loss of their structural integrity, as evidenced by their plasmonic signals inside the cell (**Figure 2.7 B, lower panel**). The *in vitro* viability of cells containing Raw and PEG-coated AuNRs in the presence and the

absence of the NIR laser was investigated in mouse melanoma B16-F10 cell lines after 24 h of AuNR treatment. For the photothermal therapy experiments, after 24 hours of treatment, the cell was irradiated with a NIR laser of wavelength 808 nm and a power density of 14.1 W/cm² for 10 seconds. Cell viability as a function of the AuNRs dose was observed (**Figure 2.7 A, upper panel**).

2.3.6 NIR mediated phototoxicity study

For the Raw AuNRs, low cell viability was observed, even at a low dose of 0.5 µg/mL, likely due to the cytotoxicity of residual CTAB surfactant. At the highest concentration tested (25 µg/mL), the viability of cells with Raw AuNRs was found to be 20% in the presence of NIR radiation and 24% in its absence, a difference that was not statistically significant. In comparison with Raw AuNRs, PEG-functionalized AuNRs were found to be biocompatible with B16-F10 cells. At the highest concentration (25 µg/mL) tested, the viability of AuNR-PEG-2 treated cells were found to 60% in the absence of NIR radiation but was reduced to 28% after 10 s of NIR radiation. For AuNR-PEG-5, the cell viability was found to be 38% and 60% in the presence and absence of NIR radiation, respectively. For AuNR-PEG-10, the cell viability was found to be 30% and 60% in the presence and absence of NIR radiation (**Figure 2.8 A, upper panel**). Therefore, for the PEG-modified AuNRs, we observed a significant reduction in cell viability caused by irradiation from the NIR laser, in contrast to the Raw AuNRs. Most importantly, among the different PEG modifications, AuNR-PEG-5 exhibited significant phototoxicity even at the lowest concentration tested (0.5 µg/mL), while higher concentrations were required to observe significant NIR-radiation-induced toxicity for AuNR-PEG-2 and AuNR-PEG-10. The superior performance of AuNR-PEG-5 over the other AuNRs could be explained in **Figure 2.5**. During NIR treatment, the AuNR-PEG-2 nanorods have been partially destroyed, as evident from the change in their aspect ratio shown in **Figure 2.5 B** and

C-E. As a result of partial thermal destruction, a relatively small temperature change of 8 ± 1 °C in the cell suspension was observed (**Figure 2.8 B, lower panel**). Similarly, for AuNR-PEG-10, the thickness

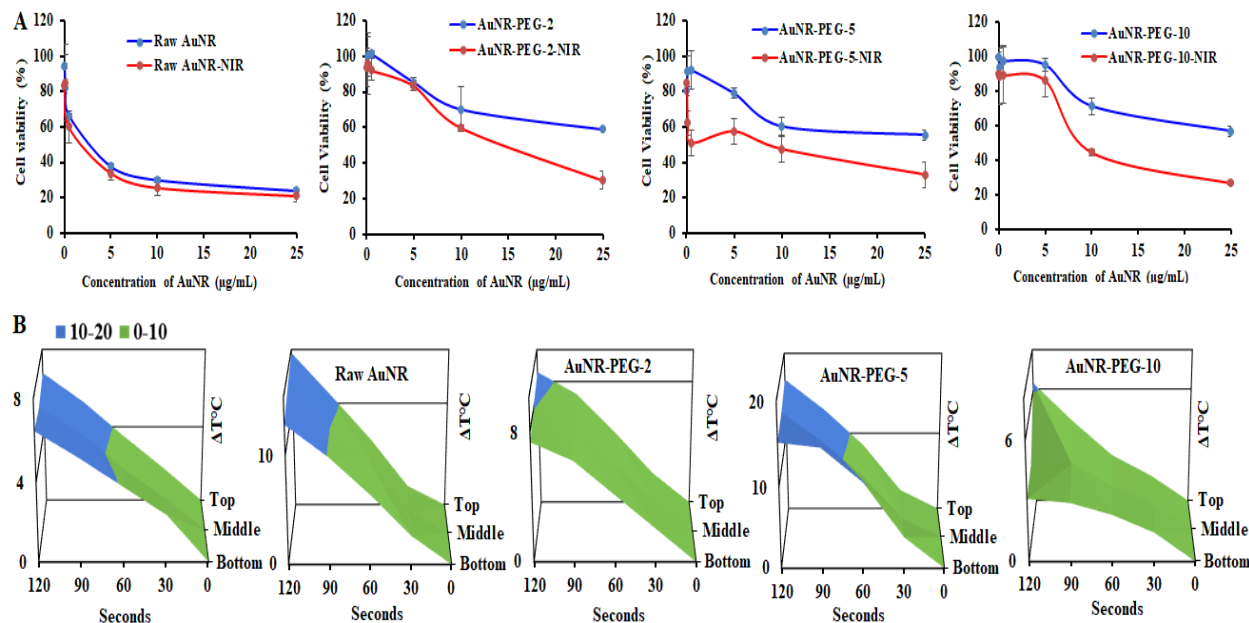


Figure 2.8 *In vitro* photothermal effect of raw and PEG-functionalized AuNRs against the B16-F10 cells. (A) Top panels showing the phototoxicity of raw AuNRs and PEG-functionalized AuNRs before and after laser irradiation (irradiation time = 10 s; $\lambda = 808$ nm); and (B) the bottom panels showing the change of temperature of raw and PEG-functionalized AuNRs under laser irradiation in the cell suspension. The cells were previously incubated with AuNRs for 24 h and recovered as a cell suspension to study the NIR mediated thermal effect with the same number of cells in all samples. The figures in the bottom panels are the 3D temperature plots showing the average change in temperature at the top, middle, and bottom of the cell suspension. Cells without AuNR treatment were used as the control cells.

of the PEG brush hinders the heat transfer at the particle- polymer- water interface. **Figure 2.8 B, lower panel**, provides great evidence of the pronounced effect in the case of AuNR-PEG-5 due to its thermal stability rendering efficient heat transfer to the surrounding thereby reaching cell suspension temperature to 18 ± 1.2 °C supporting results obtained from both experiment and molecular simulation.

2.4 Conclusion

In this study, we determined the influence of the PEG passivation on the AuNRs on their production of hyperthermia, with the aim to improve photothermal therapy of cancer. We compared

unmodified, CTAB-stabilized AuNRs, with three PEG coatings of different PEG molecular masses (2, 5, and 10 kDa). AuNR-PEG-2 has a denser PEG coating than that of AuNR-PEG-5 and AuNR-PEG-10 as demonstrated by molecular simulation and supported by the quantitative thermogravimetric analysis. Therefore, there is little room for AuNR-PEG-2 on its surface for water diffusion as compared to the AuNR-PEG-10. However, due to intermediate chain length, relatively less dense coating, and higher thermal stability of 5 kDa induce more heat. Under a NIR laser, AuNR-PEG-5 shows a higher degree of structural stability and more uniform temperature distribution with enhanced NIR induced thermal toxicity against mouse melanoma cell line, as compared to AuNR-PEG-2 and AuNR-PEG-10. Therefore, this comprehensive fundamental study suggested an optimum polymer length of 5 kDa of PEG is advantageous for better surface passivation and colloidal stability of AuNR, which also maximizes the heat conduction from the nanorod–fluid interface to the surroundings to enhance its photothermal efficiency. Overall, this study illustrates the need for a proper selection of surface functionalizing agent in rational design consideration of AuNR for biomedical applications.

Chapter 3 - Indocyanine-type infrared-820 encapsulated polymeric nanoparticle assisted photothermal therapy of cancer

Abstract

Organic small molecule photosensitizers are well characterized and known for the light-responsive treatment modality including photodynamic therapy. Compared with ultraviolet-visible (UV-Vis) light used in conventional photodynamic therapy with organic photosensitizers, near-infrared (NIR) light from 700–900 nm is less absorbed and scattered by biological tissue such as hemoglobin, lipids, and water and thus, the use of NIR excitation can greatly increase the penetration depth and emission. Additionally, NIR light has lower energy than UV-Vis that can be beneficial due to less activation of fluorophores present in tissues upon NIR irradiation. However, the low water stability, nonspecific distribution, and short circulation half-life of the organic photosensitizers limit its broad biological application. NIR responsive small-molecule fluorescent agents are the focus of extensive research for combined molecular imaging and hyperthermia. Recently a new class of NIR dye, IR-820 with excitation and emission wavelengths of 710 nm and 820 nm has been developed and explored as an alternative platform to overcome the limitations of most commonly used gold nanoparticles for photothermal therapy of cancer. Herein, we synthesized a core-shell biocompatible nanocarrier envelope made up of phospholipid conjugated with polyethylene glycol as a shell while polylactic glycolic acid (PLGA) as core to encapsulate IR-820 dye. The IR-820 loaded nanoparticles were prepared by nanoprecipitation and characterized for its physicochemical properties and photothermal efficiency. These nanoparticles were monodispersed and highly stable in physiological pH with the hydrodynamic size of 103 ± 8 nm polydispersity index of 0.163 ± 0.031 . The IR-820 loaded nanocarrier showed excellent

biocompatibility in the dark whereas remarkable phototoxicity was observed with breast cancer cells (MCF-7) upon NIR laser excitation. Therefore, the IR-820 loaded phospholipid mimicking biodegradable lipid-polymer composite nanoparticles could have great potential for cancer theranostics.

3.1 Introduction

With the progress of nanotechnology, there has been considerable attention in the treatment of cancer using thermal therapies such as magnetic hyperthermia, microwave-assisted hyperthermia, photosensitizer induced photodynamic therapy, and plasmonic nanoparticle-mediated photothermal therapy (PTT) due to their high tumor ablation efficiency, good spatial resolution, and minimal side effects.¹²⁹⁻¹³⁴ The most common feature in the aforementioned modalities is the use of heat energy to modulate cancer cells. Near-infrared (NIR) responsive fluorescent agents are the focus of extensive research for combined molecular imaging and hyperthermia. A key advantage of the PTT strategy is the fact that photothermal agents are capable of annihilating cancer cells with remote light irradiation while causing minimal damage to normal tissues.¹³⁴ In contrast to inorganic nanoparticles such as superparamagnetic iron oxide nanoparticles and gold nanoparticles, NIR absorbing small molecule organic dyes overcome the issue of metal-induced toxicity such as redox-active and unknown metabolic pathways when incorporated in a suitable envelope and thus are generally considered to be more biocompatible.¹³⁵⁻¹⁴⁰ On the other hand, optical imaging is inexpensive with good resolution, easy to handle, and can be made portable offering broad application when compared to other modalities such as magnetic resonance imaging, computed tomography, or positron-emitting tomography.¹⁴¹⁻¹⁴³ Thanks to the advancement in the fiber optics technology that makes optical imaging ideal for incorporation into an endoscope used in minimally invasive procedures. However, conventional optical imaging that

uses the light of lower wavelengths in the ultraviolet-visible (UV-Vis) region suffers due to the high light scattering and absorption by tissues.¹⁴⁴ Instead, NIR light of wavelengths from 700 to 900 nm has a deep tissue penetration limit owing to minimal scattering and tissue absorption.¹⁴⁵ Small organic molecule fluorescent probes that absorb energy in the NIR region will release vibrational energy in the form of heat following exposure to the light illumination and can kill cancer cells similar to that of plasmonic PTT mediated by noble metal nanoparticles.¹⁴¹

Indocyanine green is a tricarbocyanine-type dye with NIR-absorbing properties approved for visualization of retinal and choroidal vasculature, blood volume determination, and photodynamic therapy.^{139,140,146,147} However, the low water stability and short circulation half-life limit its broad application for hyperthermia and *in vivo* imaging.¹⁴⁸ To address these issues, the use of IR-820 dye as a potential alternative has been described in the literature.^{135,135,149–153} IR-820 dye has similar structural and optical characteristics to the indocyanine green with a relatively longer absorption range through maximal excitation and emission wavelengths of 710 nm and 820 nm, respectively. Prajapati and colleagues reported the use of IR-820 as a blood pool contrast agent to image tissue injuries and tumors in mice with improved circulation half-life compared to the indocyanine green.¹⁵³ In an *in-vivo* study by Pandey and colleagues where they conjugated IR-820 with a photodynamic therapy drug and studied its potential for dual imaging and thermotherapy.¹⁵⁴ Although these reports indicate that IR-820 has the potential for *in vivo* applications and provides an attractive alternative to the metallic nanoparticles, there is still more for the field to provide a detailed *in vitro* characterization regarding its photothermal efficiency and cellular behavior in nanoformulations.

When a NIR dye, as an organic photothermal agent, is encapsulated into a suitable delivery vehicle, it can be selectively activated by the external stimulus such as light after the dye has

reached its intended target, for example, tumor offering an image-guided treatment platform. The incorporation of the photothermal agent into self-assembled polymeric nanocarriers confers several benefits to PTT including biodegradability, scalability, and reproducibility.^{154–157} Herein, we designed a lipid polymer-based core-shell nanocarrier by encapsulating the indocyanine class of IR-820 dye into the polymeric for the photothermal treatment of breast cancer. These lipid-polymer hybrid nanocarriers delivered IR-820 to MCF-7 breast cancer cells as a potent mediator of PTT exhibiting significant cytotoxic effects upon excitation with clinically approved external laser light stimulus. The results also showed that these NPs induced cell death primarily through apoptosis, a preferred cell-death pathway over necrosis that may lead to the recurrence and metastasis of tumors.¹⁵⁸ With the great success of photothermal cancer treatment *in vitro*, this approach exhibits promising potential for *in vivo* applications. Furthermore, photothermal treatment modality could be improved by combining NIR-responsive agents with anticancer drugs or photosensitizers for combination therapy like photothermal–chemotherapy or photothermal–photodynamic therapy to maximize their therapeutic efficacy with synergistic cancer treatment.

3.2 Materials and Methods

3.2.1 Chemicals and reagents

Carboxylic end group terminated PLGA (lactide: glycolide= 50:50 dLg⁻¹) was purchased from DURECT Corporation (USA) and used after purification by repeated precipitation in diethyl ether. 1, 2-Distearoylphosphatidylethanolamine polyethylene glycol succinyl (DSPE-PEG-COOH), 1,2-distearoyl-sn-glycero-3-phosphoglycerol, sodium salt (DSPG), and phospholipid conjugated 1- α -phosphatidylethanolamine-N-(lissamine rhodamine-B sulfonyl) (Ammonium Salt) (RhB) was purchased from Avanti Polar Lipid Inc (Alabaster, AL, USA) and used as received. DAPI (4',6-Diamidino-2-phenylindole dihydrochloride, (3-(4,5-dimethylthiazol-2-yl)-2,5-

diphenyl tetrazolium bromide) (MTT), acetonitrile, and dimethyl sulfoxide (DMSO) were purchased from Sigma-Aldrich (Saint Louis, MO, USA). IR-820 (CAS No.: 172616-80-7) dye was purchased from BOC Sciences, NY, USA, and Annexin V/PI (Propidium Iodide) stain was purchased from BD Bioscience, USA. All other analytical grade reagents and solvents were used without further purification.

Human breast cancer (MCF-7) and Dulbecco's Modified Eagle's Medium (DMEM) were purchased from American Type Cell Culture (ATCC), Manassas, USA. Fetal Bovine Serum (FBS) USDA Premium Select, heat-inactivated was purchased from MIDSCI, Saint Louis, USA. Cells were maintained in DMEM supplemented with 10% (v/v), Fetal Bovine Serum (FBS), and 1% streptomycin at 37 °C in a 5% CO₂ environment. When cells reached 80 – 90% confluency in T75 cell culture flasks, they were passaged or plated by detaching the cells from the flask using Trypsin–EDTA (Thermo Fisher) and then counting the cells with a hemocytometer. The cell lines were used from passage 10 for bionano interaction studies.

3.2.2 Preparation of IR-820 encapsulated nanoparticles

PLGA with carboxylic acid terminated end group of molecular weight 50 kDa was used to synthesize IR-820 encapsulated PLGA nanoparticles following the well-established nanoprecipitation protocol.^{34,38,77,159,160} In a typical experiment, the calculated amount of IR-820 in DMSO was physically adsorbed with 1 mg PLGA in acetonitrile and made the final volume of the mixture to 1 mL to prepare IR-820 encapsulated PLGA nanoparticles. Then the phospholipids that consist of lipid mixtures formulations having 260 µg of DSPE-PEG and 200 µg DSPG were used in 4% ethanol, respectively. This lipid mixture was stirred at 60 °C for 30 min and then IR-820 encapsulated PLGA nanoparticles solution was added dropwise to the lipid suspension while stirring followed by the addition of 1 mL deionized water (acetonitrile:water=1:3). The content is

further stirred at room temperature for 1 h to facilitate the formation of nanoparticles. IR-820 encapsulated PLGA nanoparticles thus formed was purified using a 10 kDa Amicon[®] wash at 3500 rpm for 10 min. The washing was done three times in 1× PBS, made a final concentration of 1 mg/mL in 1× PBS, and stored at 4 °C until further use. Similarly, control nanoparticles were prepared in the same phospholipid ratio and PLGA content without IR-820.

3.2.3 Characterization of nanoparticles

The morphology of the purified NPs was characterized using a transmission electron microscope (TEM) (FEI Technai G2 Spirit BioTWIN). TEM samples were prepared by incubating 20 µL of IR-820 PLGA NPs (1 mg/mL) with 20 µL of 0.1% Uranyl acetate for 5 mins at room temperature. The sample was then placed on a formvar coated copper grid (400 mesh) and let stand for an additional 20 minutes. The excess amount of sample was removed before image acquisition. TEM images were acquired at 120 kV and analyzed by GATAN digital imaging system (GATAN, Inc.). Similarly, NPs were characterized for hydrodynamic size and zeta potential measurements using a Malvarian Zeta sizer Nano[®]. In this instrument, the Brownian motion and the Smoluchowski equation were used to calculate the average hydrodynamic size and zeta potential value, respectively. The colloidal stability of NPs was investigated in both ionic and serum conditions to mimic the biological environment. In brief, 1 mg NPs dispersed in the medium were subjected to hydrodynamic size analysis over the period to obtain size, polydispersity index (PDI), and zeta potential values. The reported intensity-based hydrodynamic diameter is the z-average of three measurements while the total count-based zeta potential is also the average of three measurements. The formulation with low PDI, high stability, and uniform narrow size distribution was selected for the *in-vitro* application. Likewise, the stability of IR-820 dye in NPs was studied by mixing 500 µL of IR-820 encapsulated NP and 500 µL of 1× PBS (n=3) over the period to

ensure the dispersity and colloidal stability of NPs in physiological media. The size and PDI of the particles after dispersed in PBS was measured for each day for a week using DLS.

The optical properties of IR-820 PLGA NPs were characterized by ultraviolet-visible spectrophotometer (BIOMATE-3S, Thermo Scientific) with 1.0 mm path length quartz cuvettes based on reading the absorbance of the NPs at 710 nm and comparing to a standard curve of known dye concentration dissolved in DMSO with dilution as required. The samples were scanned from 400 to 1100 nm with baseline correction. The amount of IR-820 released from the NPs while in storage conditions were also examined by UV-vis spectroscopy. At several time points between 0- and 7-days post preparation, samples were centrifuge using 10 kDa Amicon[®] filter to separate the NPs from released IR-820, and the collected released IR-820 was compared to a standard curve of known dye concentration using the same scanning conditions as described above. The dye release study was performed three times and the average and standard deviation of all three trials are reported.

For the IR-820 dye loading and release study, IR-820 was loaded on PLGA NPs by direct mixing of a known concentration of dye into the PLGA polymer followed by the nanoprecipitation technique.^{33,36,43,45} To optimize the maximum IR-820 loading, different calculated amounts such as 150, 300, and 400 µg of IR-820 were initially fed with 1 mg of PLGA dissolved in 400 µL of acetonitrile solution. The amount of encapsulated IR-820 was quantified, after purification, spectrophotometrically using a UV-vis spectrophotometer by measuring the absorbance of the NPs at 710 nm. The drug loading efficiency was calculated using the following equation:

$$\% \text{ loading efficiency} = (\text{amount of encapsulated IR-820} / \text{amount of initial IR-820 input}) \times 100.$$

The cumulative free IR-820 dye release from IR-820 PLGA NPs and free IR-820 (Mw= 849.47) were studied using 3.5 kDa molecular cut-off dialysis bags at physiological pH (pH 7.4, PBS). For this purpose, 300 µg IR-820 input formulation was selected for further studies due to the stable

physiochemical properties. Free IR-820 release from selected formulations was tracked throughout 72 h by dialysis. 1 mL of IR-820 PLGA containing 1 mg/mL of NPs or equivalent concentration of free IR-820 dye was dialyzed in 200 mL PBS release media kept at 37 °C, while constantly stirring (80 rpm) to maintain the sink condition during the experiment. 1 mL of release media was taken at a regular interval and replaced with equivalent fresh media. The amount of free IR-820 in the release media was quantified spectrophotometrically and the cumulative release percentage was calculated using the following equation:

$$\% \text{ cumulative IR-820 release} = (\text{IR-820 in release media} / \text{IR-820 in 100\% release}) \times 100.$$

The photothermal efficiency of free IR-820 and IR-820 PLGA NPs was measured in aqueous suspension upon 808 nm laser (China Deheng Group, Inc.) irradiation with a thermal camera imaging system (Forward Looking InfraRed FLIR A5 systems). Samples were suspended in phosphate-buffered saline (PBS) at an IR-820 concentration of 20 to 120 μM with a total volume of 1 mL in the Eppendorf tube. The free dye and IR-820 PLGA NPs were then irradiated with a continuous wave constant diode laser power of 808 nm laser for 2 min at varying power densities from 5.3 to 21.2 W/cm^2 while maintaining an approximately 1 cm distance between laser and sample. The concentration dependence photothermal efficiency for IR-820 PLGA NPs was examined by irradiating nanoparticles at concentrations of 20, 60, or 120 μM of IR-820 content with the 808 nm laser set to different power densities for 2 min. The temperature in each sample was recorded once every 30 seconds during irradiation and experiments were repeated three times. To further evaluate the influence of NIR laser exposure on the optical and physical properties of the NPs, we recorded the absorbance spectra, hydrodynamic diameter, and polydispersity index of IR-820 PLGA NPs were recorded by UV-vis spectroscopy and DLS both before and after irradiation.

3.2.4 Cellular biocompatibility and NIR mediated phototoxicity study

The *in-vitro* biocompatibility of free IR-820 dye and IR-820 PLGA NPs was conducted in MCF-7 cells using a colorimetric assay for assessing cell metabolic activity by 3-(4,5-Dimethylthiazol-2-yl)-2,5-diphenyltetrazolium bromide (MTT) assay. A time-dependent MTT assay in dark was conducted as discussed in the literature.^{40,106,161,162} In brief, cells at a density of 1×10^4 cells per well in a 96-well plate were incubated overnight. The seeded cells were washed twice with $1 \times$ PBS to remove the debris before NPs treatment. Then the medium was replaced with various concentrations of NPs (0.01, 0.1, 0.5, 5, 10, 25, 50, 100, 200 $\mu\text{g}/\text{mL}$) suspended in DMEM. The control cell was maintained without treatment. After 24 h of incubation, cells were washed with $1 \times$ PBS to remove surface absorbed and excess NPs. After washing, 100 μL MTT (5 mg/mL in PBS, filtered through 0.22 μm syringe) reagent was added to each well following manufacturer's recommendation. Then the supernatant was aspirated followed by the addition of 100 μL DMSO for solubilizing formazan crystal. The plate gently shaken in an orbital shaker for 5 min in the dark and absorbance was recorded at 560 nm using a microplate reader (BioTek, Synergy H1 hybrid reader). To analyze the data, background (DMSO only) was subtracted from the absorbance reading in each well. Triplicate well signals were averaged and then normalized to untreated cells. These experiments were performed in triplicate and analyzed by Student's t-tests at each concentration.

The *in-vitro* phototoxicity of IR-820 or IR-820 PLGA NPs was conducted in cells seeded as described above and treated with IR-820 PLGA NPs at IR-820 concentration of 60 μM or with fresh media for 24 h incubation at 37 $^{\circ}\text{C}$. The cells were then washed with PBS and incubated in fresh media for 1 h to bring the temperature to 37 $^{\circ}\text{C}$. The appropriate wells were then irradiated with continuous wave 808 nm light at 14.1 W/cm^2 for 30 seconds/well such that the treatment groups included no treatment, laser light only, IR-820 PLGA NPs only, or IR-820 PLGA

NPs with laser light with an approximately 1 cm distance between laser and sample. The irradiation was performed at room temperature and returned to the 37 °C incubator immediately following irradiation. After 24 h, MTT assay was performed as described above. Data obtained was compared side by side with the control experiment to map the relative toxicity. Data shown are from three experiments that were each run with triplicate wells and the data was analyzed by one-way ANOVA with post hoc Tukey.

3.2.5 Intracellular uptake study

To evaluate the cellular internalization competence of IR-820 PLGA NPs, experiments were conducted with MCF-7 cells using confocal microscopy and flow cytometry studies. For the confocal study, cells were seeded on poly-D-lysine coated eight chamber slides at a density of 50,000 cells per well and incubated for 24 h. Then the cells were treated with 50 µg/mL rhodamine-labeled IR-820 PLGA NPs suspension prepared in complete DMEM and incubated for 3 h. After incubation, treated cells were washed twice with 1×PBS (pH= 7.4), fixed with 4% paraformaldehyde for 30 min at room temperature. The nucleus of the cells was stained with 4',6-diamidino-2-phenylindole (DAPI) for an additional 10 min and imaged under a confocal laser scanning microscope (Carl Zeiss, CLSM-700). Cells without any treatment served as control cells. The quantitative percentage of fluorescence intensity was determined using the Image-J software. The quantification of the intensity of internalized RhB labeled NPs was calculated in terms of corrected total cell fluorescence (CTCF) by the use of the following equation:

$$\text{CTCF} = \text{Integrated Density} - (\text{Area of selected cell} \times \text{Mean fluorescence of background readings})$$

To investigate the quantitative cellular uptake of IR-820 PLGA NPs, fluorescence-activated cell sorting (FACS) study was conducted after labeling NP with rhodamine B dye using lipid insertion followed by the nanoprecipitation technique described above.^{34,40,159} In brief, MCF-

7 cells with passage 10 were plated at the density of 1×10^5 cells per well in on poly-D-lysine coated 24-well plates and incubated overnight. Cells were then treated with 0, 20, or 60 μM of IR-820 content in IR-820 PLGA NPs prepared as described above and incubated for 3 h to evaluate dose dependency. After 3 h, the cells were rinsed with $1 \times \text{PBS}$, lifted off the plate with Trypsin–EDTA, and resuspended in 500 μL of $1 \times \text{PBS}$ to yield a single cell suspension of 1×10^6 cells were analyzed by BD LSR Fortessa X-20 Special Order Research Product Flow Cytometer. Control cells were maintained without any treatments. 10,000-gated events were collected for all measurements. Density plots showing forward and side scatter data were used to create a primary gate for cells, excluding debris, prior to analyzing IR-820 PLGA NPs content.

3.2.6 Investigation of the mechanism of cell death induced by PTT

To analyze the mechanism of cell death induced *via* PTT mediated by IR-820 PLGA NPs, cells were seeded at 3×10^5 cells per well in a 24-well plate and incubated overnight. Cells were then treated with 20 μM of IR-820 content in IR-820 PLGA NPs for 3 h, at which time the cells were rinsed with $1 \times \text{PBS}$ and the wells replenished with fresh media. The appropriate wells were then irradiated with continuous wave 808 nm light at $14.1 \text{ W}/\text{cm}^2$ for 30 seconds per well for the following group of samples, no treatment, cells with laser light only, IR-820 PLGA NPs only, or IR-820 PLGA NPs with laser light. After the laser light treatment, the samples were returned to the incubator. After 24 h, an Annexin V/PI staining was conducted as per the manufacturer's recommendations. Briefly, cells were lifted from the plate with Trypsin–EDTA, washed with $1 \times$ binding buffer, and resuspended in 100 μL binding buffer containing 1:500 Annexin V and 1:1000 PI stains for 15 minutes in the dark condition. The samples were then diluted with 300 μL $1 \times$ binding buffer and analyzed on the BD LSR Fortessa X-20 Special Order Research Product Flow Cytometer with FITC (excitation, 488 nm; emission, 530/30 nm) and PerCP (excitation, 488 nm;

emission, 675/30 nm) channels. Density plots showing forward and side scatter data were used to create a primary gate for cells, excluding debris, before establishing gates for Annexin V-positive and PI-positive cells. 10,000-gated events were collected for all measurements. Positively stained gates were based on unstained cells and single stained controls including Annexin V only, PI only, or free IR-820 dye were used for compensation. The data presented are the average of three experiments and were analyzed by one-way ANOVA.

3.2.7 Data and statistical analysis.

The obtained data were plotted and compared to the significance of the results using GraphPad® software. Different statistical models and tests were carried out including T-test, F-test, and dose-response inhibition model fit using GraphPad software according to requirement. All data represent the mean \pm standard deviation. Biocompatibility and cytotoxicity data include six replicates ($n = 6$). All other major data includes at least three replicates ($n = 3$).

3.3 Results and Discussions

3.3.1 Physiochemical characterization

The nanoparticles were fabricated using the nanoprecipitation technique. The morphology of IR-820 PLGA NPs was characterized by TEM and DLS which showed that the nanoparticles were spherical, uniformly distributed, and the hydrodynamic diameter of 103 ± 8 nm (**Figures 3.1 A and B**). The encapsulation of IR-820 dye has no significant impact in the diameter of nanoparticles as compared to the control particles without dye which has a size of 96 ± 3 nm. These nanoparticles were negatively charged with zeta potential value of -28 ± 7 mV (**Figure 3.1 C**), as compared to the slightly negative charge (-1.6 ± 2 mV) of free IR-820 in aqueous condition. No significant change in surface zeta potential further assured that the IR-820 dye is loaded into the core of the NP. The negative charge in IR-820 PLGA NPs is due to the presence of the carboxylic

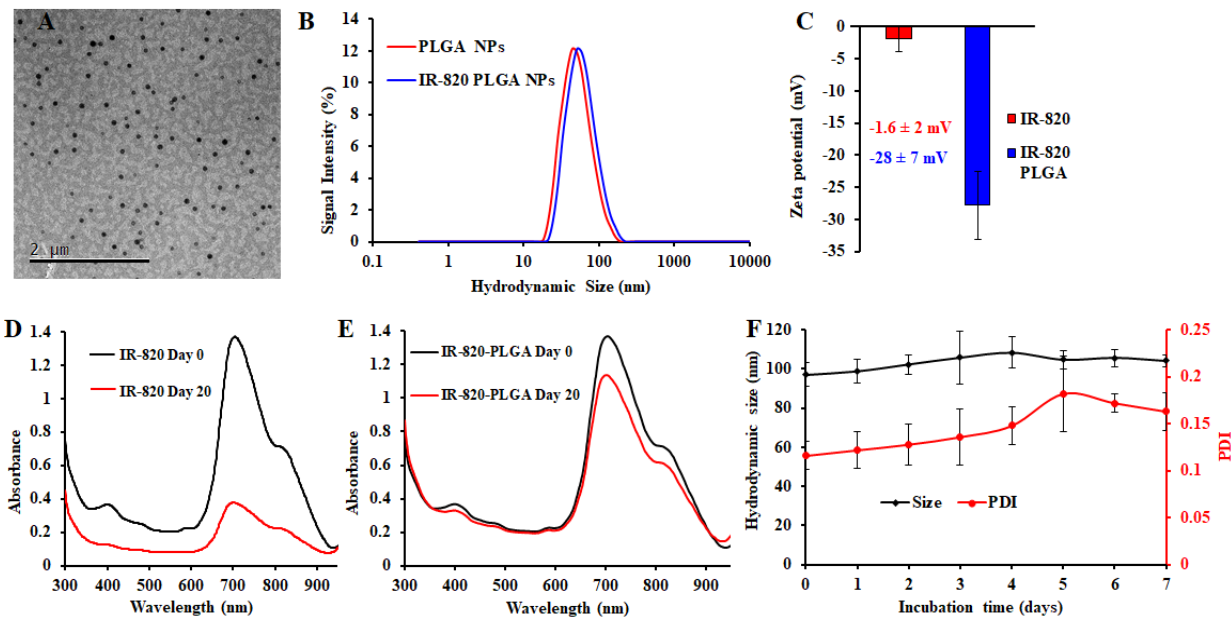


Figure 3.1 Morphology, size, and photostability of IR-820-PLGA NPs. (A) Transmission Electron Microscopy image of IR-820-PLGA NPs, (B) Hydrodynamic size with different initial input of IR-820 concentration (150 to 400 μg) per mg PLGA NPs, (C) Zeta potential of IR-820 and IR-820 PLGA NPs, (D-E) Optical properties (absorption profiles) of free IR-820 dye and IR-820 PLGA NPs in water before and after storage condition at 4°C as determined by UV–vis spectrophotometry. The concentration of IR-820 is 60 μM (corresponding to 300 μg input) for both free and encapsulated dye. (F) Stability of particles over storage. Data represents (n= 3).

acid terminated phospholipid PEG moiety. The optical property of the particles including free IR-820 and IR-820 PLGA NPs by using UV–vis spectroscopy revealed a characteristic extinction spectrum peak at 710 nm of free dye that is shifted further to the longer wavelength by 15 nm, red-shift, after loading into the nanoparticles (**Figures 3.1 D-E**). To evaluate the stability and retention of optical properties of IR-820 dye free in solution or loaded into the NPs, we analyzed the extinction spectrum of freshly prepared samples and samples that had been stored at 4 °C for three weeks. After storage in MiliQ water, we observed that free IR-820 dye loses its absorption capabilities, whereas IR-820 PLGA NPs fairly maintains its optical properties (**Figures 3.1 D-E**). To further examine the stability of IR-820 loaded PLGA NPs, we evaluated the colloidal stability by monitoring the hydrodynamic size and polydispersity index (PDI) up to seven days as shown

in **Figure 3.1 F**. During 7 days of incubation time, PDI of NPs varied from 0.116 to 0.163 and the size from 97 nm to 108 nm. Taken together with optical properties, these characterization data show minimum variation during the storage condition signifying better stability and the retention of dye in the NPs compared to the free dye solution.

Next, we studied the dye loading and release kinetics to explore the potential application of IR-820 in the drug delivery platform for PTT. IR-820 dye was used as a photo-responsive agent. The IR-820 dye was loaded into PLGA NPs using lipid insertion mediated nanoprecipitation technique. As shown in **Figure 3.2 A**, the percentage loading efficiency of dye with respect to the various initial input concentrations of dye was calculated. Our synthetic protocol yielded a high loading efficiency of 84% to 96% with input IR-820 concentration ranging from 400 μg to 150 $\mu\text{g}/\text{mg}$ polymer, respectively. Unfortunately, in the case of high loading content with 400 μg , IR-820 is aggregated as observed from the increased size and bimodal distribution (**Figure 3.2 B**). However, in the case of 300 μg IR-820 initial input, the size and PDI of NPs after loading (103 nm, 0.135 PDI) was similar to that of before loading (96 nm, 0.112 PDI) as shown in **Figure 3.1 B**. Also, the loading efficiency was 93% and the percentage of dye content (% wt) to the carrier was 1.37%. So, among different formulation studied, it was found that 300 $\mu\text{g}/\text{mg}$ polymer showed the best stability in media while maintaining its loading content. Therefore, we have chosen 300 $\mu\text{g}/\text{mg}$ polymer input formulation as a standard for further experiments. No significant changes in the size and PDI of this formulation were observed when incubated at 37 °C for 7 days in PBS (pH= 7.4) confirming the excellent physicochemical properties (**Figure 3.1 F**). To determine the release efficiency of the dye from the NPs, 2 mL samples of 1 mg/mL were placed in a dialysis bag and processed under identical conditions. We observed burst and sustained dye release kinetics for free IR-820 and IR-820 PLGA NPs over a 72 h period at 37 °C (pH= 7.4), respectively. The results, as

shown in **Figure 3.2 C** indicate that about 36% IR-820 was released within a period of 1 h while over 12 h, we observed about 90% in dye release kinetics. On the other hand, we found a higher order of dye stability in the IR-820 PLGA NPs. Less than 20% of IR-820 was released throughout the release study period of 72 h. These data are consistent with the literature with the release of similar lipophilic dyes such as DiR dye or indocyanine green from the nanoparticles.^{33,36,163,150,153} The stability of dye is highly essential in device NPs for theragnostic application.

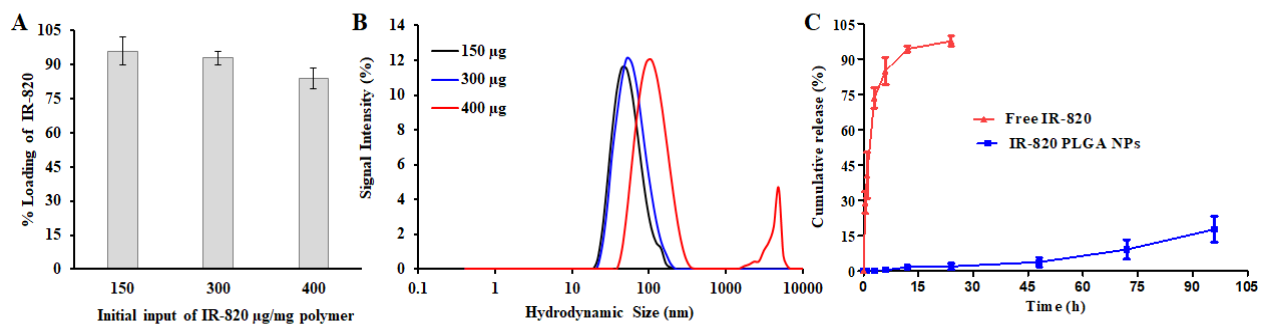


Figure 3.2 IR-820 loading and release study. (A) IR-820 loading into PLGA NPs, (B) Hydrodynamic size with different initial input of IR-820 concentration (150 to 400 µg) per mg PLGA NPs, (C) Cumulative dye release kinetics from free IR-820 and IR-820 PLGA NPs at physiological condition (PBS at pH 7.4). The concentration of IR-820 is 60 µM (corresponding to 300 µg input) for both free IR-820 and IR-820 PLGA NPs. Data represents (n= 3).

3.3.2 IR-820 mediated photothermal efficiency

The concentration dependence and laser power dependence photothermal efficiencies of free IR-820 and IR-820 PLGA NPs were investigated under 808 nm NIR laser irradiation using three different concentrations of IR-820 from 20 to 120 µM and power densities of 5.3, 14.1, and 21.2 W/cm². All samples suspended in an aqueous solution were irradiated where the change in temperature versus time was noted using a thermal imaging system at an interval of 30 seconds. As shown in **Figure 3.3**, a time-dependent increase in temperature was observed in all samples. As expected, we observed low heat evolution at a lower concentration of dye or laser power used for both samples. However, we did not observe any bigger difference in the temperature rise between free IR-820 dye or IR-820 PLGA NPs at identical dye content. As a general trend, we

found that IR-820 PLGA NPs produced more temperature compared to the free IR-820 under identical conditions of dye concentration and laser power used (**Figures 3.3 A and B**). At 5.3 W/cm², free IR-820 increased temperature (ΔT) from 3.7 to 19 °C while IR-820 PLGA NPs increased from 6 to 20.4 °C under similar dye content ranging from 20 to 120 μM . The temperature

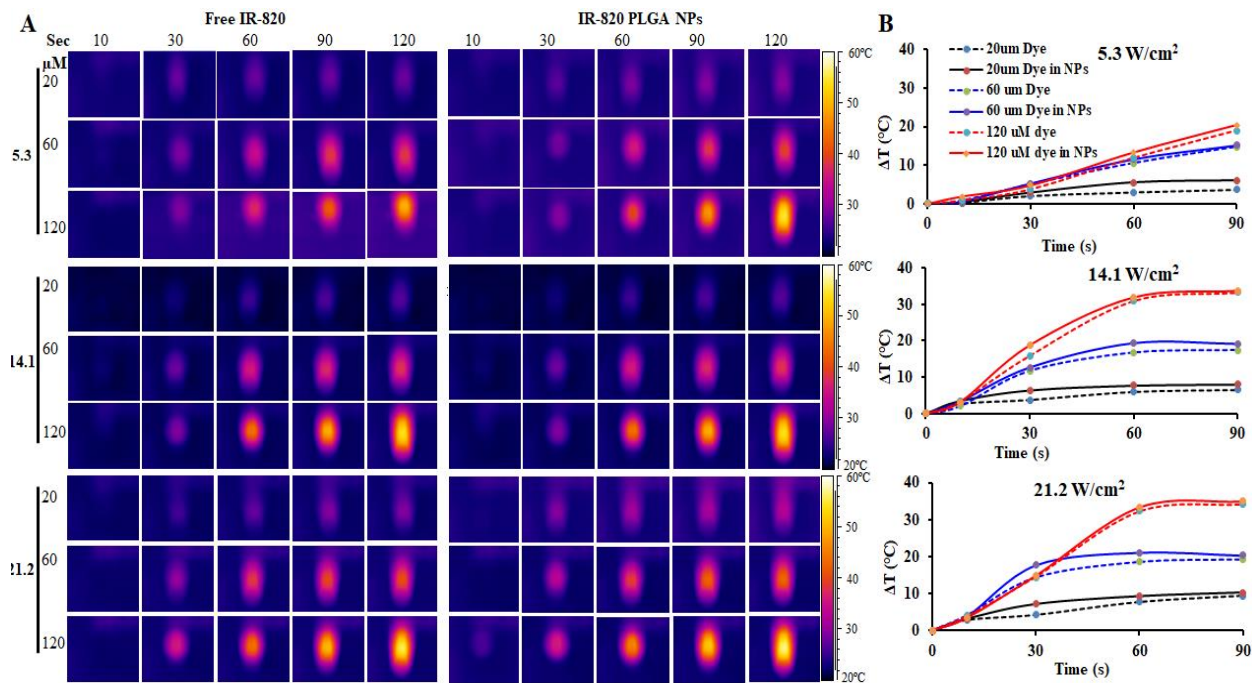


Figure 3.3 Comparative photothermal efficiency of free IR-820 dye and IR-820 PLGA NPs. (A) The concentration and power-dependent near-infrared laser ($\lambda = 808 \text{ nm}$) heating thermograph profile of IR-820 PLGA NPs and free IR-820 dye suspension upon laser irradiation. Three different laser power densities 5.3, 14.1, and 21.2 W/cm² and 20, 60, and 120 μM IR-820 dye corresponding to 150, 300, and 400 μg input /mg polymer were irradiated for 2 min with laser and sample distance of about 1 cm. The evolution of temperature throughout the suspension was recorded using a FLIR thermal camera system. (B) The corresponding temperature plots showing the average change in temperature as a function of time from panel A. Data represent (n= 3).

was increased from 6.5 to 33.3 °C and 8 to 33.6 °C while 9.4 to 34.2 °C and 10.2 to 35 °C for free IR-820 and IR-820 PLGA NPs at 14.1 and 21.2 W/cm², respectively. Interestingly, we did not find a significant difference in heat evolution at 14.1 *versus* 22.2 W/cm² irrespective of the sample. To investigate the effect of laser exposure to the optical and physicochemical properties of IR-820 PLGANPs or free IR-820, we recorded the UV-vis spectra and size of the particles. We observed a

significant reduction in the absorption peak of free IR-820 but a lesser effect of laser in the case of IR-820 PLGA NPs after laser exposure of 2 min (**Figures 3.4 A and B**). As shown in **Figure 3.4 C**, we did not much effect on laser irradiation in terms of size and PDI of the IR-820 PLGA NPs. However, during NIR exposure, a change in the color of the free IR-820 suspension was observed, which was confirmed by recording the change in optical density and absorption peak as can be seen in **Figure 3.4 A**. This is presumably because aqueous stability of IR-820 is greatly affected by the local temperature, and high local temperature makes free dye unstable in the suspension. In contrast to free IR-820, the retention of optical density and higher order of colloidal stability was observed in the case of IR-820 PLGA NPs. These results demonstrate that IR-820 PLGA NPs could act as an excellent photothermal source for therapeutic study.

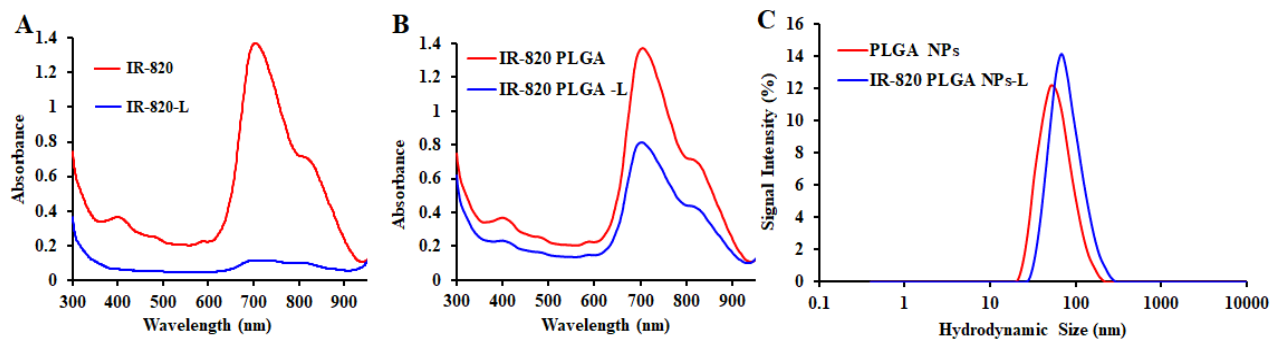


Figure 3.4 Optical response and alteration in the size of IR-820 PLGA NPs after laser exposure. (A-B) UV-Vis absorption profile showing the changes in optical density of free IR-820 dye and IR-820 PLGA NPs before and after laser irradiation. (C) Changes in the hydrodynamic size of PLGA NPs and IR-820 PLGA NPs after laser exposure measured by dynamic light scattering. These data were recorded for the laser power density 14.1 W/cm^2 and $60 \mu\text{M}$ IR-820 dye content either in free dye or in NPs were irradiated for 2 min.

3.3.3 Biocompatibility and cellular internalization study

Biocompatibility of free IR-820 and IR-820 PLGA NPs was performed in human breast cancer cell MCF-7 as presented in **Figures 3.5 A and B** for 48 h of treatment. IR-820 dye concentration as a handle was used to assess biocompatibility. IR-820 PLGA NPs showed at least 80% cell viability (**Figure 3.5 A**) at high concentration ($200 \mu\text{g/mL}$) while the viability of free IR-

820 was found to be 42% at an equivalent concentration (65 μM of IR-820), respectively (**Figure 3.5 B**). The dye concentration was used according to the dye content in nanoparticles used in **Figure 3.5 A**. This data signifies the biocompatibility of IR-820 PLGA NPs even at high concentrations. We further extended our approach to see if IR-820 loaded NPs were taken up by cells. We labeled IR-820 PLGA NPs with Rh-B and treated with cells for 3 h and found that these nanoparticles were taken up by cells (**Figure 3.5 C**). To further evaluate dose-dependency and quantitative cellular uptake, the same Rh-B labeled nanoparticles upon treatment and incubation of 3 h with IR-820 concentration of 20 or 60 μM , FACS study was carried out. As shown in **Figure 3.5 D**, nanoparticles were taken up by the cells and as expected, we observed a significantly larger amount of IR-820 PLGA NPs were taken up by cells when treated with 60 μM IR-820 content. It is worth mentioning that this concentration of nanoparticles is well tolerated with more than 70% of cells are viable even at large concentration input, 200 $\mu\text{g}/\text{mL}$ (**Figure 3.5 A**). Taken together, these observations reflect excellent biocompatibility and uptake of IR-820 PLGA NPs signifying that it can be used as a safe photothermal delivery agent.

3.3.4 NIR mediated phototoxicity study

We next investigated the use of IR-820 PLGA NPs mediated PTT as a treatment strategy for breast cancer and probed the mechanism of cell death induced by this treatment modality. MCF-7 cells were treated with 60 μM dye in IR-820 PLGA NPs, the maximum tolerated dose determined previously (**Figure 3.5 A**) for 3 h, and then samples were irradiated with an 808 nm laser and compared it with free IR-820 having identical dye concentration. Cells without any treatment were used as control throughout treatment experiments (**Figure 3.6 A**). The combination of IR-820 PLGA NPs and laser exposure for 30 seconds has resulted in significant phototoxicity having 70% and 42% cell viability after 24 h post-treatment as measured by MTT assay for 5.3 and 14.1 W/cm^2 laser

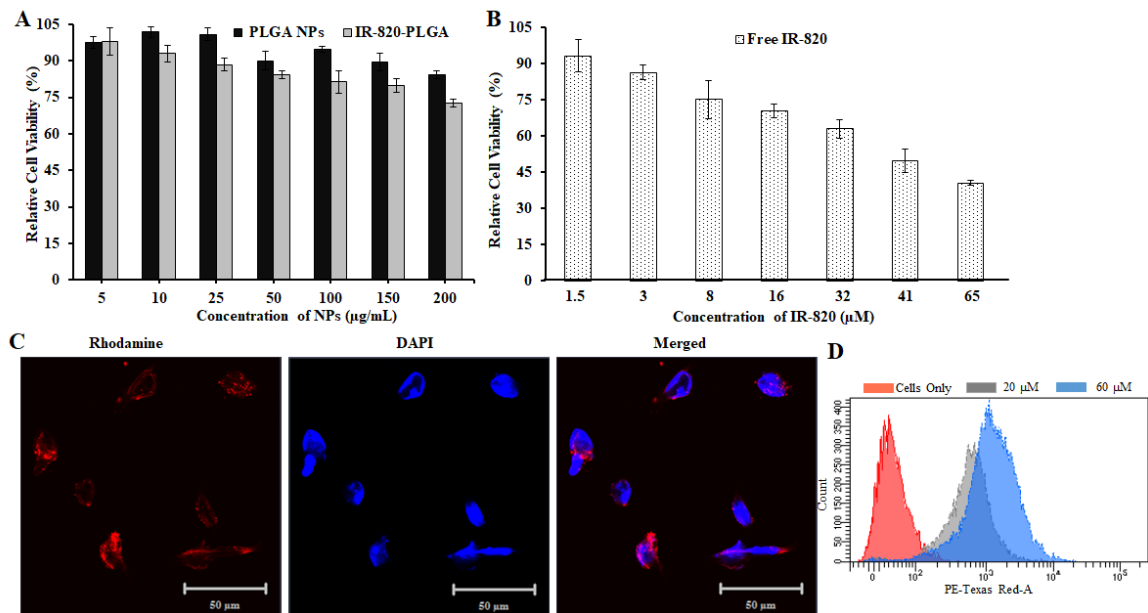


Figure 3.5 Cellular interaction study in MCF-7 cells. (A) Concentration-dependent relative cell viability of MCF-7 cells exposed to PLGA NPs or IR-820 PLGA NPs without light exposure. (B) Concentration-dependent cell relative viability of MCF-7 cells exposed to free IR-820 dye. The concentration of IR-820 was used similar to the IR-820 content encapsulated in PLGA NPs as shown in A. (Data represents (n= 6 for biocompatibility and n= 3 for FACS study).

power density, respectively. While 77% and 56% of cell viability were observed for free IR-820 under similar conditions before and after laser illumination. It should be noted that laser alone or laser + PLGA NPs (without dye) have no noticeable effect on the viability of cells. These data when taken together with aqueous photothermal efficiency data from **Figure 3.6** showed that $14.1\text{W}/\text{cm}^2$ is optimal for the IR-820 assisted photothermal therapy of cancer *in vitro*. Additionally, we evaluated the concentration dependence phototoxicity at $14.1\text{W}/\text{cm}^2$ while varying IR-820 concentration in samples, both free IR-820 and IR-820 PLGA NPs, from 1.5 to 65 μM as shown in **Figure 3.6 B**. With the increase in IR-820 content, the increase in IR-820 assisted phototoxicity was observed after laser exposure as measured by MTT. At lower concentrations of dye, we do not see much difference in the phototoxicity pattern. However, the IR-820 PLGA NPs produced significant phototoxicity at the concentrations of 16 to 65 μM when compared with its free dye counterpart (**Figure 3.6 B**).

3.3.5 Evaluation of mechanism for IR-820 PLGA NPs induced phototoxicity

After the successful PTT *in vitro* using IR-820 PLGA NPs, we next evaluated the mechanism of cell death by identifying the percentage of cells undergoing apoptosis *versus* necrosis using FACS study. Apoptosis is a preferred programmed cell death pathway in a normal physiologic process characterized by certain morphological features, including loss of plasma membrane asymmetry and attachment, condensation of cytoplasm and nucleus, and internucleosomal cleavage of DNA.¹⁵⁸ In apoptotic cells, the membrane phospholipid phosphatidylserine (PS) is translocated from the inner to the outer leaflet of the plasma membrane, thereby exposing PS to the external cellular environment, which upon treatment with Annexin V conjugated to fluorochromes including FIT-C, 35-36 kDa Ca²⁺ dependent phospholipid-binding protein that has a high affinity for PS, binds to cells with exposed PS.¹⁶⁴ This format retains its high affinity for PS and thus serves as a sensitive probe for flow cytometric analysis of cells that are undergoing apoptosis. FIT-C Annexin V staining leads to the loss of membrane integrity, which accompanies the latest stages of cell death resulting from either apoptotic or necrotic processes. Therefore, we stained with FIT-C Annexin V in conjunction with PI to identify early apoptotic cells (PI negative, FIT-C Annexin V positive). Thus, we assessed the mechanism of cell death by first treating cells with no treatment versus 20 μ M of IR-820 in IR-820 PLGA NPs for 3 h and then irradiating the samples with 808 nm light for 30 seconds at 14.1 W/cm². After 24 h of incubation, cells were stained with Annexin V (FIT-C channel) and PI (PE channel) for analysis by flow cytometry. Viable cells with intact membranes exclude PI, whereas the membranes of dead and damaged cells are permeable to PI. As shown in representative scatter plots in **Figure 3.6 C**, cells that stain positive for Annexin V only (bottom right quadrant Q4) are undergoing early apoptosis, cells that stain positive for Annexin V and PI (top right quadrant Q2) are undergoing

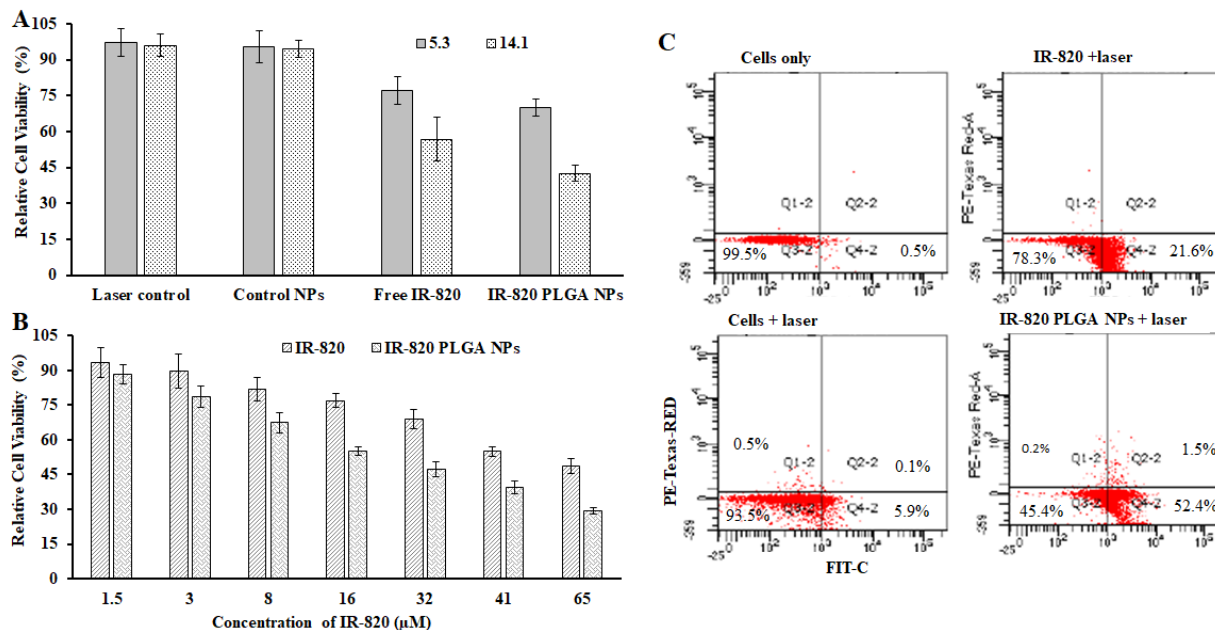


Figure 3.6 NIR mediated phototoxicity study and its mechanism of cell death in MCF-7 cells. (A) A comparative power-dependent photothermal therapy using either cells, PLGA NPs, free IR-820, or IR-820 PLGA NPs (60 μM) with laser exposure for 30 sec. These data were recorded for the laser power density 5.3 versus 14.1 W/cm², respectively to map the best power density for further investigation. (B) A comparative dose-dependent relative phototoxicity of MCF-7 cells after photothermal therapy generated by free IR-820 versus IR-820 PLGA NPs having identical IR-820 content after 808 nm laser exposure for 30 seconds at 14.1 W/cm². (C) A representative scatterplot demonstrating the fraction of cells in early apoptosis (bottom right quadrant), late apoptosis (top right quadrant), or necrosis (top left quadrant) following treatment with media only, cells +laser, IR-820-PLGA NPs only, or IR-820-PLGA NPs + laser.

late apoptosis and cells that stain positive for PI only (top left quadrant Q1) are undergoing necrosis. The flow cytometric analysis showed that IR-820 PLGA NPs induced cell death *via* PTT by primarily through apoptosis (52%) with no notable increase in necrotic cell percentage (0.2%) (**Figure 3.6 C**). In contrast to the PTT using gold nanoparticles as seen in our previous study, the rapid and high raise in the temperature in cell suspension results in cellular necrosis where there is a reported pro-inflammatory response that can elicit a negative immune reaction that may actually promote tumor recurrence.^{165,158,166,167} Therefore, it is essential to produce normal physiological cell death to achieve long-term survival benefits. These data when taken together with the MTT data indicate that IR-820 PLGA NPs can successfully mediate proapoptotic PTT of

breast cancer cells *in vitro* warranting further investigation of its use *in vivo*. Furthermore, because of the limitation of Annexin V and PI assay which does not distinguish between cells that have undergone apoptotic death *versus* those that have died as a result of a necrotic pathway because in either case, the dead cells will stain with both Annexin V and PI, therefore it is suggested to measure apoptosis over time so that cells can be tracked from Annexin V and PI negative (viable, or no measurable apoptosis), to Annexin V positive and PI negative (early apoptosis, membrane integrity is present) and finally to Annexin V and PI-positive (late- apoptosis and death).

3.4 Conclusion

In summary, we showed that IR-820 dye when encapsulated into lipid polymer composite nanoparticles that are monodispersed and highly stable maintaining optical characteristics of IR-820 dye. The IR-820 PLGA NPs were taken up by cells and exhibited excellent biocompatibility as compared to the free IR-820 dye. However, the combination of NIR laser with IR-820 PLGA NPs has induced significant cell death when compared to its counterpart free IR-820 dye at equivalent dye concentration. Furthermore, we confirmed that the mechanism of NIR mediated cell death mainly *via* apoptosis. Considering the fact that the polymer and lipids used herein are biodegradable and FDA approved biomaterials, these nanoparticles overcome the limitations of toxicity associated with metallic especially gold and iron nanoparticle-mediated thermal treatments. This study warranted further validation *in vivo* PTT and the mechanism of cell death is also essentially *via* apoptosis *in vivo*. Additionally, one could expect to compare and contrast the photothermal efficiency and mechanism of cell death of this system with gold nanoparticles for the quantitative analysis of each system. Overall, IR-820 PLGA NPs showed promise in the PTT and lays the foundation for further investigation.

Chapter 4 - Synthesis and characterization of a tumor-seeking LyP-1 peptide integrated lipid–polymer composite nanoparticle

*Chapter 4, in full, is a reprint of the material in **Materials Advances**, 2020. DOI: [10.1039/D0MA00203H](https://doi.org/10.1039/D0MA00203H)*

Abstract

Biocompatible polymeric and lipid nanoparticles are under extensive investigation as anticancer nanomedicines due to the ease of chemical modification in both polymer and lipid in order to target the distinctive tumor environment. However, microenvironment and molecular heterogeneity in tumors pose a great challenge to deliver anticancer drugs or imaging agents precisely, further limiting their applications. As a result, existing nanomedicine formulations rely on a passive-drug targeting mechanism taking advantage of leaky tumor vasculature. However, one strategy does not fit for all due to the molecular dissimilarities between cancers. Therefore, more research on tumor-specific receptors is needed to maximize drug delivery, while minimizing drug-related adverse effects. In addition, a high degree of the immunocompatibility and aqueous stability of the delivery device is essential to maximize delivery efficiency. Herein, we are addressing the aforementioned requirements in cancer management by engineering a receptor-specific anticancer nanomedicine as a composite of polymer and lipids. We are presenting a tumor seeking cyclic LyP-1 peptide integrated core–shell polymer–lipid composite nanoparticle (NP) that targets the overexpressed p32 receptor in cancer cells. The designed nanoconstruct is composed of poly(lactide-*co*-glycolic acid) as a skeleton and a cargo reservoir, a phospholipid with polyethylene glycol as a stabilizer, and LyP-1 as a targeting motif. We studied cellular interaction and targeting ability by accessing the full spectrum of biodistribution using NPs labeled with near-infrared dye as an imaging tracer *in vivo*. The NPs are spherical and monodispersed with an average hydrodynamic size of 79

± 3 nm and negative zeta potential. These particles are highly stable in physiological conditions over the period with a lower polydispersity index (PDI = 0.15). Furthermore, the nanoparticles showed excellent biocompatibility *in vitro*, with significantly higher uptake by mouse osteosarcoma compared to non-cancerous mouse fibroblasts. Likewise, LyP-1 NP showed nearly three-fold enhancement in tumor accumulation *in vivo* compared to its non-targeted counterparts in the K7M2 tumor. Considering the overexpression of p32 in many cancers, the proposed nanoconstruct could hold promises in the therapeutic planning of a wide range of tumors.

4.1 Introduction

The lipid-polymer composite nanoparticle exhibits complementary characteristics of both lipid and polymer that have shown remarkable clinical success in drug delivery.^{168–170} These composite nanoconstructs are distinctly organized creating different core-shell compartments to host the guest molecules. Herein, a skeleton of the polymeric hydrophobic core which can encapsulate drugs whereas lipid as the hydrophilic shell can be tuned for receptor targeting moieties and contrast agents.^{37,171,172} As such, the versatile chemistry of hydrophilic head moiety of phospholipid can be uniquely redesigned for precision drug delivery.¹⁷³ Regardless of their complex structure, these lipids-polymer composite nanoparticles (NPs) are synthesized in a simple, single-step fashion, which allows future scale-up production and cost-effective real-life applications.^{168,173–178} It has been established that the functionalization of polymer end groups and subsequent conjugation with targeting motifs such as peptides as a nanoparticle vehicle is a powerful strategy to permit precise drug delivery to the targeted site while reducing systemic toxicities.¹⁷⁹ The use of food and drug administration approved polymeric biomaterial, polyethylene glycol (PEG) as a surface passivating layer onto the nanoparticle prevents aggregation, opsonization, phagocytosis, and prolonging systemic circulation time to improve

nanoparticle-based drug delivery system.^{180,165,181,182,36,183} Also, it offers a facile PEG end functional chemistry that provides further room to improve NP's delivery, for instant covalent attachment of small molecules, antibody, and tumor targeting peptides.^{184,185}

Tumor targeting peptides are small peptides capable of targeting tumor tissue and internalizing in tumor cells. The tumor-specific receptor-mediated interaction associated with tumor-targeting peptide makes them outstanding candidates to dose a high concentration of any attached payload for tumor-targeted drug delivery. Recently, the LyP-1 peptide has been recognized for its unique specific localization into tumors.²² It is a cyclic peptide having sequence CGNKRTRGC discovered by the *in-vivo* phage display method. A uniquely structured nine amino acid residues arranged in C-terminal motifs (KRTR) binds to the specific receptor p32 (globular head of complement component 1q receptor or gC1qR) and takes the peptide or peptide conjugated cargo to the vascular endothelium in the target tissue *via* the CendR pathway.^{186,187} Extensive accumulation of LyP-1 was reported in the areas with higher expression of p32, such as tumor-associated macrophages, the luminal lining of tumor lymphatics, and tumor cells.¹⁸⁷⁻¹⁹¹ P32 has a functional role in maintaining oxidative phosphorylation in normal cells.³⁰ Research has shown that its expression and the subcellular location are changed in many cancers including breast, colon, melanoma, ovarian, bone, and prostate.^{188,189,192,193} This mitochondrial p32 is also responsible for regulating cancer cell metabolism and critical for tumor advancement. Its genetic knockdown has significantly reduced tumor formation *in-vivo*.¹⁹⁴⁻¹⁹⁶ Therefore, p32 is a potentially important therapeutic target in cancer.

Upon this background, we designed a tumor homing LyP-1 peptide integrated lipid-polymer composite nanoparticles to deliver cargo precisely to the tumor. We hypothesized that due to the overexpression of p32 in cancer and its specificity with LyP-1 peptide, the synthesized LyP-1 NP could preferentially deliver cargo *via* receptor-mediated interaction. This targeted composite NP

consists of outer polyethylene glycol corona as a stabilizer, LyP-1 as a tumor seeking peptide, a monolayer of phospholipids mixture containing 1,2-distearoylphosphatidylethanolamine (DSPE) and 1,2-distearoyl-sn-glycero-3-phospho-rac-glycerol (DSPG), and poly (L-lactic-co-glycolic acid) (PLGA) polymer core for the encapsulation of drug. Conjugation chemistry was utilized to label peptide with carboxylic acid terminated DSPE-PEG in a single-step followed by nanoprecipitation resulting in the formation of LyP-1 NP. By using *in-vitro* and *in-vivo* studies, we found that LyP-1 NP is highly stable in biological media, transverse the systemic circulation, and specifically accumulate to the tumor region compared to control NPs. Due to the tumor-seeking feature of the integrated peptide, the proposed nanosystem could drive maximum payload to the tumor site.

4.2 Materials and Methods

4.2.1 Chemicals and reagents

Carboxylic end group terminated PLGA (lactide: glycolide = 50:50 dLg⁻¹) was purchased from DURECT Corporation (USA) and used after purification by repeated precipitation in diethyl ether. 1, 2-Distearoylphosphatidylethanolamine polyethylene glycol succinyl (DSPE-PEG-COOH), 1,2-distearoyl-sn-glycero-3-phosphoglycerol, sodium salt (DSPG), and phospholipid conjugated 1- α -phosphatidylethanolamine-N-(lissamine rhodamine-B sulfonyl) (Ammonium Salt) (RhB) was purchased from Avanti Polar Lipid Inc (Alabaster, AL, USA) and used as received. DAPI (4',6-Diamidino-2-phenylindole dihydrochloride, (3-(4,5-dimethylthiazol-2-yl)-2,5-diphenyl tetrazolium bromide) (MTT), doxorubicin hydrochloride (DOX) (European Union pharmacopeia standard), acetonitrile, 1-ethyl-3-(3-dimethylaminopropyl)-carbodiimide (EDC), N-hydroxysuccinimide (NHS), and dimethyl sulfoxide (DMSO) were purchased from Sigma-Aldrich (Saint Louis, MO, USA). Rapid Gold BCA Assay (Cat No: A53225) was purchased from Thermo Fisher Scientific, USA. All other analytical grade reagents and solvents were used without further purification.

4.2.2 Cell lines and animal tumor model

Mouse osteosarcoma (K7M2), mouse normal fibroblast (NIH/3T3), and Dulbecco's Modified Eagle's Medium (DMEM) were purchased from American Type Cell Culture (ATCC), Manassas, USA. Fetal Bovine Serum (FBS) USDA Premium Select, heat-inactivated was purchased from MIDSCI, Saint Louis, USA. K7M2 and NIH/3T3 were maintained in DMEM supplemented with 10% (v/v), Fetal Bovine Serum (FBS), and 1% streptomycin at 37 °C in 5% CO₂ environment. The cell lines were used from passage 10 for bionano interaction studies. Six-week-old female immunodeficient NU/NU nude mice were procured from Charles River Laboratories International, Inc. and used for the study after ten days of acclimatization. The Institutional Animal Care and Use Committee (IACUC) and Institutional Biosafety Committee, Kansas State University, Manhattan approved all animal experiments and protocols. The solid tumor model using osteosarcoma cancer cells was developed by subcutaneous injection of 1×10^6 K7M2 cells into the rear flank of mice. Tumor growth and animal health were regularly monitored by measuring tumor volume, body weight, and physical health following an approved IACUC protocol.

4.2.3 Synthesis of LyP-1 conjugated lipid

As shown in **Scheme 4.1 A**, DSPE-PEG-LyP-1 was synthesized in a straightforward manner using well-established EDC-NHS bioconjugation coupling chemistry following the published protocol.¹⁹⁷ First, 0.08 mmol of EDC was dissolved in 500 μ L of 1 \times phosphate buffer saline (PBS) in 3 mL, and then gradually added to the 0.008 mmol of the DSPE-PEG-COOH dissolved in 5 mL of 1 \times PBS, stirred for 1 h at room temperature for the activation of the carboxylic group. Then, 3 mL of 0.5 mmol of NHS in 1 \times PBS was added to the previously activated lipid mixture. The whole mixture was further stirred for 2 h at room temperature. Then, 0.002 mmol of LyP-1 peptide dissolved in 1 \times PBS was added and stirred overnight at room temperature. The product was purified

three times by dialysis using 3000 Da molecular weight cutoff and lyophilized to recover the product. The obtained final concentrated product was stored at -20°C for further use.

4.2.4 Preparation of LyP-1 conjugated lipid-polymer composite nanoparticles

There are five components in LyP-1 NP *viz.*, PLGA NPs, phospholipids, DOX, LyP-1, and imaging probe DiR (**Scheme 4.1 B**). PLGA with carboxylic acid terminated end group of molecular

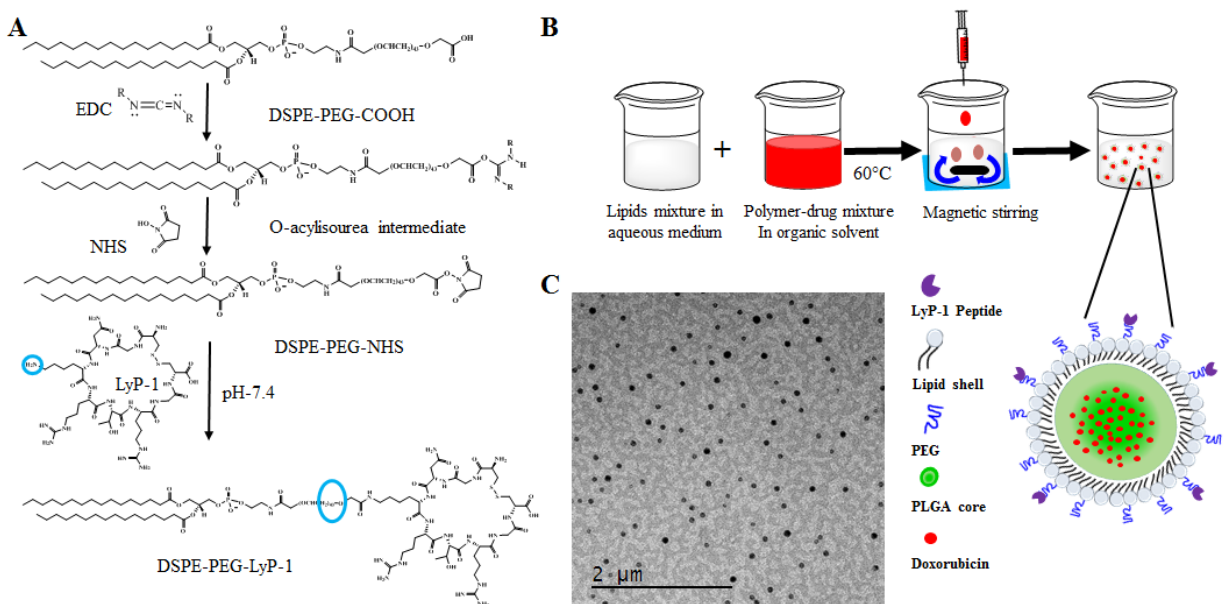


Figure 4.1 Graphical representation of DSPE-PEG and LyP-1 conjugate synthesis and nanoparticle fabrication process. (A) Synthetic scheme of LyP-1-PEG-DSPE using EDC/NHS bioconjugation, (B) Cartoon representation of nanoprecipitation forming lipid-polymer composite nanoparticles, and (C) transmission electron micrograph of synthesized composite nanoparticles.

weight 50 kDa was used to synthesize LyP-1 NP following the well-established nanoprecipitation protocol.^{34,38,77,159,160} In a typical experiment, 1 mg/mL PLGA in 400μL acetonitrile was used to prepare nanoparticles. The second component is phospholipids that consist of lipid mixtures formulations having 250 μg of DSPE-PEG, 200 μg DSPG, and 10 μg LyP-1- DSPE-PEG were used in 4% ethanol, respectively. This lipid mixture was stirred at 60°C for 30 min and 1mg of PLGA in 400 μL acetonitrile solution was added dropwise while stirring followed by the addition of 1 mL deionized water (acetonitrile: water= 1:3). The content is further stirred at room temperature for 1 h to facilitate the formation of nanoparticles. NPs thus formed was purified using

a 10 kDa Amicon® wash at 3500 rpm for 10 min. The washing was done three times in 1× PBS, made a final concentration of 1 mg/mL in 1× PBS, and stored at 4°C until further use. Similarly, control nanoparticles were prepared in the same phospholipid ratio without LyP-1-conjugated lipid. The third component being DOX which was physically adsorbed with 1 mg PLGA in acetonitrile and made the final volume of the mixture to 400 µL for nanoprecipitation. The near-infrared dye tracer (DiR dye) as an imaging probe was infused in lipid mixture by film hydration technique. In a typical experiment, 20 µg of dye was added to the lipid mixture and the solvent was evaporated to obtain the lipid film. The lipid film was dissolved in 4% ethanol and proceeded using nanoprecipitation under dark conditions.

4.2.5 Characterization of nanoparticles

The formation of the LyP-1-DSPE-PEG product was characterized using Fourier Transform Infrared Spectroscopy (FT-IR). The morphology of the nanoparticles was examined using transmission electron microscopy (TEM, FEI Technai G2 Spirit BioTWIN, 80KeV). The sample was loaded into the copper grid and dried over air followed by the staining with 0.1% uranyl acetate. The hydrodynamic size and zeta potential measurements of the NPs were monitored by dynamic light scattering (DLS) using a Malvarian Zeta sizer Nano®. In this instrument, the Brownian motion and the Smoluchowski equation were used to calculate the average hydrodynamic size and zeta potential value, respectively. The colloidal stability of NPs was investigated in both ionic and serum conditions to mimic the biological environment. In brief, 1 mg NPs dispersed in the medium were subjected to hydrodynamic size analysis over the period using DLS to obtain size, polydispersity index (PDI), and zeta potential values. The formulation with low PDI, high stability, and uniform narrow size distribution was selected for the *in-vitro* and *in-vivo* applications. Likewise, the stability of DiR dye in NPs was studied by assessing its release

kinetics in PBS. The release content of DiR was quantified spectrophotometrically with fluorescence excitation at 748 nm and emission at 780 nm. Finally, the presence of peptide on the nanoparticles was quantified using a colorimetric assay, the rapid gold BCA assay, according to the manufacturer's protocol.

4.2.6 Drug loading and release study

In a typical experiment, DOX was loaded LyP-1 tagged and control NPs by directly mixing of known concentration of DOX into the PLGA polymer followed by the nanoprecipitation technique.^{197–199} To optimize the maximum DOX loading, different calculated amounts such as 10, 25, 50, 100, 150, 200, 300, 400, and 500 µg of DOX were initially fed with 1 mg of PLGA dissolved in 400 µL acetonitrile solution. The amount of encapsulated DOX was quantified after purification spectrophotometrically using a UV-Vis spectrophotometer (Bio Tek Synergy2) with excitation at 485 nm and emission at 590 nm. The drug loading efficiency was calculated using the following equation:

$$\% \text{ Loading Efficiency} = (\text{Amount of encapsulated DOX} / \text{Amount of initial DOX input}) \times 100$$

Next, we studied the cumulative drug/dye release using 3.5 kDa molecular cut-off dialysis bags at physiological pH (pH 7.4, PBS). For this purpose, 150 µg/mL DOX input formulation was selected for further studies due to the stable physiochemical properties. An optimization experiment was performed using an aqueous solution of free DOX (25 µg/mL) placed in the dialysis tubing. Free DOX release from selected formulations was tracked throughout 72 h by dialysis. 1 mL of DOX-NPs containing 1 mg/mL of NPs was dialyzed in 100 mL PBS release media kept at 37 °C while constant stirring (80 rpm) to maintain the sink condition during the experiment. 1 mL of release media was taken at a regular interval and replaced by equivalent fresh media. The amount of free DOX in the release media was quantified spectrophotometrically and the cumulative release percentage was calculated using the following equation.

% cumulative DOX release = (DOX in release media/DOX in 100% release) ×100

The stability of DOX loaded NPs was studied by mixing 500µL of DOX-NP and 500 µL of PBS (1×) over the period to ensure the dispersity and colloidal stability of NPs in physiological media. The size and PDI of the particles after dispersed in PBS was measured for each 4th day for 7 weeks using DLS.

4.2.7 Cellular biocompatibility and cytotoxicity study

The *in-vitro* biocompatibility of NPs was conducted in K7M2 and NIH/3T3 cell lines using a colorimetric assay for assessing cell metabolic activity by 3-(4,5-Dimethylthiazol-2-yl)-2,5-diphenyltetrazolium bromide (MTT) assay. A time-dependent MTT assay was conducted as discussed in the literature.^{40,106,161,162} In the typical *in-vitro* experiment, the cells were cultured in DMEM containing 10% (v/v) fetal bovine serum and 1% (w/v) penicillin-streptomycin at 37 °C in 5% CO₂ and 95% air. Noncancerous and cancerous cells were used in this study and maintained according to the manufacturer's recommendation. In brief, at a density of 5×10³ cells per well in 96-well plate were incubated for 24 hours. The seeded cells were washed twice with 1X PBS to remove the debris before NP treatment. Then the medium was replaced with various concentrations of NPs (0.01, 0.1, 0.5, 5, 10, 25, 50,100, 200 µg/mL) suspended in DMEM. The control cell was maintained without treatment. After 24 h of incubation, cells were washed with 1× PBS to remove surface absorbed and excess NPs. After washing, 100 µL MTT (5 mg/mL in PBS, filtered through 0.22 µm syringe) reagent was added to each well following manufacturer's recommendation. Then the supernatant was aspirated followed by the addition of 100 µL DMSO for solubilizing formazan crystal. The plate gently shaken in an orbital shaker for 5 min in the dark and absorbance was recorded at 560 nm using a microplate reader (BioTek, Synergy H1 hybrid reader).

The *in-vitro* cytotoxicity of DOX loaded LyP-1 NP was conducted in mouse cells with targeted osteosarcoma and the non-targeted (normal) fibroblast using the MTT assay as discussed above in

biocompatibility measurement. We varied DOX concentration from 0.01 to 50 μM free DOX and NPs DOX. Data obtained was compared side by side with the control experiment to map the relative toxicity.

4.2.8 Intracellular uptake study

To evaluate the cellular internalization competence of LyP-1 NP, the experiment was conducted with mouse osteosarcoma and the noncancerous mouse fibroblast using confocal microscopy. For the confocal study, cells were seeded on poly-D-lysine coated eight chamber slides at a density of 50,000 cells per well and incubated for 24 h. Then the cells were treated with 50 $\mu\text{g}/\text{mL}$ rhodamine-labeled LyP-1 NP or control NP suspension prepared in complete DMEM and incubated for 3 h. After incubation, treated cells were washed twice with $1\times$ PBS (pH 7.4), fixed with 4% paraformaldehyde for 30 min at room temperature. The nucleus of the cells was stained with 4',6-diamidino-2-phenylindole (DAPI) for an additional 10 min and imaged under a confocal laser scanning microscope (Carl Zeiss, CLSM-700). RhB-labeled NP without having LyP-1 was used as the control particles. Cells without any treatment served as control cells. Comparative RhB fluorescence intensity in mouse fibroblast (NIH/3T3) and osteosarcoma (K7M2) cells were analyzed with CLSM. The quantitative percentage of fluorescence intensity was determined using the Image-J software. The quantification of the intensity of internalized RhB labeled NPs was calculated in terms of corrected total cell fluorescence (CTCF) by the use of the following equation:

$$\text{CTCF} = \text{Integrated Density} - (\text{Area of selected cell} \times \text{Mean fluorescence of background readings})$$

4.2.9 Fluorescence-activated cell Sorting (FACs) study

FACS study was conducted for quantitative cellular uptake to support the hypothesis. Following published protocol, the experiment for the FACS was conducted using RhB-labeled LyP-1 NP and RhB labeled non-targeted NP serving as a control particle.^{34,40,159} In brief, cells were

cultured in T25 flask up to around 80% confluency. Cell culture media was replaced by 4 mL of 50 µg/mL of RhB labeled NPs. After a pre-determined treatment time point, the media was removed, and cells were washed with 1× PBS three times and trypsinized. Finally, 1×10^6 cells were suspended in 500 µL of 1× PBS and cellular internalization was analyzed using BD LSR Fortessa X-20 Special Order Research Product Flow Cytometer. Control cells were maintained without any treatments. 10,000-gated events were collected for all measurements.

4.2.10 Biodistribution and *in vivo* imaging

Biodistribution study involves measuring NP concentrations in all major tissues after a single administration of NP over a period. NIR dye-tagged in NP is the probe to track the NPs *in vivo* for this study using lipid insertion technique.¹⁸ 20 µg DiR dye was added to 1000 µg both control and LyP-1 NPs and extruded using a 200 nm polycarbonate membrane filter for physical encapsulation of dye in NPs resulting in Control NP-DiR and LyP-1 NP-DiR. The encapsulation of 20 µg dye/mg NPs gave monodispersed sub-hundred nm size particles and used the next day for an imaging application. This dose of dye was chosen based on the literature.^{32,34,36,38} The solid tumor model using osteosarcoma cancer cells was developed by subcutaneous injection of 1×10^6 K7M2 cells into the rear flank of immunodeficient NU/NU nude mice (Charles River, 088/NU/NU homozygous). After 1 week of tumor induction or when the tumor size reaches about 6mm³, tumor-bearing animals were treated with respective NPs for the biodistribution studies. The time-course biodistribution patterns of different formulations were examined by NIR-fluorescence whole-body imaging using DiR as a tracer in the LI-COR[®] whole-body imaging system. DiR dye was labeled with NP according to the published protocol to obtain DiR labeled NPs.^{36,34,38} After a single dose post-injection of 10 mg/kg of NPs *via* lateral tail vein (100 µL volume), mice (n= 3) were imaged to map the real-time distribution of NPs at various time point *viz.*, 0.5, 1, 2, 3, 6, 12, 24,

and 48 h. The non-invasive imaging of mice was performed after anesthetized (2-3% isoflurane in 100% oxygen) and placed within a Pearl[®] Trilogy imaging system (LI-COR[®]). The 750nm channel was used to excite DiR and emission was observed at 800 nm. Fluorescent background images were acquired before NPs administration. When imaging animals, a fluorescent phantom was included in the image for calibration of the fluorescent intensity. After 48 h post-injection, animals were euthanized, and their selected organs including heart, lung, liver, kidney, spleen, brain, and tumor were collected, washed with 1× PBS, weighed, and imaged in the same imaging system to quantify DiR accumulation in organs using ImageStudio[™] software. DiR labeled NPs were quantified by selecting a region of interest (ROI) and plotted against signal intensity. All animal experiments were approved by IACUC, KSU.

4.2.11 Data and statistical analysis

The obtained data were plotted and compared to the significance of the results using GraphPad[®] software. Different statistical models and tests were carried out including T-test, F-test, and dose-response inhibition model fit using GraphPad software according to requirement. All data represent the mean ± standard deviation. Biocompatibility and cytotoxicity data include six replicates (n = 6). All other major data includes at least three replicates (n = 3).

4.3 Results and Discussion

4.3.1 Chemical characterization of LyP-1 lipid

The synthesis of the peptide conjugated lipid was carried using EDC/NHS bioconjugation chemistry as described in **Scheme 4.1 A** with a ~91% yield. The chemical structure of the synthesized LyP-1 peptide conjugated lipid DSPE-PEG was confirmed by Fourier-transform infrared (FT-IR) spectroscopy. As shown in **Figure 4.2 A**, the FT-IR spectrum of LyP-1- exhibits the characteristic

peaks of unmodified DSPE-PEG (spectrum in blue, upper panel) with additional functional absorption peaks (spectrum in red, bottom panel). The appearance of the broad and strong signal between 3169-3334 cm^{-1} is attributed due to the formation of an amide bond between the carboxylic group and the primary amine group from LyP-1 peptide after conjugation (spectrum in red, bottom panel).^{161,200} It is notable that after the conjugation, the shifting of the carbonyl C=O peak from 1730 to 1647 cm^{-1} (highlighted with black dotted line) with clear distinction absorption bands at 1647 cm^{-1} and at 1566 cm^{-1} , and the N-H out of plane wagging at 729 to 675 cm^{-1} (highlighted with black dotted arrow) confirms the successful peptide conjugation (**Figure 4.2 A**). The higher frequency band at 1647 cm^{-1} is characteristic of the amide-I band while the lower frequency band at 1566 cm^{-1} is amide-II which is largely due to the N-H bending trans to the carbonyl oxygen.²⁰¹ The bands at 2850 to 2952 cm^{-1} correspond to the aliphatic C-H stretch of the lipid backbone and symmetric and asymmetric C-O-C stretching (1170–1130 and 1050–950 cm^{-1}) belongs to DSPE-PEG moiety (**Figure 4.2 A**).^{161,202} The presence of peptide on the surface of the nanoparticles is characterized and quantified using a calorimetric rapid gold BCA assay according to the manufacturer's protocol (**Figure 4.2 B**).

4.3.2 Physiochemical characterization of NPs.

The physical morphology of the synthesized nanoparticles was measured using TEM, which shows highly monodispersed and uniform spherical particles with an average diameter of 68 ± 7 nm (**Scheme 4.1 C**). Similarly, the average hydrodynamic size of the LyP-1 NP was 79 ± 3 nm with a polydispersity index (PDI) of 0.183 ± 0.018 (**Figure 4.3 A and Appendix B- Figure 4.S1**), and the average surface zeta potential -39 ± 4 mV (**Figure 4.3 B**). Also, the control particle without LyP-1 showed a similar size and zeta potential with an average hydrodynamic size of 68 ± 4 nm and PDI of 0.161 ± 0.015 , and the average surface zeta potential of -37 ± 3 mV. The negative zeta potential is due to the surface carboxylate groups at the end moiety of the PEG corona. The size

from TEM and DLS measurements are in good agreement and demonstrates the monodispersity of the particles. The prepared nanoparticles (both control and targeted) were stable for a prolonged period as demonstrated in **Figure 4.3 C**. In the physiological condition of PBS pH= 7.4, we did not observe significant changes in size and PDI of both particles incubated over the weeks confirming the stability of the nanoparticles in the biological environment.

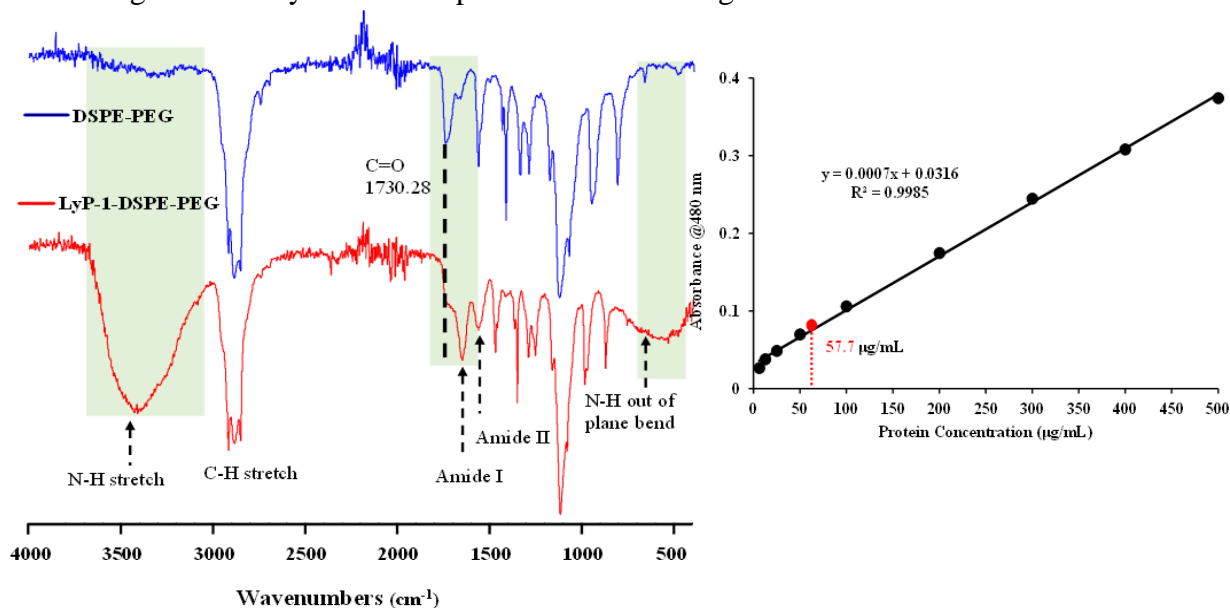


Figure 4.2 Chemical characterization of synthesized LyP-1-DSPE-PEG. FT-IR spectrum showing functional peaks of starting materials (DSPE-PEG) and product (LyP-1-DSPE-PEG). The LyP-1-DSPE-PEG spectra were taken with the lyophilized product (Left figure) and calibration curve for quantification of LyP-1 in NP using colorimetric Rapid Gold BCA Assay, Thermo Fisher Scientific Cat No: A53225 (right).

After the analysis of physicochemical properties, the drug encapsulation efficiency of NPs was evaluated by altering the initial doxorubicin (DOX) input concentration from 10 to 400 µg/mg of the PLGA. DOX loading was quantified spectrophotometrically at excitation and emission wavelength of 490 nm and 580 nm following the published protocol.^{77,161} The results showed that the initial DOX loading can be precisely tuned by varying the drug input (10, 25, 50, 100, 150, 200, 300, and 400 µg/mg of PLGA weight) during the NP preparation process. Among the different initial DOX feeding concentrations, the maximum encapsulation efficiency of the control NP was

found to be about 93% (**Figures 4.3 D and 3 E**). As expected, the similar encapsulation efficiency of DOX in both control and LyP-1 NP was observed with optimum 150 $\mu\text{g}/\text{mg}$ of feeding concentration, which accounts for 15% by weight of PLGA and about 78% loading efficiency. Due to the same PLGA core, the DOX content in both NPs (control and LyP-1 NP) were the same. Among these different formulations, 150 $\mu\text{g}/\text{mg}$ PLGA initial feeding input of DOX gave the most effective loading efficiency without altering nanoparticle physicochemical properties. However, in the case of higher DOX input formulations, in both NPs, resulted in lesser encapsulation and affected the physiological stability of the particles as indicated by rapid aggregation and precipitation. Therefore, we have chosen 150 $\mu\text{g}/\text{mL}$ input formulation as a candidate for further experiments. No significant changes in the size and PDI of this formulation were observed when

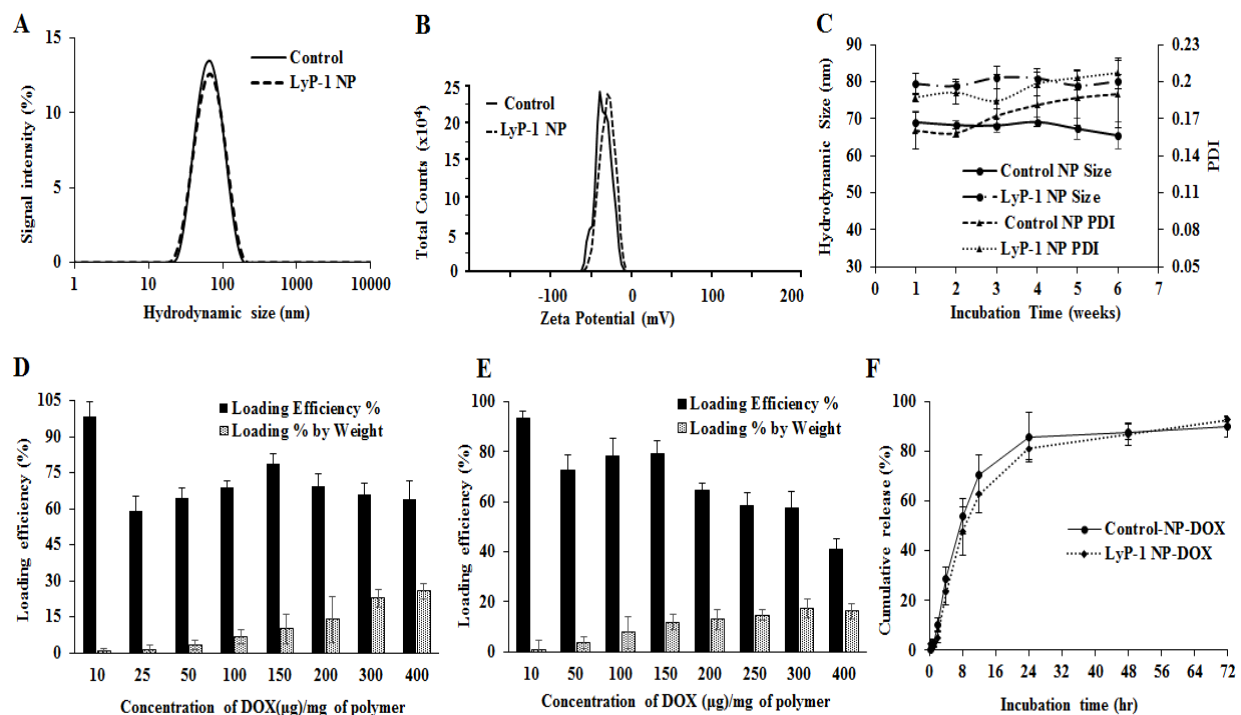


Figure 4.3 Physicochemical characterization, drug loading, and release study of NPs. (A) Dynamic light scattering showing the average hydrodynamic size of NPs, (B) Surface charge zeta potential of NPs, and (C) Stability study of control and LyP-1 NP in PBS (pH = 7.4). (D) Comparative DOX loading efficiency of control NP with various initial input feeding concentrations of DOX (10–400 μg), (E) Comparative DOX loading efficiency of LyP-1 NP with various initial input feeding concentrations of DOX (10–400 μg), and (F) Comparative drug release characteristics of Control-DOX and LyP-1-DOX in PBS (pH = 7.4) after 72 h incubation. Data represent mean \pm SD, n = 3.

incubated at 37 °C for 5 days (**Figure 4.4 A**) and over 7 weeks period stored at 4°C in PBS (pH=7.4) confirming the excellent physiochemical property (**Figure 4.4 B**).

To learn the release efficiency of the drug from NPs, 2 mL of 1 mg/mL Control-NP-DOX and LyP-1-NP-DOX were placed in a dialysis bag and processed under identical conditions. We observed similar time course DOX release kinetics for both Control-NP-DOX and LyP-1-NP-DOX over a 72 h period at 37 °C. The results, as shown in **Figure 4.3 F**, indicated that about 16% DOX was released within a period of 6 h from both NP types. While through 12 h, we observed a slight difference in drug release kinetics by below 8% in LyP-1 NP, however, there is no significant difference in overall kinetics through 72 h. Whereas compared to DOX release, we found a higher order of DiR dye stability in NPs (**Appendix B-Figure 4.S2**). Less than 13% DiR released throughout the release study, 72 h (**Figure 4.4 C**) consistent with the literature.³⁴ The stability of DiR is highly essential to device NPs as theranostics.

4.3.3 Biocompatibility Study.

Cellular compatibility and therapeutic efficacy of LyP-1 NPs, with and without the drug, were studied using mouse normal fibroblast (NIH/3T3) and osteosarcoma (K7M2) cells. We used DOX in our study because the current clinical treatment protocol against osteosarcoma includes DOX as one

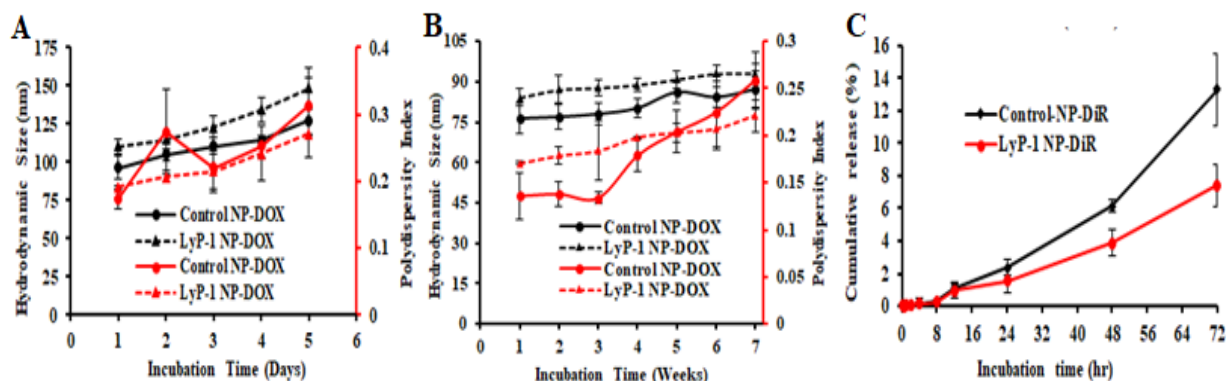


Figure 4.4 Stability study of drug and dye. (A) Stability of control NP-DOX and LyP-1 NP-DOX in PBS (pH = 7.4) at 37°C (n=3). B) Stability of control NP-DOX and LyP-1 NP-DOX in PBS (pH = 7.4) at 4°C (n=3). C) Comparative DiR dye release characteristics of Control-NP-DiR and LyP-1 NP-DiR NPs in PBS (pH = 7.4) after 72 h incubation. Data represent mean \pm SD, n = 3.

of the important chemotherapeutics along with Methotrexate and Cisplatin.²⁰³ For biocompatibility study, various concentrations of LyP-1 NP were incubated with K7M2 and NIH/3T3 cells as presented in **Figure 4.5** for 24 h. A cell without NP treatment was used as an experimental control and non-targeted NP as an NP control. Control NP showed at least 82% cell viability even at high nanoparticle concentration (200 $\mu\text{g}/\text{mL}$) in both K7M2 and NIH/3T3 cells. More specifically, in the particle concentration window from 10 $\mu\text{g}/\text{mL}$ to 200 $\mu\text{g}/\text{mL}$, both cell lines showed similar viability. In the case of LyP-1 NP, the cell viability with particle concentrations from 10 $\mu\text{g}/\text{mL}$ to 200 $\mu\text{g}/\text{mL}$ ranges from 93% to 79% in K7M2 cells and 100% to 83% in NIH/3T3 cells, respectively. This higher cell viability even at high NPs concentrations puts it as an excellent candidate for drug delivery (**Figures 4.5 A and C**). The extent of cytotoxicity of NPs depends on its cellular internalization efficiency. The compatibility of NPs relies on the interaction of healthy cells with the NPs, in such a way that NPs will enhance or retards the growth phase of the cells under living conditions.¹⁰⁶ At lower NPs concentration, no significant toxicity related to both non-targeted and targeted were observed indicating the excellent biocompatibility of NPs in the tested cells. However, when the concentration increases up to 150 $\mu\text{g}/\text{mL}$, cell viability was decreased by 15% (total viability at this concentration was 85%) for both cell lines used in the study, which could be a dose effect in limited culture area of 96 well plates. The results of the biocompatibility of these NPs are consistent with previous findings on lipid polymer containing NPs.^{160,161,172,174,199,204}

4.3.4 Cellular cytotoxicity study

In a typical cellular cytotoxicity experiment, DOX-loaded NPs and equivalent of free DOX were used against K7M2 and NIH/3T3 cells. The results have shown that both free DOX and DOX-loaded NPs exhibit a time- and dose-dependent cytotoxic effect (**Figures 4.5 B and D**). The lower concentration of the drug-loaded NPs showed lower cytotoxicity than free DOX against K7M2

after 24 h post-treatment. In contrast, about 10% enhanced cytotoxicity of DOX-loaded NPs was observed as compared to free DOX with the higher dose (10 μ M). Notably, free DOX showed higher cytotoxic behavior with noncancerous cells throughout the range of concentrations used than DOX-loaded NPs. However, enhanced toxicity was observed in both cells in the case of LyP-1NP-DOX with higher payload compared to control-NP-DOX. The dose-dependent cytotoxic effect of LyP-1 NP-DOX is likely due to nanoparticle's internalization mechanism. First, it could be attributed due to the presence of tumor-targeting LyP-1 peptide that can recognize and binds to the p32 receptor proteins overexpressed on the surface of cancer cells leading to higher accumulation and distribution throughout cancer cell as compared to non-cancerous cells.^{106,205,206} This p32 receptor-mediated endocytosis as reported in the literature^{106,205,206} increases localized intracellular drug concentration whereas in the case of free DOX that diffuses slowly into the cell limiting localized drug concentration. Although no statistically significant difference was observed for the targeted and non-targeted NPs against cancer cells (*p-value* >0.05, two-way ANOVA), it is worth noting that a two-dimensional culture system, where density induced NP cell surface interaction is accounted, can interfere with cell viability and may limit actual representation of toxicity.^{177,207,208} Therefore, we further studied quantitative cellular internalization studies to validate the receptor-mediated uptake of NPs.

4.3.5 Cellular uptake studies

Cellular uptake is an important biological property that dictates therapeutic effectiveness. A tumor-targeted internalization property of nanoparticulate drug delivery system can not only enhance toxicity against tumor cells but also can reduce off-target toxicity. To analyze the tumor-targeting behavior of Lyp-1 NPs, a cellular uptake study was carried out in K7M2 and NIH/3T3 cells *via* confocal microscopy following 3 h incubation of rhodamine B (Rh-B) labeled NPs (**Figures 4.6**). The 3 h incubation time point was chosen based on our previous study where the

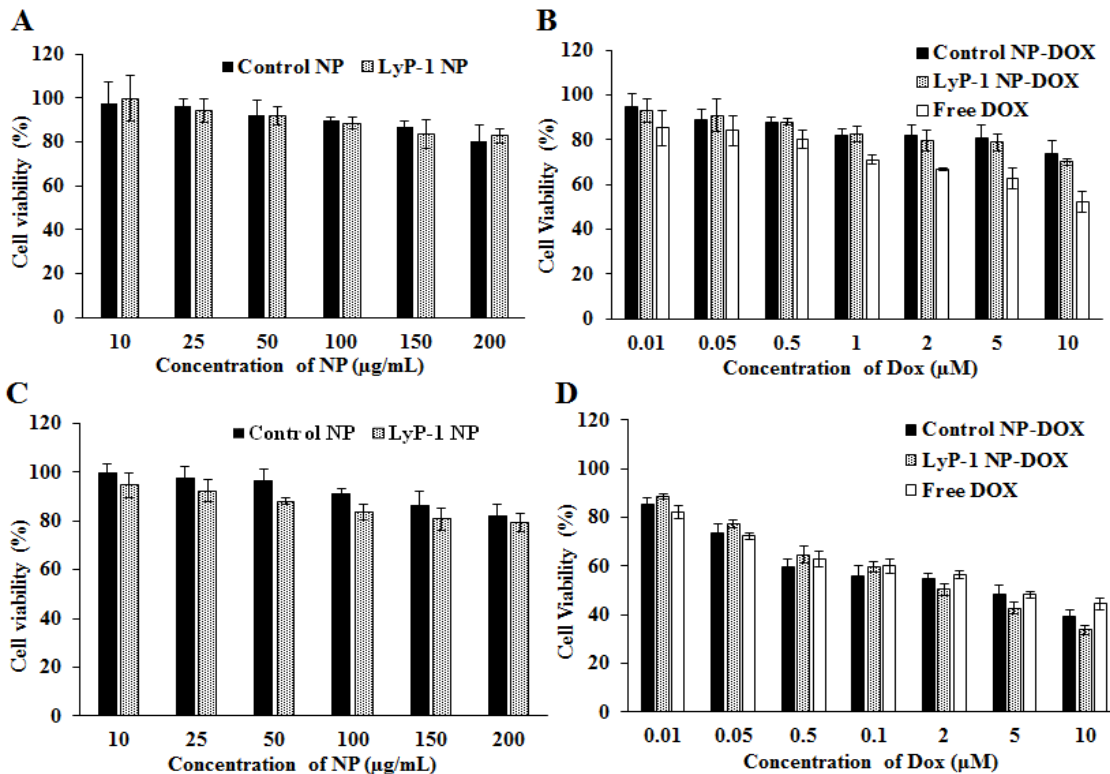


Figure 4.5 Comparative cellular interaction study of control NP and LyP-1 NP against mouse fibroblast (NIH/3T3) and osteosarcoma (K7M2) cells. (A) Concentration-dependent biocompatibility of control and LyP-1 NP and (B) comparative cytotoxicity of free DOX, control NP-DOX, and LyP-1NP-DOX against NIH/3T3 cells after 24 h post-treatment, respectively. (C) Concentration-dependent biocompatibility of control and LyP-1-NP and (D) Comparative cytotoxicity of free DOX, Control NP-DOX, and LyP-1-NP-DOX against K7M2 cells after 24 h post-treatment, respectively. Data represent mean \pm SD, $n = 6$. p -value > 0.05 , two-way ANOVA for the targeted and non-targeted NPs against K7M2 cells, p -value summary- n. s.

internalization of NPs reached a maximum at 3 h.^{40,206,209,210} **Figure 4.6** shows the confocal imaging of the cells showing the internalization of NPs and their corresponding quantification in terms of corrected total cell fluorescence in K7M2 cells. Untreated cells were used as control. As shown in **Figure 4.6 B**, the fluorescence intensity of the LyP-1 NP-RhB was significantly higher than that of Control NP-RhB nanoparticle ($p < 0.0001$, unpaired t-test). On the other hand, no significant difference in NPs uptake was observed for the noncancerous NIH/3T3 cells (**Figures 4.6 C-D**). This observation indicates that LyP-1 NP-RhB were preferentially taken up by K7M2 cells supporting our hypothesis of receptor-mediated uptake due to LyP-1 in NPs.

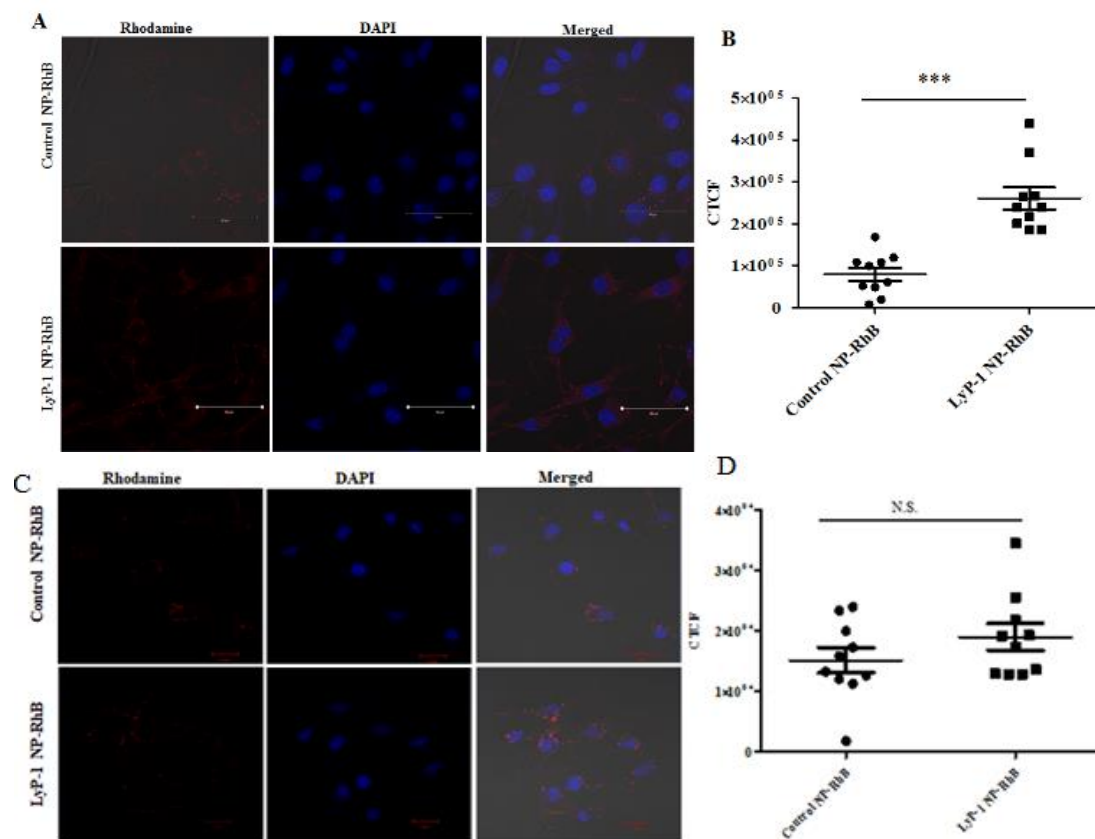


Figure 4.6 Cellular internalization study in cancerous and non-cancerous cells. (A) Comparative confocal images of K7M2 cells incubated with LyP-1 NP-RhB and control NP-RhB (50 $\mu\text{g}/\text{mL}$) for 3 h at 37 $^{\circ}\text{C}$. (B) Corresponding quantification of internalized NPs following corrected total cell fluorescence (CTCF) using ImageJ. (C) Comparative confocal images of NIH/3T3 cells incubated with LyP-1 NP-RhB and control NP-RhB (50 $\mu\text{g}/\text{mL}$) for 3 h at 37 $^{\circ}\text{C}$. The nuclei of the cell were stained by DAPI (blue). (D) Corresponding quantification of internalized NPs following CTCF. The cells were imaged under a 20 \times lens and 50 μm scale bar. Unpaired t-test, p -value <0.0001, p -value summary-***.

To further support our confocal results, the targeting property of NPs was confirmed by quantitative cellular uptake studies using FACS. As the LyP-1 NP has targeting ligand from the LyP-1 peptide on the surface, the differential targeting ability is expected to be more in the cancer cells. Based on the literature for the overexpression of p32 in bone cancer^{188–190,211,212}, we expect LyP-1-modified nanoparticles to specifically target K7M2 cells. The quantitative cellular uptake of NPs was evaluated at 3 h incubation for both control and targeted NPs, experiments carried under identical conditions with both cell types, K7M2, and NIH/3T3 cells.^{40,206,209,210} As shown in

the (Figure 4.7 A), the overlapping of the histogram from control NP-RhB and LyP-1 NP-RhB showing no significant difference in internalization behavior was observed in NIH/3T3 cells. On the other hand, LyP-1 NP-RhB showed a right shift in Figure 4.7 C demonstrating higher cellular uptake than control NP-RhB. This observation was further analyzed by taking the median fluorescence value of NPs internalized into cells. Figure 4.7 D shows the significantly higher fluorescence intensity of the LyP-1 NP-RhB as compared to the control NP-RhB (p -value <0.0001 , unpaired t-test). Both confocal imaging and flow cytometry analysis confirmed the selective internalization of LyP-1NP-RhB towards tumor cells supporting our hypothesis.

In the similar studies, Pang et al. reported that the RPARPAR peptide coated 50 nm gold nanoparticles (AuNPs) were taken up by primary prostate carcinoma-1 cells in a glucose-dependent manner and internalized through neuropilin-1 (NRP-1), a cell surface receptor with multiple ligands that binds through a CendR motif, mediated endocytosis *via* mammalian target of rapamycin (mTOR) signaling pathway.²¹⁰ AuNPs coated with a control peptide did not bind to NRP-1 and were not taken up into cells in the absence of glucose. RPARPAR peptide has a CendR motif similar to that of LyP-1 peptide. The CendR pathway could be ascribed for the localized LyP-1 NP uptake similar to that of the previous studies.²¹⁰ When LyP-1 NPs get into the endosome, the higher endosomal pH will breakdown the ester bond present in the lipid-polyethylene glycol moiety resulting in destabilization of the particles. Then the fusion of the lipid shell with the endosomal membrane could allow the cargo to escape from the endosomal degradation and release into the cytosol.

4.3.6 *In-vivo* biodistribution study

NIR fluorescent probes such as DiR dye have many advantages in imaging applications

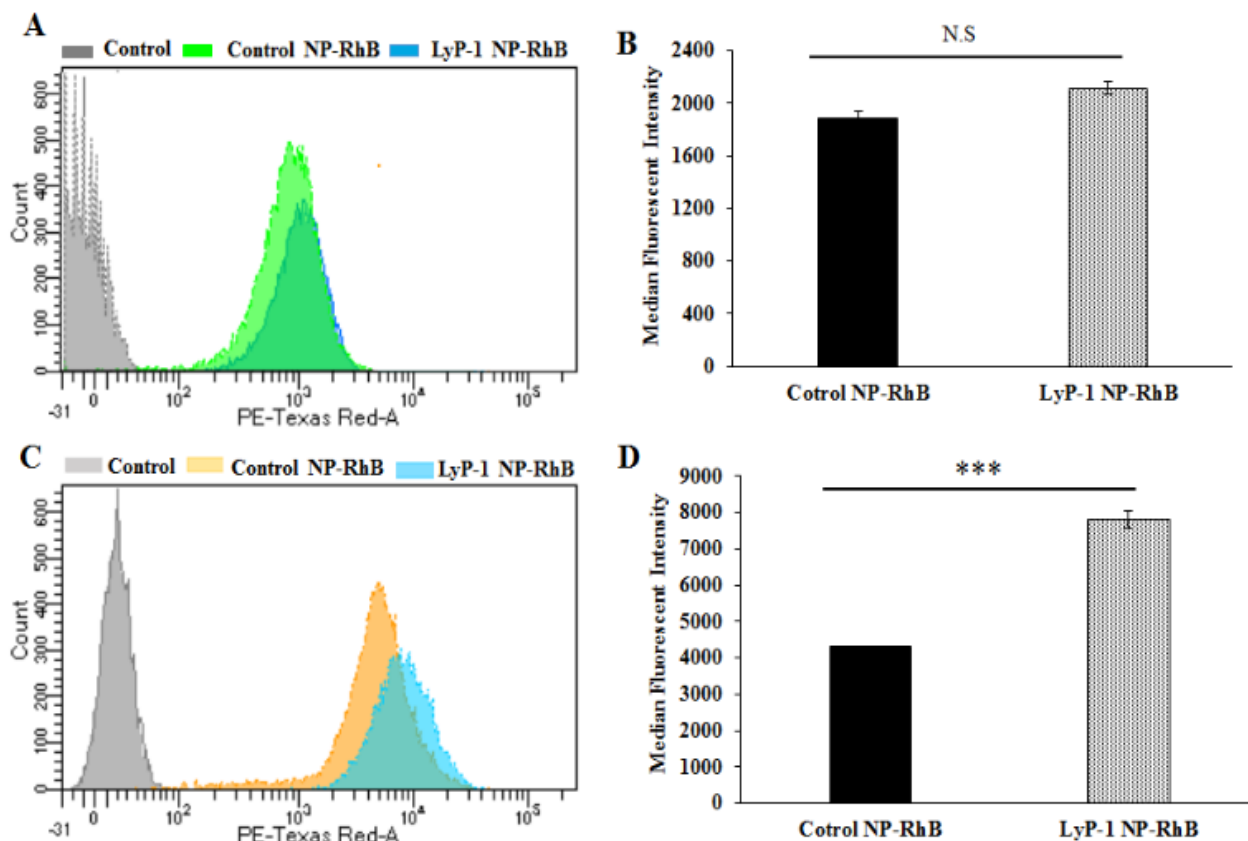


Figure 4.7 Fluorescent activated cell sorting (FACS) experiment for quantification of internalized NPs. (A) and (C) are histograms showing a comparative cellular uptake study by Control NP-RhB and LyP-1 NP-RhB against NIH/3T3 and K7M2 cells, respectively. (B) and (D) are corresponding quantitative data in terms of average median fluorescent intensity (MFI) for control and LyP-1 NP. Cells were treated 50 $\mu\text{g}/\text{mL}$ RhB labeled particles and incubated for 3 h before data acquisition. Data represent mean \pm SD, $n = 3$. (Statistics: Unpaired t-test, p value= 0.1669, non-significant for NIH/3T3, and p value<0.0001 for K7M2 respectively).

including minimum tissue autofluorescence, real-time visualization, minimum photo-bleaching, maximum tissue penetration, and photo-damage.^{213–217} Therefore, near-infrared fluorescent probes are being developed and used in optical imaging for the visualization of biological phenomena in the living system. To examine the effect of versatility in surface modification and confirm the accumulation in the tumor, we tagged the NPs by DiR dye and compared both targeted and non-targeted NPs. DiR in NPs become the part of the lipid building block of nanoconstruct. We investigated the biodistribution of DiR labeled NPs in K7M2 tumor-bearing NU/NU mice following intravenous injection of 10 mg/kg NP dose. LI-COR[®] whole-body imaging system was used to monitor the real-time biodistribution and

tumor homing efficiency of LyP-1 NP-DiR (**Figure 4.8**). The images were spectrally processed using Image Studio ver5.2[®]. The emission of the dye was isolated from autofluorescence and quantified as the region of interest (ROI) indicated on the corresponding graphs (**Figures 4.8 B and C**).

Figure 4.8 A shows the overall distribution of fluorescent-tagged NPs in K7M2 tumor-bearing mice. We observed the rapid extravasation of the control NP into the tissue showing localized intensity as compared to LyP-1-NP-DiR. Also, we observed control NPs-DiR distributed quickly (**Figure 4.8 A**) throughout the body as early as 1 h point. However, LyP-1-NP-DiR did not show much accumulation during this period. We observed significant tumor uptake of both NPs more specifically at 12 h post-injection. However, with time, we didn't observe enhance tumor intensity in control NP-DiR treated mice as it distributed throughout the body. In contrast, mice treated with LyP-1-NP-DiR have shown tumor uptake over the period (**Figure 4.8 B**) thereby supporting our hypothesis of receptor-mediated targeting while minimizing unwanted distribution throughout the body. Similar enhanced uptake has been reported in previous publications.^{188-190,211,212} To further understand the tissue distribution, we euthanized mice after 48 h post-injection and harvested organs were studied for NP accumulation. **Figure 4.8 D** shows the accumulation of Control NP-DiR and LyP-1 NP-DiR into vital organs and blood in terms of percentage injected dose (ID) per weight of tissue (g). Control NP-DiR retained mainly in the liver (4.09%), spleen (5.43%), and blood (6.09%). In contrast, LyP-1 NP-DiR, showed retention in liver (3.15%), spleen (3.28%), tumor (1.16%), and blood (19.20%). Notably, we observed that more than three-fold high retention in the blood even after 48 h post-injection (19.2% vs 6.09%) suggesting excellent blood retention characteristic of LyP-1 NP-DiR (**Appendix B-Figure 4.S3**). This suggests the blood availability of LyP-1 NP-DiR, thereby providing its long-circulating properties (**Figure 4.8 D**). The time-course pharmacokinetic and biodistribution studies are needed for further confirmation

as warranted by this observation. Unsurprisingly for nanoparticles above the glomerular filtration capacity, it is expected that these particles were cleared mainly through the reticuloendothelial system (liver and spleen) uptake, which can be seen in **Figures 4.8 C, D, and E**. Furthermore, LyP-1 NP-DiR

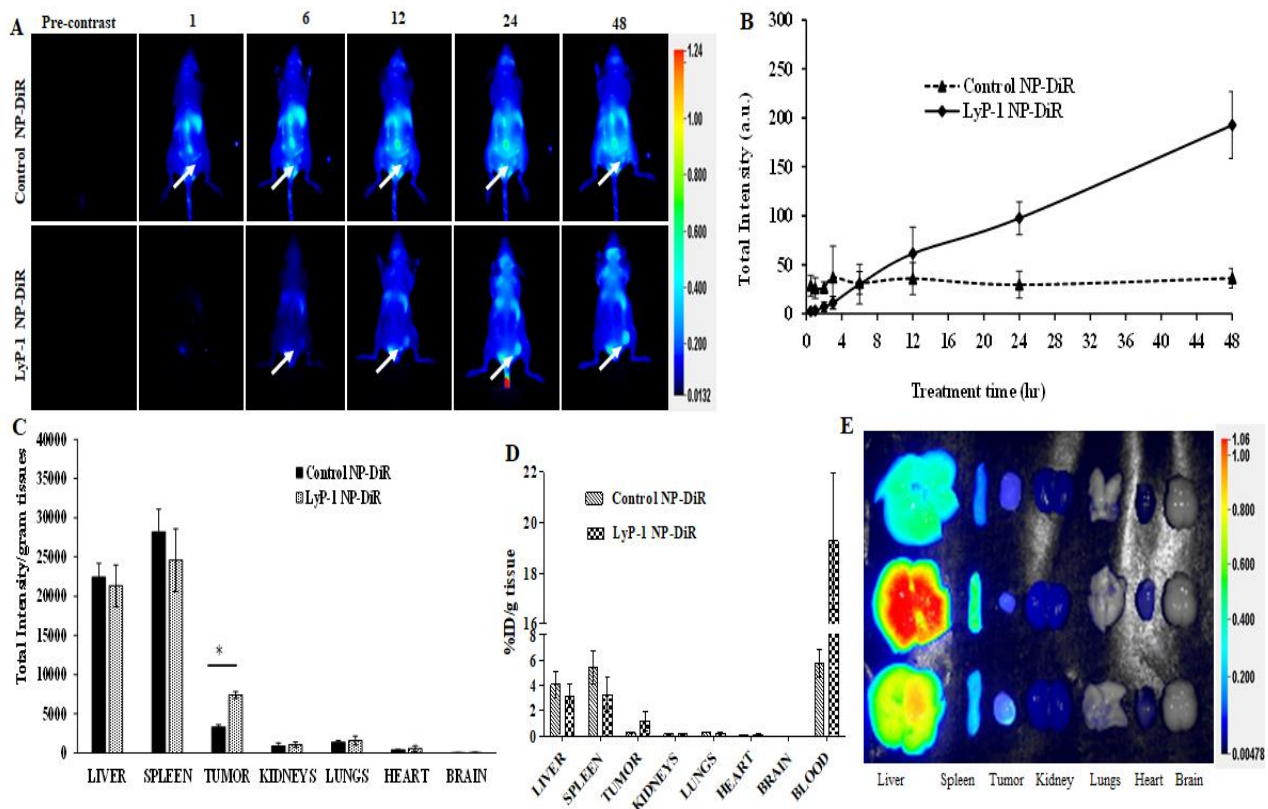


Figure 4.8 *In-vivo* biodistribution of NPs using fluorescence imaging. (A) Time-dependent real-time animal imaging of K7M2 tumor-bearing NU/NU nude mice after intravenous injection of DiR-labelled NPs (10 mg/Kg). Images were recorded before injection (pre-contrast) and after 3, 6, 12, 24, and 48 h post-injection of single-dose, respectively. (B) Quantification of time-dependent accumulation of control and LyP-1 NP-DiR in tumors by measuring the intensity of dye in the region of interest (ROI). (C) Comparative bioaccumulation of control and LyP-1 NP-DiR in different organs imaged ex-vivo after 48h post-injection. (D) Quantification of tumor accumulation of control and LyP-1 NP-DiR. (E) Comparative biodistribution of LyP-1 NP in various organs after 48 hr post-injection imaged for DiR dye in Li-COR® whole-body imaging system. p value= 0.0169, * (F-test). Data represent mean \pm SD, n = 3.

showed more than three times higher deposition of NPs into the tumor region than that of non-targeted counterparts (**Figure 4.8 C**). This strongly supports the notion of tumor targeting and homing potential of LyP-1 peptide. It is also reported that *in vivo* study of cationic liposomal formulation fabricated with aptamer tends to accumulate more in the liver, spleen, and kidney suggesting reticuloendothelial

system uptake.^{218,219} The higher tumor accumulation of LyP-1 nanoparticles could be attributed that the LyP-1 peptide tends to accumulate more in the tumor microenvironment and drags more amount of bulk nanoparticles towards the target site by activating the CendR pathway.^{186,220,221} The active tumor accumulation largely depends on the overexpression of cell receptor ligands p32 in tumor cells.^{179,184,186–188,222–224} This result strongly corroborates with previous studies using cell membrane infused liposomal system and targeted polymeric nanoparticles for the targeted tumor therapy and bioimaging.^{36,159,225,226}

4.4 Conclusion

In summary, we describe a simple and versatile nanoformulation strategy by combining the synthetic lipids, biocompatible polymer, and tumor homing peptide into a composite nanosystem for targeted drug delivery and imaging in a single session. It is evident from our results that the LyP-1 navigated the nanoconstruct into the tumor region showing its promise in precision drug delivery in the experimental tumor conditions. Moreover, the hybridization of lipid-polymer with different physiochemical properties could be beneficial to overcome the respective shortcomings to design a robust drug delivery system due to the coexistence of hydrophobic and hydrophilic nature. Overall, this will eventually open the opportunity for the mapping of the many experimental carcinomas for therapeutic planning and image-guided therapy.

Chapter 5 - Iron (III) chelated paramagnetic polymeric nanoparticle as next-generation T₁-weighted MRI contrast agent

Abstract

Magnetic resonance imaging (MRI) is a routinely used imaging technique in medical diagnostics. To enhance the quality of MR images, contrast agents (CAs) are used, which account for nearly 40% of contrast-enhanced MRI (Ce-MRI) exams in the clinic benefiting millions of patients globally. The most used CAs are gadolinium-based contrast agents (GBCAs) but the use of GBCAs has been linked with gadolinium metal-deposition in various organs including the brain, bone, and skin. Gadolinium deposition has shown to be correlated to lead nephrogenic systemic fibrosis, a kidney disease characterized by poor kidney function, and as such, there is no alternative CAs for the patients with a kidney disorder. Moreover, due to the GBCA associated potential toxicities, some clinically approved GBCAs have been suspended or strict guidelines have been issued for careful consideration of risk versus benefit. Therefore, there is an unmet need for the development of a new CAs alternative to GBCAs for T₁-weighted Ce- MRI. Herein, we designed paramagnetic ferric iron (III) ions chelated poly lactic-co-glycolic acid nanoparticles and routinely examined its application in Ce-MRI using clinical and ultra-high-field MRI scanner. Iron (III) chelated polymeric nanoparticles were prepared by nanoprecipitation and characterized its physicochemical properties and iron loading content. Nanoparticles were monodispersed and highly stable in physiological pH over one month's period with the hydrodynamic size of 130 ± 12 nm polydispersity index of 0.231 ± 0.026 . The T₁-contrast efficacy of the nanoparticles was compared with commercial agent gadopentetate dimeglumine called Magnevist[®] in aqueous phantoms *in vitro* and then validated *in vivo* by visualizing angiographic map in a clinical MRI scanner. Relaxivities of nanoparticle in aqueous environment were $r_1 = 9.86 \text{ mmol}^{-1} \cdot \text{s}^{-1}$ and $r_1 = 2.86$

mmol⁻¹.s⁻¹ at 3.0 T and 14.1 T measured at room temperature and pH 7.4, respectively. The clinically relevant magnetic field relaxivity is three times higher compared to the Magnevist[®], a clinical GBCAs, signifying its potential applicability in clinical settings. Therefore, paramagnetic iron-based nanoscale CA shows great promise for next-generation of T₁-weighted CAs serving as a replacement for gadolinium and has the potential to contribute to the safety of MR imaging. Moreover, iron is an endogenous metal with known metabolic safety, and polymer and phospholipids used in the nanoconstruct are approved biodegradable and biocompatible components from concerned authorities, these properties further put the proposed T₁ agent in a promising position in Ce-MRI of the patient with any disease conditions.

5.1 Introduction

Magnetic resonance imaging (MRI) is one of the prominent noninvasive imaging modalities to provide images with unprecedented anatomical details based on soft-tissue contrast and functional information in real-time.²²⁷⁻²²⁹ The quality of the MR image is enriched using contrast agents (CAs), by the perturbation of nearby water protons' longitudinal (T₁) or transverse (T₂) relaxations time in the body. Most clinically used MRI CAs include gadolinium(Gd)-based contrast agents (GBCAs), which account for about 40% of contrast-enhanced MRI (Ce-MRI) scans among about 1 billion global MRI exams benefiting millions of patients globally.^{176,230} CAs help physicians diagnose and treat a variety of pathophysiological procedures by improving the visualization of specific organs, tissues, and blood vessels. CAs improve the effectiveness of MRI by altering the molecular motions and compositions with respect to the characteristics of the surrounding tissues in a living subject thereby altering the surrounding contrast. Based on the underlying physical relaxation mechanisms, two types of MRI contrast agents, positive (T₁-weighted) and negative (T₂-weighted), are used.^{231,232} In general, paramagnetic Gd(III) complexes

are most predominant among T₁-agents while superparamagnetic iron oxide nanoparticles (SPIONs), for example, e.g. Feridex[®] and Revoisit[®], are typical T₂-agents, used in Ce-MRI.^{32,233–237} However, recent reports have shown that the widespread application of GBCAs led to Gd deposition in the organs including the brain, bones, and skin raising serious safety concerns.^{238–240} The long-term health consequences of Gd retention in tissue is, however, unknown, but it raises additional concerns about the long-term safety profile of GBCAs, particularly patients that require frequent Ce-MRI exams for disease surveillance.²⁴¹ According to the National Institute of Diabetes and Digestive and Kidney Diseases (NIDDKD) more than 661,000 Americans have kidney failure. Of these, 468,000 individuals are on dialysis, and about 193,000 live with a functioning kidney transplant.²⁴² Moreover, the overall prevalence of chronic kidney disease in the general population is approximately 14 percent.²⁴² The use of GBCA in these populations is fatal. These results prompted the European Medical Agency to suspend some of the clinically approved GBCAs and the Food and Drug Administration (FDA) of the United States has added warning labels on these agents.^{243,244}

Increasing awareness of the potential risks associated with Gd metal has revealed an unmet need for the development of alternative, Gd free, CAs for T₁-weighted MR imaging. In pursuit of safer alternatives to Gd, the bulk of research has focused on the SPIONs based CAs which can also be categorized as the first generation of iron-based CAs.^{233,237,245–248} However, several clinical SPIONs have already been discontinued due to toxicity and a lack of clinical benefit in imaging.²⁴⁹ On the other hand, less attention has been given to the potential application of ferric iron (Fe³⁺) as the next generation of T₁ based CAs. The paramagnetic metal ion, Fe³⁺ with five unpaired electrons has high longitudinal relaxivity and unlike Gd, iron is an essential element that is naturally found in the body and has clear metabolic pathways, for example, endosomal degradation and

hepatobiliary excretion.^{236,250,251} However, one concern remains is the possible toxicity associated with the aqua ions of paramagnetic metals, therefore, a variety of ligands have been employed to chelate free metals ions. For example, catechol ligands have a high affinity and binding capacity to coordinate Fe^{3+} cations, which have been widely applied in biomaterials.^{252,253} Although the standard tris-catecholate- Fe^{3+} complexation is simple for Fe^{3+} encapsulation, only a handful of reports have been published as T_1 -weighted MRI CAs.^{246,254–258} In the past, small molecular Fe^{3+} chelates of ethylenediaminetetraacetic acid, pentetic acid, and trans-cyclohexane diamine tetraacetic acid as low-molecular-weight T_1 CAs have been reported.^{259,260} These small molecular Fe-chelates did not show any better contrast efficacy compared to GBCAs limiting further translation to the clinic. Alternatively, there are some Fe-based nanoparticulate systems designed and tested in the preclinical model to improve the relaxivities. For example, Fan et al. designed multifunctional Fe^{3+} -chelated melanin-like nanoparticles (NPs) with $r_1 = 1.2 \text{ mM}^{-1} \cdot \text{s}^{-1}$ and found an increase in signal intensity in the tumor region when used with RGD-peptide linked NPs at 4 h post-injection (1.0 T, 25 °C).²⁶¹ Similarly, Miao et al. reported the $r_1 = 5.6 \text{ mM}^{-1} \cdot \text{s}^{-1}$ from Fe^{3+} -chelated poly-3,4-dihydroxy-l-phenylalanine-b-polysarcosine nanoparticles using 3.0 T magnetic field at 20 °C.²⁵⁶ However, these approaches were mainly limited due to the restricted control over the synthetic colloidal chemistry hindering size and shape control and inherently lower relaxivity value.²⁵³ In contrast, poly-lactic glycolic acid (PLGA) is widely applied in biomedical fields, such as controlled drug release, gene delivery, stimuli-responsive biomaterials, and nanoscale self-assembly systems due to its excellent biocompatibility and biodegradability.^{36,34,37,262–265,172} Carboxylate terminated PLGA NPs could offer complexation with Fe^{3+} and help make overall NPs charge distribution effective for cellular uptake. Herein, we test our hypothesis that Fe^{3+} encapsulated PLGA nanoparticles will give comparable relaxivity with equivalent to the GBCAs.

We studied the relaxivity of Fe-PLGA NPs at low field (3.0 T) and ultra-high-field (14.1 T) in aqueous solutions and compared it with Magnivist[®], a clinical GBCA. We demonstrate three-fold enhancement of the relaxivity of Fe³⁺-PLGA NPs at the clinically relevant field and offer a Gd free alternative platform for next-generation of iron-based T₁-weighted nanoscale CA for Ce-MRI.

5.2 Materials and Methods

5.2.1 Material and chemical

Carboxylic end group terminated PLGA (lactide: glycolide = 50:50 dLg⁻¹) was purchased from DURECT Corporation (USA) and used after purification by repeated precipitation in diethyl ether. 1, 2-Distearoylphosphatidylethanolamine polyethylene glycol succinyl (DSPE-PEG-COOH) and phospholipid conjugated l- α -phosphatidylethanolamine-N-(lissamine rhodamine-B sulfonyl) (Ammonium Salt) (RhB) was purchased from Avanti Polar Lipid Inc (Alabaster, AL, USA). DAPI (4',6-Diamidino-2-phenylindole dihydrochloride, acetonitrile, and dimethyl sulfoxide (DMSO) were purchased from Sigma-Aldrich (Saint Louis, MO, USA). (3-(4,5-dimethylthiazol-2-yl)-2,5-diphenyl tetrazolium bromide) (MTT) was purchased from Thermo Fisher Scientific, USA. All other analytical grade reagents and solvents were used without further purification.

5.2.2 Cell line and animal model

Breast cancer (MCF-7) cells from American Type Culture Collection (ATCC) were maintained in Dulbecco's Modified Eagle's Medium (DMEM) with 10% (v/v) fetal bovine serum (FBS) and penicillin/streptomycin (100 μ g/mL) and maintained at 37 °C in 5% CO₂ environment.

Six-week-old female NU/NU nude mice were procured from Charles River Laboratories International, Inc. and used for the study after ten days of acclimatization. All animal experiments

and protocols were approved by the Institutional Animal Care and Use Committee (IACUC) and Institutional Biosafety Committee (IBC), Kansas State University, Manhattan, Kansas.

5.2.3 Preparation of paramagnetic polymeric nanoparticles

Paramagnetic polymeric NPs were prepared by the nanoprecipitation technique following our established protocol.^{33,36-38} In brief, the paramagnetic PLGA cores were prepared by adding dropwise 100 μ L of PLGA (10 mg/mL, acetonitrile) containing various amounts of iron(III) chloride hexahydrate (10, 20, 50, 100, 150, 200, and 400 μ L (0.1 M FeCl₃, acetonitrile) was added dropwise into 3 mL Milli-Q water containing 200 μ g/mL lipid suspension under magnetic stirring at 60 °C. Control PLGA NPs were fabricated similarly without encapsulating Fe³⁺. The mixture was stirred continuously overnight to evaporate off the organic solvent. The sample was further purified using Amicon Ultra-4 centrifugal filter (Millipore, MA) with a molecular weight cut-off of 10 kDa and stored at 4 °C for further use. Rhodamine dye-labeled Fe-PLGA or PLGA NPs were prepared by mixing 20 μ g of L- α -Phosphatidylethanolamine-N-(lissamine rhodamine B sulfonyl) (Ammonium Salt) with lipid suspension before the fabrication of paramagnetic polymeric core.

5.2.4 Characterization of Fe-PLGA

The hydrodynamic size and zeta potential of the Fe-PLGA NPs were characterized using dynamic light scattering analysis (Malvern, Nano ZSP). The morphology of Fe-PLGA NPs was further confirmed using a transmission electron microscope (FEI Technai G2 Spirit BioTWIN). TEM samples were prepared by incubating 20 μ L of Fe-PLGA (1 mg/mL) with 20 μ L of 0.1% Uranyl acetate for 5 mins at room temperature. The sample was then placed on a formvar coated copper grid (400 mesh) and let stand for an additional 10 mins. The excess amount of sample was removed before TEM acquisition. TEM images were acquired at 120 kV and analyzed by GATAN

digital imaging system (GATAN, Inc.). The amount of Fe in NPs was determined using inductively coupled plasma mass spectrometry (ICP-MS, PerkinElmer, NexION[®] 350X). For ICP-MS, the Fe-PLGA NPs samples were digested with 2.0 mL of concentrated HNO₃ for 3 h at 90 °C in a hot block digester (Environmental Express). After digestion, 100 µL of the sample was diluted with 10 mL of 2% HNO₃ and analyzed using ICP-MS. ICP standard of Fe³⁺ with 1, 2, 4, 8, 16, 32, 64, 128 ppb was used for the standard calibration curve.

The stability at physiological condition was investigated by dispersing nanoparticles in phosphate buffer saline (PBS, pH 7.4) at the particle concentration of 1 mg/mL. The nanoparticles were incubated at 37 °C for 4 weeks. The changes in hydrodynamic size and polydispersity index (PDI) were tracked each week using dynamic light scattering analysis. The serum stability of the prepared PLGA and Fe-PLGA NPs were carried out as reported in the literature. Briefly, 150 µL of 1 mg/mL nanoparticles were incubated with 50 µL of Fetal Bovine Serum (90%) at 37 °C. The change in absorbance at 560 nm was measured kinetically every 6s for 1 h, a double-orbital shaking with slow speed was applied before each measurement using a Microplate reader (BioTek, Synergy H1 hybrid reader).

Simulated body fluid (SBF) was prepared to mimic the biological environment by dissolving appropriate quantities of the chemical reagent in ultra-pure MiliQ water following the procedure reported by Ciineyt and Aryal et. al.^{266,267} The chemical reagents were added one after other as shown in Table 5.1 where each reagent was completely dissolved in 700 mL MiliQ water. The pH of the resulting SBF was adjusted by titrating with 1 M HCl to 7.4 at 37 °C, and the final volume was adjusted to 1 liter by adding the required amount of MiliQ water.

For the ascorbic acid oxidation assay, first, the UV-Vis spectrum of an ascorbic acid solution (67 µM and 12 µg/mL) in PBS was recorded in SpectraMax i3X (Molecular Devices).²⁶⁸ The

absorbance intensity at $\lambda_{\text{max}} = 265 \text{ nm}$ was observed. An aliquot ($30 \mu\text{L}$) of the iron chelate of ethylenediaminetetraacetic acid (Fe-EDTA) in PBS (2 mM , 0.7 mg/mL) was added to afford a catalytic quantity of Fe-EDTA ($20 \mu\text{M}$, $30 \text{ mol}\%$) for ascorbic acid. The absorbance intensity ($\lambda_{\text{max}} = 265 \text{ nm}$) was recorded at intervals of 1 minute for 60 minutes and the data normalized. The experiment was then repeated identically using a solution of the Fe-PLGA NPs under investigation ($20 \mu\text{M}$), and the results were plotted as a function of the percent initial ascorbic acid signal versus elapsed time (min).

Order	Reagent	Amount (g/L)	Sample
1	NaCl	6.547	A
2	NaHCO ₃	2.268	B
3	KCl	0.373	C
4	Na ₂ HPO ₄ .2H ₂ O	0.178	D
5	MgCl ₂ .2H ₂ O	0.305	E
6	CaCl ₂ .2H ₂ O	0.368	F
7	Na ₂ SO ₄	0.071	
8	(CH ₂ OH) ₃ CNH ₂	6.057	

Table 5.1 Composition of simulated body fluid in order of mixing reagents. Samples A–C are prepared under ambient conditions while samples D–F at $37 \text{ }^\circ\text{C}$ while stirring.

5.2.5 MRI phantom study of Fe-PLGA

The T_1 -weighted MRI images of Fe-PLGA NPs was investigated under low field (3.0 T , Canon, USA) and ultrahigh field (14.1 T , Bruker, MA) MRI system at $20 \text{ }^\circ\text{C}$. Samples of Fe-PLGA NPs were diluted in Mili-Q water with a series of concentrations of 0.02 , 0.03 , 0.07 , 0.13 , 0.27 , and 0.54 mM of Fe^{3+} . The r_1 of Fe-PLGA NPs was obtained using a fast spin-echo (FSE) sequence for 3 T and rapid acquisition with relaxation enhancement (RARE) pulse for 14.1 T with variable repetition time. A knee coil for 3 T with a local tube rack and a QTR 30 mm coil with a home designed falcon tube for holding 6 samples at a time in NMR tubes were used, respectively for phantom acquisition. Scans were performed with the following imaging parameters (3 T):

repetition time (TR)= 3000, 2500, 1500, 800, 500, and 200 ms, echo time (TE)= 7.5 ms, slice thickness= 2 mm, flip angle (FA)= 90° , image size 256×256 , FOV= 25.6×25.6 , total acquisition time of nearly 15 min and for 14 T: repetition time (TR)= 10000, 8000, 6000, 4000, 2500, 1500, 1000, 600, 400, 200, 100, 50 ms, echo time (TE)= 7.5 ms, slice thickness= 1 mm, flip angle (FA)= 80° , image size 256×256 , FOV= 30×30 , total acquisition time of 55 min 43 s. The representative T_1 weighted magnetic resonance phantom images of Fe-PLGA were taken at TR= 1500 ms, TE= 7.5 ms, and slice thickness= 2 mm. The longitudinal coefficient relaxivity value r_1 was determined from the slope of the plot of $1/T_1$ versus the sample concentration. Magnevist[®] was used as a control under the identical experimental condition for comparison.

5.2.6 *In vitro* biocompatibility study

In this study, the standard MTT assay was used to evaluate the cytotoxicity of Fe-PLGA NPs. For the MTT assay, MCF-7 cells were seeded with cell density 10,000 cells/well in 96-well plates and incubated overnight. After that, the cells were treated with different concentrations of pure PLGA NPs and Fe-PLGA NPs for 24 h. After washing, the cells were incubated with syringe filtered (0.22 μM) 100 μL of 5 mg/mL MTT in a $1 \times$ PBS solution. After 4 h of incubation, the supernatant was carefully aspirated and the intracellular formazan crystals were dissolved in DMSO. The absorbance of the formazan solution was measured by spectroscopy at 570 nm using DMSO as the blank. The cell viability (%) was expressed as the percentage relative to the control cells (untreated cells).

5.2.7 *In vitro* cellular uptake study

Cells were plated 20,000 cells per well on an 8-well chamber slide (BD Biosciences). After 24 h, cells were treated with RhB labeled PLGA and Fe-PLGA NPs with a final NP concentration of 50

$\mu\text{g/mL}$ and incubated over varying periods (0, 0.5, 1.5, and 3 h). After incubation, the treated cells were washed twice with $1\times$ PBS (pH 7.4), fixed with 4% paraformaldehyde for 15 min at room temperature, stained with DAPI for an additional 10 min, mounted with Fluoromount aqueous medium (Sigma-Aldrich), and imaged using CLSM (Carl Zeiss, LSM-700). The cellular uptake was assessed by measuring RhB fluorescence intensity using Image-J software (National Institute of Health). The data were analyzed using one-way ANOVA with Turkey's multiple comparison post-test.

5.2.8 *In vivo* MRI study

In vivo MRI study was performed using NU/NU mice on a 3 T MRI clinical scanner. In brief, the mice have intravenously injected 100 μL of Fe-PLGA NPs (equivalent Fe concentration of 0.2 mmol/kg) with formulation reconstituted in saline *via* the lateral tail vein. During imaging, mice were continuously anesthetized with 2 to 4% isoflurane in oxygen delivered using a nose cone mounted on the mouse holder. Whole-body coronal slices images were acquired immediately pre-injection, at injection (bolus injection), and post-injections at 10 min, 1 h, 2 h, and 3 h. The T_1 -weighted MR images were recorded using FSE sequences discussed above. The recorded images with different slices were processed for maximum intensity projection. All images were analyzed using Medical Image Processing, Analysis, and Visualization (MIPAV) software. The animal experiment and protocols were approved by the Institutional Animal Care and Use Committee and Institutional Biosafety Committee, Kansas State University, Manhattan.

5.3 Result and Discussion

5.3.1 Limitations of currently used CAs in medical imaging

The objective of the CA is to visualize blood vessels, tissue abnormalities, and their architecture in different organs of the body, with a particular interest in arteries, veins, heart chambers,

inflammation, and tumors. The gold standard in diagnostic imaging, especially arterial occlusive disease, is conventional x-ray angiography. This is an invasive, costly, and potentially hazardous procedure that is performed *via* computed tomography and by systemically injecting high doses of an iodinated CAs.^{269–271} Therefore, alternative noninvasive MRI approaches have been introduced, which allow us to visualize vessel stenosis, occlusions, aneurysms, and other less common vascular abnormalities, tumors, as well as the properties of the vessel walls. MRI minimizes artifacts that are generally associated with the complex temporal and spatial flow patterns within the blood vessels and the respiratory motion. Iron oxide (Ferumoxides or Feridex: colloid of SPIONPs associated with dextran) was used for Ce-MRI in the United States over a decade but is no longer used due to its associated side effects and poor clinical benefit. Safety concerns about GBCAs were raised for patients with normal kidney function in 2014 when researchers discovered that Gd could remain in patient's brains and could accumulate with each dose of contrast that they received.^{272–274} Long-term accumulation of gadolinium causes gadolinium-associated plaques that share certain symptoms in patients with normal kidney function.²⁷⁵ This has resulted in guidelines recommending more careful consideration of the benefits and the risks of various GBCAs for each patient and situation.²⁷⁴ Therefore, we must look for a better alternative that is endogenous and have known biological safe clearance from the body. The overall goal of this project is to explore the use of Fe³⁺ as an alternative, Gd free, T₁ CA.

5.3.2 Morphology, size, and charge distribution of Fe-PLGA NPs

The chelation of Fe³⁺ cations in the PLGA NPs was performed by nanoprecipitation as discussed in the method and material section. The physical morphology of the Fe-PLGA nanoparticles measured using TEM that showed highly monodispersed and uniform spherical shaped particles with an average diameter of 93 ± 7 nm (**Figure 5.1 A**). The presence of Fe³⁺ metal ions localized inside the

spherical nanoparticles was confirmed with energy-dispersive X-ray spectroscopy (EDS). Specifically, the EDS profiles suggested that the content of Fe in the testing areas of Fe-PLGA significantly higher than those on the grid surface background, which are in good agreement with the elemental mapping analysis results (**Figure 5.1 B**). Furthermore, the average hydrodynamic size of the Fe-PLGA NP was 130 ± 12 nm with a PDI of 0.231 ± 0.026 (**Figure 5.1 C**). The Fe-PLGA NPs when dispersed into $1 \times$ PBS showed zeta potential of -6 ± 2 mV as compared to the PLGA NPs (before chelation) of -39 ± 6 mV (**Figure 5.1 D**). The negative zeta potential is likely due to the surface carboxylate groups at the end moiety of the PEG corona and the presence of soluble anions in the PBS solution. The large increase of surface charge can also be corroborated with the chelation with Fe^{3+} cations thereby decreasing the overall surface charge of the nanoparticles. The difference between TEM and hydrodynamic sizes indicates that the DSPE-PEG provided a hydrating layer over the surface of the nanoparticle. Thus, formed hydrating layers could enhance nanoparticle stability helping to minimize protein corona formation in the bloodstream, and prevent the nanoconstruct from immune invasion. We did not observe agglomeration with no significant changes in size and PDI of nanoparticles (**Figure 5.2 A**) incubated over the four weeks in the physiological condition of PBS at pH= 7.4. Furthermore, we evaluated the serum stability of pure PLGA NPs and Fe-PLGA NPs using 90% FBS where we observed immediate aggregation of PLGA NPs as indicated by the increase in absorbance at 560 nm while Fe-PLGA NPs were stable under serum condition (**Figure 5.2 B**). This *in vitro* study verified long-term stability in PBS and serum showing the applicability of the nanoparticles for the biological environment.

5.3.3 Ferric chloride loading and release study

The Fe^{3+} encapsulation efficiency of the NPs was evaluated by altering the initial iron input concentration from 5 to 198 μM per mg of the PLGA. The results showed that the initial Fe^{3+} loading

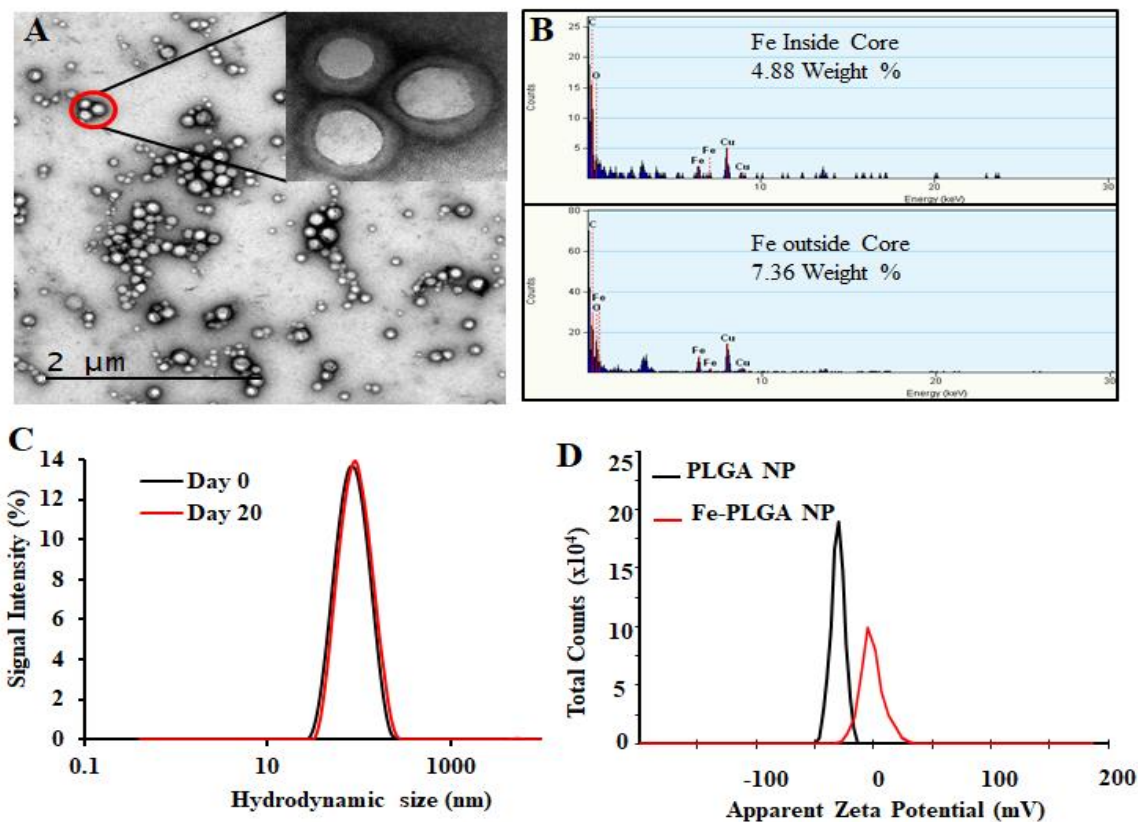


Figure 5.1 Physicochemical characterization of iron (III) chelated polymeric NPs. A) Transmission Emission Micrograph (TEM) of NPs, B) The hydrodynamic size of NPs as prepared and after 20-day incubation of Fe-PLGA NPs, and D) Zeta potential of PLGA NPs and Fe-PLGA NPs dispersed in PBS.

can be precisely tuned by varying the iron input (5, 10, 25, 50, 74, 99, and 198 $\mu\text{M}/\text{mg}$ of PLGA weight) during the NP preparation process (**Figure 5.2 C**). Among the different initial Fe^{3+} feeding concentrations, the maximum encapsulation efficiency was found to be about 14% (w/w) iron per 1 mg polymer in which a plateau was observed with 50 μM . When the initial input amount of iron increases up to 200 μM per 1 mg PLGA, the nanoparticle started to aggregate due to the destabilization affecting the physiological stability of the particles as indicated by rapid aggregation and precipitation due to the excess amount of iron in the suspension. Therefore, after investigating various loading of iron input, we found 200 μL (0.1 M FeCl_3) input formulation corresponding to 99 μM iron per 1 mg PLGA is an ideal composition for further investigations. No significant changes in the size and PDI of this formulation were observed when stored at 4 $^\circ\text{C}$

in PBS (pH = 7.4) over 4 weeks, confirming the excellent physicochemical properties (**Figure 5.2 A**). When Fe-PLGA-200 is 1.0 mg/mL, the concentration of iron is found to be 214 $\mu\text{g/mL}$ according to ICP-MS.

The retention of Fe^{3+} ions in the nanoparticle formulation is paramount for the development of a safer contrast agent. To evaluate the chelation stability of iron in the Fe-PLGA NPs formulation, the competitive iron release assay was carried out in simulated body fluid with different ion media prepared according to the literature.^{266,267} Magnevist[®], a widely used commercial Gd-based contrast agent, was used as a control. As we expected that the Fe-PLGA NPs nanoconstruct could serve as a T_1 -weighted next-generation CA, the phenomenon such as transmetalation with endogenous scavenger cations while traveling in the bloodstream could be minimized to achieve a better safety profile. Therefore, the Fe-PLGA NPs were challenged with different ion media in simulated body fluid, exactly mimicking the blood serum condition. The iron release characteristics of Fe-PLGA NPs were mapped in terms of cumulative iron release from a 500 Da dialysis bag and compared with the Magnevist[®]. This selected molecular weight cutoff gives free passage of all ion presence in the media. As a result, in simulated body fluid (pH 7.4), Fe-PLGA NPs appeared to be highly stable with about 2% release up to 24 h, 2.4% at 48 h, and 3.1% of iron release over 72 h of incubation (**Figure 5. 2 D**). This minimal release could be attributed to the strong chelation of Fe^{3+} ions with carboxylate end of PLGA and lipid-PEG. On the other hand, the amount of Gd released from Magnevist[®] (a clinical contrast agent) under the identical condition increases significantly as the incubation time increase leading to the cumulative release of 12.3% at 72 h of incubation. Additionally, Gd is a toxic heavy metal with safety concerns regarding the use of GBCAs for Ce-MRI. When dechelated, the free Gd^{3+} ions due to similar ionic sizes can compete with Ca^{2+} ions affecting voltage-gated calcium channels and disrupting crucial

calcium homeostasis causing adverse biological effects.¹⁷⁶ Because of these concerns, when challenged with simulated body fluid, the designed iron-based T₁-weighted next-generation of nanoscale CAs provided more than 96% retention of iron within the nanoconstruct as compared to the 85% retention of Gd from Magnevist[®]. These preliminary results demonstrate the potential alternative, Gd free, T₁-weighted MR contrast agent.

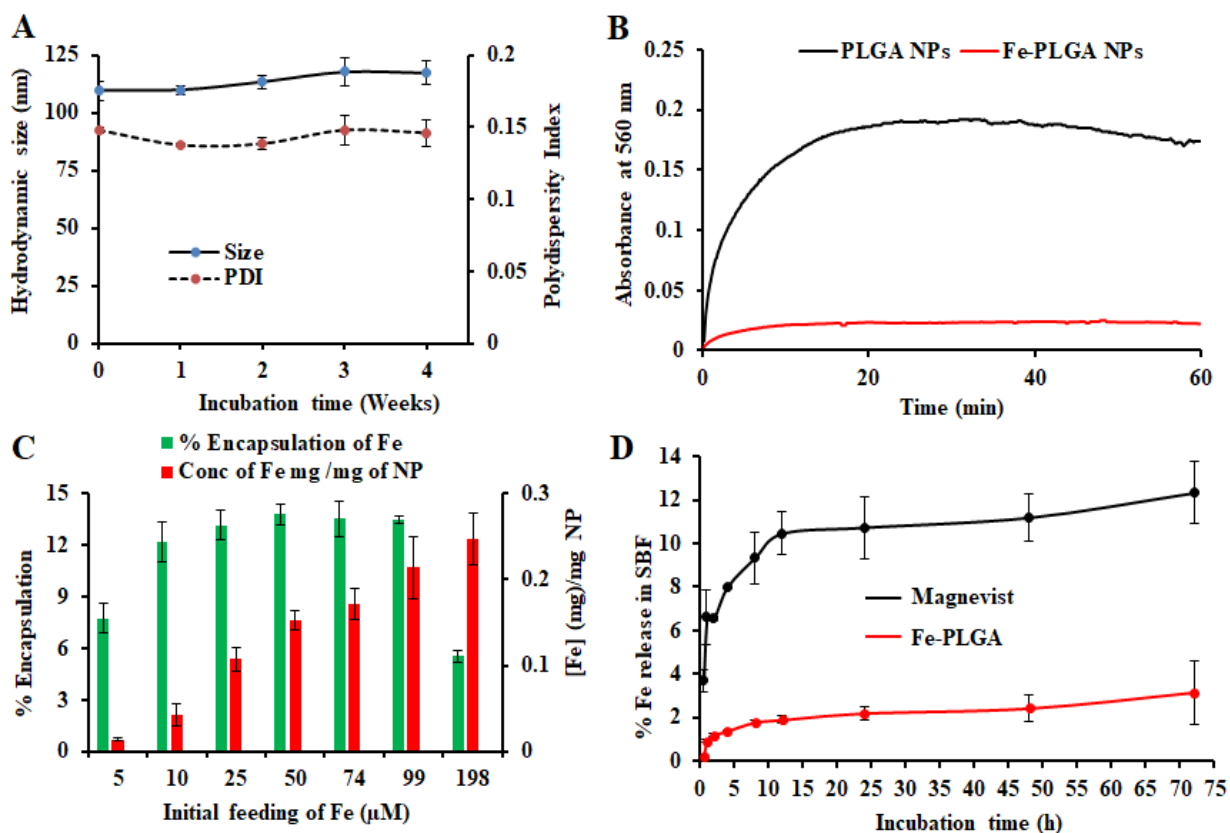


Figure 5.2 Stability and loading/release study of iron (III) chelated polymeric NPs. A) Stability of NPs over 4 weeks period when stored at 4 °C showing the change of size and polydispersity index, B) Serum stability test to measure dynamic aggregation of PLGA NPs and Fe-PLGA NPs using 90% fetal bovine serum environment to find the rapid increase in optical density of 560 nm due to NPs aggregation by forming protein corona, C) Iron loading efficiency with different initial feeding concentration of Fe³⁺ per mg PLGA, and D) A comparative Fe release study from Fe-PLGA NPs and Gd from Magnevist[®] against simulated body fluid (SBF). Data represents mean ± S.D, n= 3.

While the Fe-PLGA NPs are well stable in aqueous media, one concern related to iron-mediated oxidative Fenton chemistry to produce hydroxyl radicals, which are deleterious to

biomolecules. However, when the iron is strongly stabilized by chelates, herein carboxylate in polymeric NPs and polymer matrix created diffusion barrier, are known that do not appreciably catalyze Fenton chemistry and, therefore, minimize an important route by which iron can be toxic.^{276,277} Therefore, this possibility was studied using ascorbic acid, as a model biomolecule, oxidation catalyzed by Fe³⁺. As shown in **Figure 5.3**, over the period of incubation, FeCl₃ catalyzed the reaction (decrease in absorbance at 265 nm) but Fe-PLGA NPs did not catalyze the oxidation of ascorbic acid supporting the stability of Fe³⁺ ion, NPs colloidal stability, and biocompatibility with no noticeable generation of radical ions.

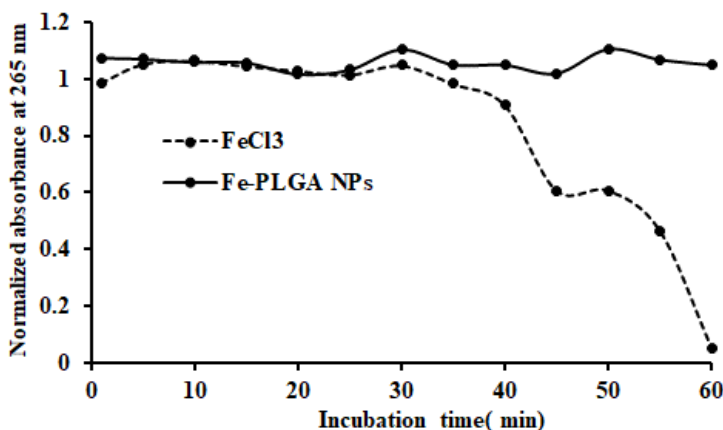


Figure 5.3 Oxidation of ascorbic acid catalyzed by Fe³⁺. FeCl₃ catalyzed the oxidation reaction of ascorbic acid as shown by the decrease in absorbance at 265 nm whereas, Fe-PLGA NPs did not catalyze the reaction.

5.3.4 *In vitro* cellular interaction study

Next, the biocompatibility of Fe-PLGA NPs was evaluated in MCF-7 cells using the standard MTT assay. Similar to Fe³⁺-chelated melanin colloidal nanoparticles and many other kinds of polycatechol-based biomaterials^{250–252,261,278–280}, Fe-PLGA NPs also showed higher biocompatibility and promisingly low toxicity in cells. **Figure 5.4 A** illustrates the biocompatibility in MCF-7 cells cultivated for 24 h with various concentrations of Fe-PLGA NPs from 5 to 200 µg/mL with the data as an average of three repeating tests. The higher cell viability over 85% against the highest concentration of nanoparticles used (200 µg/mL) indicates excellent

biocompatibility and low toxicity. After confirming the biocompatibility of nanoparticles, we assessed the time-dependent cellular uptake of rhodamine-labeled Fe-PLGA NPs (50 $\mu\text{g}/\text{mL}$) for 0.5, 1.5, and 3 h, respectively in cells using confocal microscopy. **Figure 5.4 B** shows the representative confocal images of the cells showing the internalization of NPs and their corresponding quantification of rhodamine intensity of internalized NPs using ImageJ. Untreated cells were used as control. **Figure 5.4 C** shows the fluorescence intensity of the Fe-PLGA was significantly higher at 3 h when compared with 0.5 h incubation ($p\text{-value} < 0.0001$, one-way ANOVA with Mann Whitney test). It is expected that with the increase of treatment time, the NPs uptake also increased for initial time points, as in the case of 0.5 h versus 1.5 h also showed a significant increase ($p\text{-value} < 0.02$). This observation clearly demonstrates that Fe-PLGA NPs were taken up by cells. These results corroborate with the previous findings of metal encapsulated polymeric nanoparticles.^{40,165,206,264,281,282} The observed high cellular viability and excellent retention of Fe^{3+} in Fe-PLGA NPs, taken together, confirm the stability of Fe^{3+} in the nanoconstruct showing excellent compatibility of the formulated Fe-PLGA NPs as a safe contrast agent.

5.3.5 Assessment of magnetic properties *in vitro*

With the assurance of stability and safety of Fe-PLGA NPs, the MRI contrast efficiency of the nanoconstruct was evaluated by looking into the effect of paramagnetic Fe^{3+} on the magnetic relaxivity for possible applications in MRI. Fe-PLGA NPs were characterized for magnetic properties by measuring T_1 as a function of aqueous nanoparticles with different Fe^{3+} concentrations. The T_1 weighted image of Fe-PLGA NPs at different millimolar concentrations was obtained using clinical (3 T) and ultra-high-field (14.1 T) MRI as shown in **Figure 5.5**. The T_1 -weighted image showed a

concentration-dependent higher signal intensity at higher concentration supported by the T_1 recovery curves at a particular concentration of iron as a function of recovery time (**Figures 5.5 A and B**). With

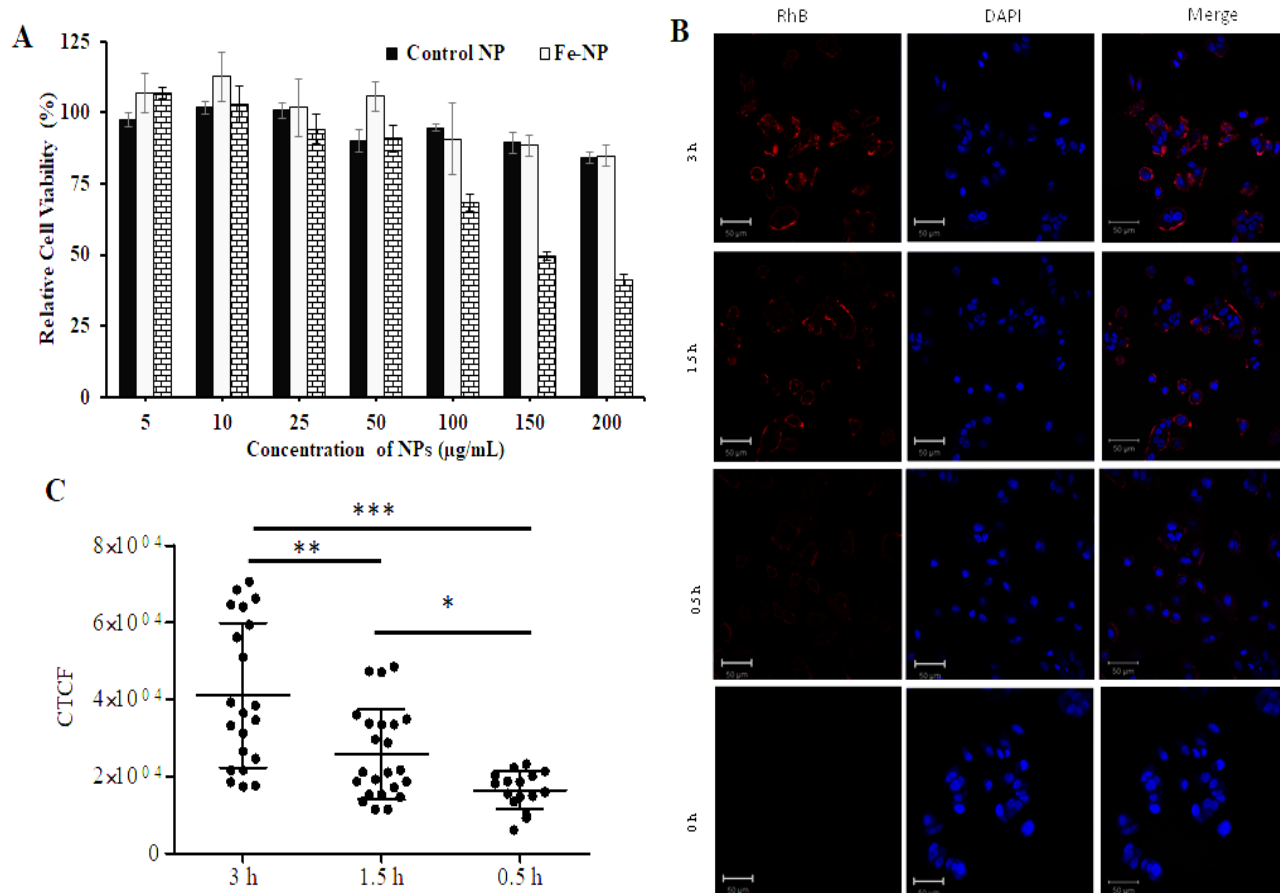


Figure 5.4 *In vitro* biocompatibility studies and cellular uptake study. (A) Concentration-dependent cytotoxicity of NPs in MCF-7 cells with 48 h incubation, (B) Representative confocal images showing comparative cellular uptake of NPs after 0.5, 1.5, and 3 h incubations and (C) Fluorescent quantification of cellular uptake by measuring corrected total cell fluorescent intensity of the cell population for each treatment and group. The data were statistically analyzed using one-way ANOVA with the Mann Whitney test. (n = ~50 cells, mean ± sd). ns = not significant, **p*-value < 0.02, ** *p*-value < 0.0045, *** *p*-value < 0.0001).

the increase of iron concentration, the MR signal was significantly enhanced as shown in the aqueous phantom images (**Figure 5.5 C**), suggesting Fe-PLGA NPs generate a high magnetic field gradient on their surface. These nanoparticles showed a higher % signal intensity at 3 T compared to 14.1 T at all recovery time points signifying enhanced contrast properties. The longitudinal relaxivity (r_1) as calculated from the slope of the linear fit of the inverse of recovery time (s^{-1}) with respect to different

iron concentrations (mM) shows a significant higher r_1 , the slope of the fitted curve in **Figure 5.5 D**, is measured to be $10.59 \pm 0.32 \text{ mM}^{-1} \cdot \text{s}^{-1}$ and $3.02 \pm 0.14 \text{ mM}^{-1} \cdot \text{s}^{-1}$ in 3.0 T and 14.1 T magnetic fields,

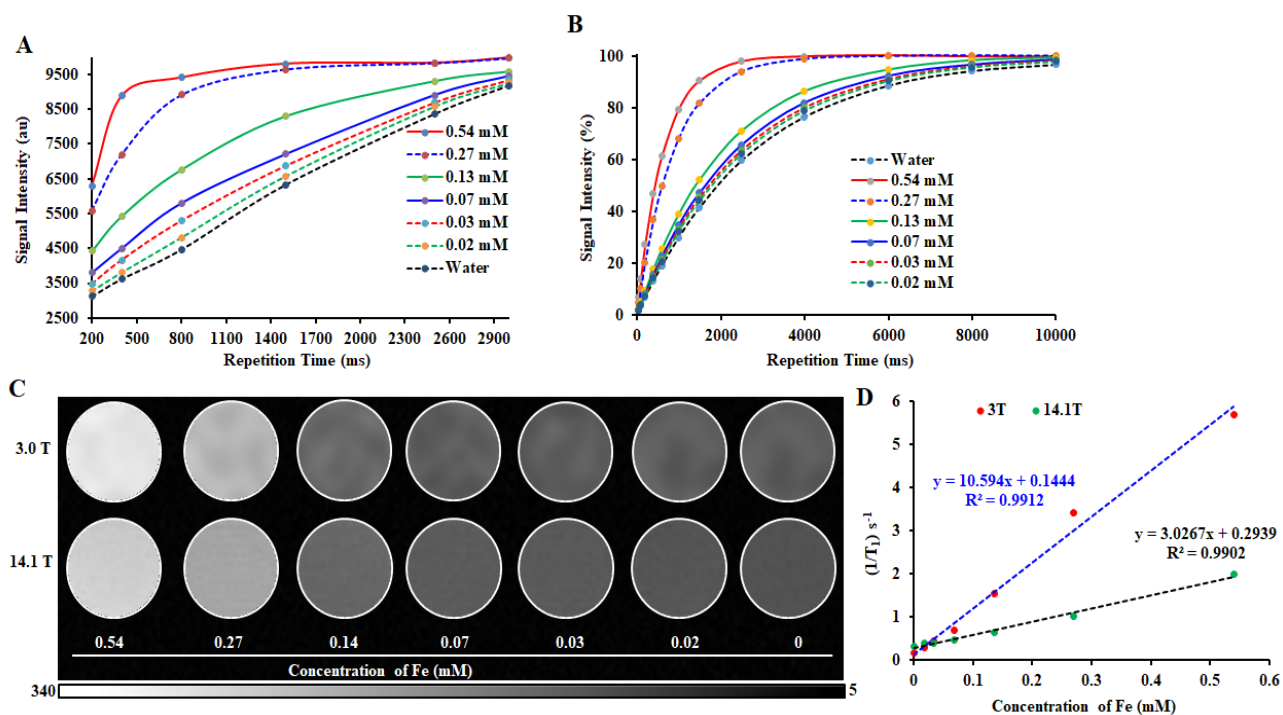


Figure 5.5 Relaxivity study of iron (III) chelated polymeric NPs in the low and ultra-high magnetic fields. A-B) T_1 recovery curve of NPs at low field (3 T) and ultra-high-field (14.1 T) as a function of iron concentration, C) T_1 -weighted MR phantom images of iron (III) chelated PLGA NPs aqueous suspensions with different concentrations corresponding to recovery curves A and B, and D) T_1 longitudinal relaxation rate against Fe^{3+} concentration measured at 3 T and 14.1 T MRI system at room temperature. Data represents mean \pm S.D, $n=3$.

respectively at 25 °C and pH 7.4. It is worth mentioning that such an r_1 value reaches obvious higher enhancement than the commercial agents Dotarem[®] ($3.8 \text{ mM}^{-1} \cdot \text{s}^{-1}$) and Magnevist[®] ($3.1 \text{ mM}^{-1} \cdot \text{s}^{-1}$), macrocyclic and linear clinical GBCAs, respectively in 3 T. The observed significant contrast enhancement in the case of Fe-PLGA NPs formulation can be attributed to the reduction of the tumbling rate of paramagnetic metal complexes due to incorporation in a stable nanoparticulate formulation, thereby promoting effective interaction between a water molecule and paramagnetic metal complex. The field-dependent relaxivity of CAs, especially GBCAs, has been widely recognized. As such, the low r_1 relaxivity of Fe-PLGA NPs at the ultra-high-field is suggestive of the

magnetic field effect affecting the rotational correlation time.^{283,284} This effect is well illustrated in the case of MS-325 (Gadofosveset[®]) where the $r_1 = 8.30 \text{ mM}^{-1} \cdot \text{s}^{-1}$ and $r_1 = 5.14 \text{ mM}^{-1} \cdot \text{s}^{-1}$ at 1.4 and 9.4 T, respectively.²⁸³ A similar increment in longitudinal relaxivity was reported by Liang et al., where naïve Dotarem[®] showed r_1 relaxivity of $4.2 \text{ mM}^{-1} \cdot \text{s}^{-1}$ compared to $10.61 \text{ mM}^{-1} \cdot \text{s}^{-1}$ at 3 T when incorporated into a polymeric nanoparticle system.²⁸⁵ Likewise, Aryal et al. also reported an increment of r_1 relaxivity of Dotarem[®] to $19 \text{ mM}^{-1} \cdot \text{s}^{-1}$ at 3 T after insertion in the lipid bilayer of the red blood cell membrane fused liposomal system.²⁸⁶

5.3.6 *In vivo* vascular imaging

With the validation of contrast enhancement and safety *in vitro*, the potential of Fe-PLGA NPs as Gd free T_1 -weighted CAs for *in vivo* Ce-MRI was evaluated in the murine model. A dose of 0.2 mmol/kg equivalent Fe concentration of Fe-PLGA NPs in 100 μL with formulation reconstituted in saline was intravenously injected *via* the lateral tail vein. Dynamic MR images were acquired pre-contrast and at-injection, 10 min, 1 h, 2 h, and 3 h post-injection under a 3 T clinical scanner. **Figure 5.5** shows the 3D reconstruction of images acquired at-injection showing maximum intensity projection with the clear enhancement of contrast at vascular lumen, especially in the abdominal aorta, when compared with the pre-contrast reconstructed image as presented in **Figure 5.5 and Appendix C- Figure 5.S1**). After post-injection, the MR signal at the blood vessel and surrounding tissue with the longer contrast enhancement observed at the abdominal region but we did not observe any noticeable changes in the bladder even after 3 h post-injection. In our recent study using red blood cell membrane wrapped Gd encapsulated polymeric nanoparticles, we found that Magnevist[®] quickly extravasate into the surrounding tissue and showed enhanced MR signal at the kidney but the membrane wrapped nanoparticles exhibited the significantly higher contrast in heart and blood vessels with half the dose of Gd used than that of Magnevist[®]. The shorter

plasma retention time of Magnevist[®] is well described and documented in the literature.^{230,32,245,36,278,282,37} Similar to our observation of Fe-PLGA NPs, in a study conducted by Young et al has demonstrated in small clinical patients that oral dose (0.06%) of ferric chloride has significantly reduced the T₁ relaxation times from 730 ms to 285 ms in the fundus of the stomach showing the promise as the bowel-labeling agent for Ce-MRI.²³²

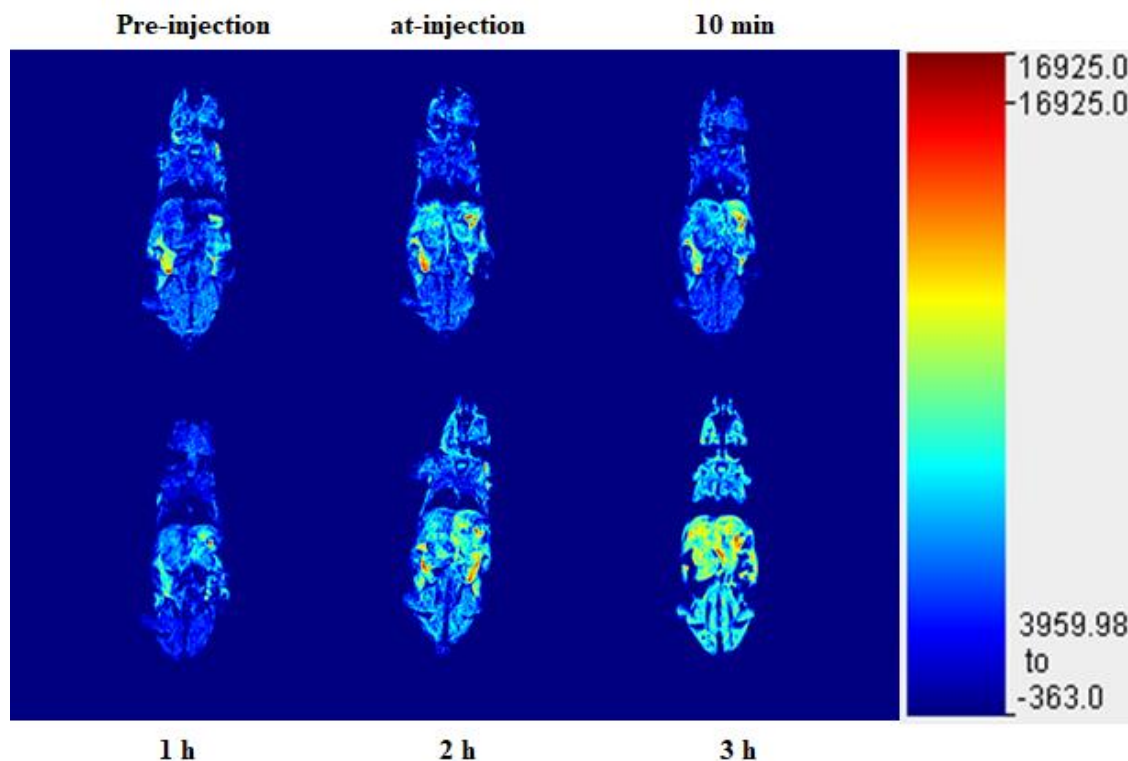


Figure 5.6 *In vivo* time-dependent T₁ weighted magnetic resonance image of mice at 3 T. Upper panel represents the 3D reconstruction of images acquired at injection using maximum intensity projection with pre-injection (left), at-injection (middle), and post-injection after 10 min (right) while lower panel represents 3D reconstruction images at 1, 2, and 3 h from left to right respectively. The mice were intravenously injected with Fe-PLGA NPs (equivalent Fe concentration of 0.02 mmol/kg).

Considering the abundant amount of Fe³⁺ ions in the living body and clearly known metabolic pathways, Fe-PLGA nanoparticulate system is expected to be metabolized in living subjects. The significantly higher T₁ effect of our designed formulation compared to small molecular GBCAs and potential toxicity of Gd, our system could offer an alternative platform for next-generation of

iron-based nanoscale T₁-weighted contrast agents for Ce-MRI. On the other hand, the traditional nanoparticulate system, for example, mesoporous silica, SPIONPs, gold nanoparticle, needs complicated multistep functionalization of ligand to chelate Gd³⁺ for MRI exams. Additionally, the new Fe-PLGA NPs system can serve the one-pot fabrication method that significantly simplifies the preparation process and reduces the heterogeneity of the resulting NPs. In addition, the PLGA is an organic and biodegradable FDA approved material for biomedical application and our system showed relatively good *in vivo* imaging properties. All of these properties make Fe-PLGA NPs highly promising for potential clinical translation.

5.4 Conclusion

In conclusion, a biocompatible one-pot Fe³⁺-based CA nanoplatform was designed to provide an excellent T₁ contrast enhancement at the clinically relevant 3 T magnetic field. The nanoconstruct facilitated the relaxivity enhancement *in vivo* and provided stability in a biologically identical condition. Considering the outstanding MRI performance, ease of synthesis, long-term stability, and biocompatibility, the use of Fe-PLGA NPs allows *in vivo* imaging thereby providing a safer and an alternative, a Gd free, platform for Ce-MRI. Also, the facile chemistry of PLGA polymer could offer new opportunities for additional targeting ligand functionalization and drug loading; Fe-PLGA NPs has potential applications as multifunctional agents for both disease diagnosis and treatment in a single session. All of these properties make Fe-PLGA NPs highly promising for potential clinical translation.

Chapter 6 - Summary and Outlook

Nanotechnology is the control of matter at the nanoscale, where unique phenomena and unusual properties enable novel applications by combining different functionalities in a single platform for example in medicine, disease targeting, diagnosis, and therapy. In this dissertation, two different approaches *via* light and magnet as external stimuli-responsive design strategies have been put forth in nanoscale with an ability to deliver drug and/or contrast agents to cancer. Thus designed nanomaterials were extensively characterized and evaluated for their physicochemical and biological functions.

Under the photoresponsive nanomaterials, drug delivery systems which are made up of rod-shaped gold nanoparticles decorated peripherally by PEG sheath was developed (**Chapter 2**). The engineered nanoconstruct exhibited combinatorial actions, upon illumination with NIR light, including targeting and therapy of skin cancer. As a one step forward, the NIR light-sensitive small-molecule fluorescent probe called IR-820 dye loaded into the core of PLGA nanoparticle was designed for both photothermal and optical imaging to enhance the effectiveness of non-invasive cancer diagnosis and therapy in a single session (**Chapter 3**). This project was further extended to see how the presence of targeting ligand changes the targeting and biodistribution patterns using LyP-1 peptide on the surface of nanocarrier using conjugation chemistry while drug as DOX or NIR imaging probe as DiR dye were engineered as core materials. This tumor-targeting strategy was able to deliver the payload about three times higher than that of the non-targeted counterparts by receptor-mediated interactions in the tumor-bearing mice model (**Chapter 4**). On the other hand, a paramagnetic iron chelated polymeric nanoconstruct was fabricated to enhance bright contrast as a next generation of MRI CAs to substitute potentially toxic clinically used GBCAs for disease diagnosis (**Chapter 5**). This study has resulted in an optimized iron chelated

polymeric nanoconstruct with enhanced contrast efficacy for improved MR imaging of disease pathology.

The major advantage of the nanocarriers presented in this dissertation are their abilities to stealth (**Chapter 2 to 4**) and communicate friendly with endogenous ions (**Chapter 5**). While promising data were obtained indicating the opportunities for these nanoformulations, challenges to translate from the bench-to-bedside still require further investigations including potential immunogenicity, organ-specific toxicity, pharmacokinetics, and *in vivo* therapeutic effectiveness, which are out of the scope of this dissertation. Thoughtful relationship between biology and technology including understanding the influence of disease pathophysiology on nanomaterial accumulation, distribution, retention, and efficacy, as well as the biopharmaceutical correlation between delivery system properties and *in vivo* behavior in mice versus humans are important determinants for the successful translation of nanoformulations. Thus, the application of a disease-driven approach for nanomaterial design strategies that can exploit pathophysiological changes in disease biology could improve the clinical translation of nanomedicine.

References

- (1) Nanotechnology Timeline | Nano <https://www.nano.gov/timeline> (accessed Jan 7, 2020).
- (2) Daw, R. Nanotechnology Is Ancient History. *The Guardian*. April 24, 2012.
- (3) The Nanotechnology Revolution <https://www.thenewatlantis.com/publications/the-nanotechnology-revolution> (accessed Feb 4, 2020).
- (4) This 1,600-Year-Old Goblet Shows that the Romans Were Nanotechnology Pioneers <https://www.smithsonianmag.com/history/this-1600-year-old-goblet-shows-that-the-romans-were-nanotechnology-pioneers-787224/> (accessed Feb 4, 2020).
- (5) Technology: NANOTECHNOLOGY In Ancient India <https://callcenterinfo.tmcnet.com/news/2006/11/17/2089553.htm> (accessed Feb 5, 2020).
- (6) Reibold, M.; Paufler, P.; Levin, A. A.; Kochmann, W.; Pätzke, N.; Meyer, D. C. Carbon Nanotubes in an Ancient Damascus Sabre. *Nature* **2006**, *444* (7117), 286–286. <https://doi.org/10.1038/444286a>.
- (7) Daw, R. Nanotechnology Is Ancient History. *The Guardian*. April 24, 2012.
- (8) Molecules | Free Full-Text | The History of Nanoscience and Nanotechnology: From Chemical–Physical Applications to Nanomedicine <https://www.mdpi.com/1420-3049/25/1/112> (accessed Feb 5, 2020).
- (9) Hulla, J.; Sahu, S.; Hayes, A. Nanotechnology: History and Future. *Hum. Exp. Toxicol.* **2015**, *34* (12), 1318–1321. <https://doi.org/10.1177/0960327115603588>.
- (10) Reibold, M.; Paufler, P.; Levin, A. A.; Kochmann, W.; Pätzke, N.; Meyer, D. C. Carbon Nanotubes in an Ancient Damascus Sabre. *Nature* **2006**, *444* (7117), 286–286. <https://doi.org/10.1038/444286a>.
- (11) Marasini, R.; Joshi, S. Antibacterial and Antifungal Activity of Medicinal Orchids Growing in Nepal. *J. Nepal Chem. Soc.* **2012**, *29*, 104–109. <https://doi.org/10.3126/jncs.v29i0.9259>.
- (12) Baboo, R. Ancient Indian Culture and Nanotechnology. **2015**, *2* (3), 3.
- (13) Nanomedicine | medicine <https://www.britannica.com/science/nanomedicine> (accessed Jan 7, 2020).
- (14) Thompson, D. Michael Faraday’s Recognition of Ruby Gold: The Birth of Modern Nanotechnology. *Gold Bull.* **2007**, *40* (4), 267–269. <https://doi.org/10.1007/BF03215598>.
- (15) Feynman, R. P. There’s Plenty of Room at the Bottom. *Eng. Sci.* **1960**, *23* (5), 22–36.
- (16) Soares, S.; Sousa, J.; Pais, A.; Vitorino, C. Nanomedicine: Principles, Properties, and Regulatory Issues. *Front. Chem.* **2018**, *6*. <https://doi.org/10.3389/fchem.2018.00360>.
- (17) van der Meel, R.; Sulheim, E.; Shi, Y.; Kiessling, F.; Mulder, W. J. M.; Lammers, T. Smart Cancer Nanomedicine. *Nat. Nanotechnol.* **2019**, *14* (11), 1007–1017. <https://doi.org/10.1038/s41565-019-0567-y>.
- (18) Cervadoro, A.; Cho, M.; Key, J.; Cooper, C.; Stigliano, C.; Aryal, S.; Brazdeikis, A.; Leary, J. F.; Decuzzi, P. Synthesis of Multifunctional Magnetic NanoFlakes for Magnetic Resonance Imaging, Hyperthermia, and Targeting. *ACS Appl. Mater. Interfaces* **2014**, *6* (15), 12939–12946. <https://doi.org/10.1021/am504270c>.
- (19) Lee, Y.-H.; Bhattarai, G.; Aryal, S.; Lee, N.-H.; Lee, M.-H.; Kim, T.-G.; Jhee, E.-C.; Kim, H.-Y.; Yi, H.-K. Modified Titanium Surface with Gelatin Nano Gold Composite Increases Osteoblast Cell Biocompatibility. *Appl. Surf. Sci.* **2010**, *256* (20), 5882–5887. <https://doi.org/10.1016/j.apsusc.2010.03.069>.

- (20) Aryal, S.; Pilla, S.; Gong, S. Multifunctional Nano-Micelles Formed by Amphiphilic Gold-Polycaprolactone-Methoxy Poly(Ethylene Glycol) (Au-PCL-MPEG) Nanoparticles for Potential Drug Delivery Applications. *J. Nanosci. Nanotechnol.* **2009**, *9* (10), 5701–5708. <https://doi.org/10.1166/jnn.2009.1227>.
- (21) Rayamajhi, S.; Nguyen, T.; Eliyapura, A.; Marasini, R.; Aryal, S. Engineering Immune Cell-Derived Hybrid Exosomes for Tumor-Targeted Drug Delivery; American Chemical Society, 2018; Vol. 256.
- (22) Page Faulk, W.; Malcolm Taylor, G. Communication to the Editors: An Immunocolloid Method for the Electron Microscope. *Immunochemistry* **1971**, *8* (11), 1081–1083. [https://doi.org/10.1016/0019-2791\(71\)90496-4](https://doi.org/10.1016/0019-2791(71)90496-4).
- (23) Gabizon, A.; Catane, R.; Uziely, B.; Kaufman, B.; Safra, T.; Cohen, R.; Martin, F.; Huang, A.; Barenholz, Y. Prolonged Circulation Time and Enhanced Accumulation in Malignant Exudates of Doxorubicin Encapsulated in Polyethylene-Glycol Coated Liposomes. *Cancer Res.* **1994**, *54* (4), 987–992.
- (24) Ventola, C. L. Progress in Nanomedicine: Approved and Investigational Nanodrugs. *P T Peer-Rev. J. Formul. Manag.* **2017**, *42* (12), 742–755.
- (25) Dilnawaz, F.; Acharya, S.; Sahoo, S. K. Recent Trends of Nanomedicinal Approaches in Clinics. *Int. J. Pharm.* **2018**, *538* (1), 263–278. <https://doi.org/10.1016/j.ijpharm.2018.01.016>.
- (26) Anselmo, A. C.; Mitragotri, S. Nanoparticles in the Clinic: An Update. *Bioeng. Transl. Med.* **2019**, *4* (3), e10143. <https://doi.org/10.1002/btm2.10143>.
- (27) Smith-Bindman, R.; Miglioretti, D. L.; Larson, E. B. Rising Use Of Diagnostic Medical Imaging In A Large Integrated Health System. *Health Aff. (Millwood)* **2008**, *27* (6), 1491–1502. <https://doi.org/10.1377/hlthaff.27.6.1491>.
- (28) Xie, D.; Yu, M.; Kadakia, R. T.; Que, E. L. 19F Magnetic Resonance Activity-Based Sensing Using Paramagnetic Metals. *Acc. Chem. Res.* **2020**, *53* (1), 2–10. <https://doi.org/10.1021/acs.accounts.9b00352>.
- (29) Bulte, J. W. M. In Vivo MRI Cell Tracking: Clinical Studies. *Am. J. Roentgenol.* **2009**, *193* (2), 314–325. <https://doi.org/10.2214/AJR.09.3107>.
- (30) Nejadnik, H.; Jung, K. O.; Theruvath, A. J.; Kiru, L.; Liu, A.; Wu, W.; Sulchek, T.; Pratz, G.; Daldrup-Link, H. E. Instant Labeling of Therapeutic Cells for Multimodality Imaging. *Theranostics* **2020**, *10* (13), 6024–6034. <https://doi.org/10.7150/thno.39554>.
- (31) Mukherjee, S.; Sonanini, D.; Maurer, A.; Daldrup-Link, H. E. The Yin and Yang of Imaging Tumor Associated Macrophages with PET and MRI. *Theranostics* **2019**, *9* (25), 7730–7748. <https://doi.org/10.7150/thno.37306>.
- (32) Rayamajhi, S.; Marasini, R.; Thanh Nguyen, T. D.; L. Plattner, B.; Biller, D.; Aryal, S. Strategic Reconstruction of Macrophage-Derived Extracellular Vesicles as a Magnetic Resonance Imaging Contrast Agent. *Biomater. Sci.* **2020**, *8* (10), 2887–2904. <https://doi.org/10.1039/D0BM00128G>.
- (33) Marasini, R.; Thanh Nguyen, T. D.; Rayamajhi, S.; Aryal, S. Synthesis and Characterization of a Tumor-Seeking LyP-1 Peptide Integrated Lipid-Polymer Composite Nanoparticle. *Mater. Adv.* **2020**, *1* (3), 469–480. <https://doi.org/10.1039/D0MA00203H>.
- (34) Abello, J.; Nguyen, T. D. T.; Marasini, R.; Aryal, S.; Weiss, M. L. Biodistribution of Gadolinium- and near Infrared-Labeled Human Umbilical Cord Mesenchymal Stromal Cell-Derived Exosomes in Tumor Bearing Mice. *Theranostics* **2019**, *9* (8), 2325–2345. <https://doi.org/10.7150/thno.30030>.

- (35) Han, X.; Xu, K.; Taratula, O.; Farsad, K. Applications of Nanoparticles in Biomedical Imaging. *Nanoscale* **2019**, *11* (3), 799–819. <https://doi.org/10.1039/C8NR07769J>.
- (36) Pitchaimani, A.; Nguyen, T. D. T.; Marasini, R.; Eliyapura, A.; Azizi, T.; Jaber-Douraki, M.; Aryal, S. Biomimetic Natural Killer Membrane Camouflaged Polymeric Nanoparticle for Targeted Bioimaging. *Adv. Funct. Mater.* **2019**, *29* (4), 1806817. <https://doi.org/10.1002/adfm.201806817>.
- (37) Thanh Nguyen, T. D.; Marasini, R.; Rayamajhi, S.; Aparicio, C.; Biller, D.; Aryal, S. Erythrocyte Membrane Concealed Paramagnetic Polymeric Nanoparticle for Contrast-Enhanced Magnetic Resonance Imaging. *Nanoscale* **2020**, *12* (6), 4137–4149. <https://doi.org/10.1039/D0NR00039F>.
- (38) Nguyen, T. D. T.; Aryal, S.; Pitchaimani, A.; Park, S.; Key, J.; Aryal, S. Biomimetic Surface Modification of Discoidal Polymeric Particles. *Nanomedicine Nanotechnol. Biol. Med.* **2019**, *16*, 79–87. <https://doi.org/10.1016/j.nano.2018.11.011>.
- (39) Nel, A. E.; Mädler, L.; Velegol, D.; Xia, T.; Hoek, E. M. V.; Somasundaran, P.; Klaessig, F.; Castranova, V.; Thompson, M. Understanding Biophysicochemical Interactions at the Nano–Bio Interface. *Nat. Mater.* **2009**, *8* (7), 543–557. <https://doi.org/10.1038/nmat2442>.
- (40) Rayamajhi, S.; Marchitto, J.; Nguyen, T. D. T.; Marasini, R.; Celia, C.; Aryal, S. PH-Responsive Cationic Liposome for Endosomal Escape Mediated Drug Delivery. *Colloids Surf. B Biointerfaces* **2020**, *188*, 110804. <https://doi.org/10.1016/j.colsurfb.2020.110804>.
- (41) Qiu, J.; Xia, Y. Killing Cancer Cells by Rupturing Their Lysosomes. *Nat. Nanotechnol.* **2020**, *15* (4), 252–253. <https://doi.org/10.1038/s41565-020-0639-z>.
- (42) Martins, J. P.; das Neves, J.; de la Fuente, M.; Celia, C.; Florindo, H.; Günday-Türeli, N.; Popat, A.; Santos, J. L.; Sousa, F.; Schmid, R.; Wolfram, J.; Sarmiento, B.; Santos, H. A. The Solid Progress of Nanomedicine. *Drug Deliv. Transl. Res.* **2020**. <https://doi.org/10.1007/s13346-020-00743-2>.
- (43) Marasini, R.; Nguyen, T.; Rayamajhi, S.; Aryal, S. Interaction of Tumor Homing LyP-1 Peptide Designed as Lipid-Polymer Hybrid Nanoparticle with Overexpressed Cell Surface Protein P32 Using Osteosarcoma Tumor Model. In *Chemical Biology and Interfaces*; American Chemical Society: Orlando, FL, USA, 2019; Vol. 257.
- (44) Marasini, Ramesh; Nguyen, Tuyen; Aryal, Santosh. Tumor-Associated Macrophage Specific Lipid-Polymer Hybrid Theranostic Nanoparticles. In *Nanomedicine for Immunotherapy*; University of Nebraska Medical College: Omaha, Nebraska, USA, 2018; Vol. 5.
- (45) Aryal, S., Nguyen, T., Pitchaimani, A. and Marasini, R. Biologically Inspired Design Consideration for Polymeric Anticancer Nanomedicine. In *Colloids and Interfaces*; AMERICAN CHEMICAL SOCIETY: Boston, MA, USA, 2018; Vol. 256.
- (46) Smith, B. R.; Gambhir, S. S. Nanomaterials for In Vivo Imaging. *Chem. Rev.* **2017**, *117* (3), 901–986. <https://doi.org/10.1021/acs.chemrev.6b00073>.
- (47) Blanco, E.; Shen, H.; Ferrari, M. Principles of Nanoparticle Design for Overcoming Biological Barriers to Drug Delivery. *Nat. Biotechnol.* **2015**, *33* (9), 941–951. <https://doi.org/10.1038/nbt.3330>.
- (48) Salvati, A.; Pitek, A. S.; Monopoli, M. P.; Prapainop, K.; Bombelli, F. B.; Hristov, D. R.; Kelly, P. M.; Åberg, C.; Mahon, E.; Dawson, K. A. Transferrin-Functionalized Nanoparticles Lose Their Targeting Capabilities When a Biomolecule Corona Adsorbs on the Surface. *Nat. Nanotechnol.* **2013**, *8* (2), 137–143. <https://doi.org/10.1038/nnano.2012.237>.

- (49) Dai, Q.; Wilhelm, S.; Ding, D.; Syed, A. M.; Sindhvani, S.; Zhang, Y.; Chen, Y. Y.; MacMillan, P.; Chan, W. C. W. Quantifying the Ligand-Coated Nanoparticle Delivery to Cancer Cells in Solid Tumors. *ACS Nano* **2018**, *12* (8), 8423–8435. <https://doi.org/10.1021/acsnano.8b03900>.
- (50) Wilhelm, S.; Tavares, A. J.; Dai, Q.; Ohta, S.; Audet, J.; Dvorak, H. F.; Chan, W. C. W. Analysis of Nanoparticle Delivery to Tumours. *Nat. Rev. Mater.* **2016**, *1* (5), 1–12. <https://doi.org/10.1038/natrevmats.2016.14>.
- (51) Cheng, Y.-H.; He, C.; Riviere, J. E.; Monteiro-Riviere, N. A.; Lin, Z. Meta-Analysis of Nanoparticle Delivery to Tumors Using a Physiologically Based Pharmacokinetic Modeling and Simulation Approach. *ACS Nano* **2020**, *14* (3), 3075–3095. <https://doi.org/10.1021/acsnano.9b08142>.
- (52) Kosaka, N.; Ogawa, M.; Choyke, P. L.; Kobayashi, H. Clinical Implications of Near-Infrared Fluorescence Imaging in Cancer. *Future Oncol. Lond. Engl.* **2009**, *5* (9), 1501–1511. <https://doi.org/10.2217/fon.09.109>.
- (53) Zhao, J.; Chen, J.; Ma, S.; Liu, Q.; Huang, L.; Chen, X.; Lou, K.; Wang, W. Recent Developments in Multimodality Fluorescence Imaging Probes. *Acta Pharm. Sin. B* **2018**, *8* (3), 320–338. <https://doi.org/10.1016/j.apsb.2018.03.010>.
- (54) Pan, D.; Schmieder, A. H.; Wickline, S. A.; Lanza, G. M. Manganese-Based MRI Contrast Agents: Past, Present and Future. *Tetrahedron* **2011**, *67* (44), 8431–8444. <https://doi.org/10.1016/j.tet.2011.07.076>.
- (55) Ersoy, H.; Rybicki, F. J. Biochemical Safety Profiles of Gadolinium-Based Extracellular Contrast Agents and Nephrogenic Systemic Fibrosis. *J. Magn. Reson. Imaging JMRI* **2007**, *26* (5), 1190–1197. <https://doi.org/10.1002/jmri.21135>.
- (56) Fukumura, D.; Jain, R. K. Tumor Microenvironment Abnormalities: Causes, Consequences, and Strategies to Normalize. *J. Cell. Biochem.* **2007**, *101* (4), 937–949. <https://doi.org/10.1002/jcb.21187>.
- (57) Price, L. S. L.; Stern, S. T.; Deal, A. M.; Kabanov, A. V.; Zamboni, W. C. A Reanalysis of Nanoparticle Tumor Delivery Using Classical Pharmacokinetic Metrics. *Sci. Adv.* **2020**, *6* (29), eaay9249. <https://doi.org/10.1126/sciadv.aay9249>.
- (58) Kano, M. R.; Bae, Y.; Iwata, C.; Morishita, Y.; Yashiro, M.; Oka, M.; Fujii, T.; Komuro, A.; Kiyono, K.; Kaminishi, M.; Hirakawa, K.; Ouchi, Y.; Nishiyama, N.; Kataoka, K.; Miyazono, K. Improvement of Cancer-Targeting Therapy, Using Nanocarriers for Intractable Solid Tumors by Inhibition of TGF- β Signaling. *Proc. Natl. Acad. Sci.* **2007**, *104* (9), 3460–3465. <https://doi.org/10.1073/pnas.0611660104>.
- (59) Cabral, H.; Matsumoto, Y.; Mizuno, K.; Chen, Q.; Murakami, M.; Kimura, M.; Terada, Y.; Kano, M. R.; Miyazono, K.; Uesaka, M.; Nishiyama, N.; Kataoka, K. Accumulation of Sub-100 Nm Polymeric Micelles in Poorly Permeable Tumours Depends on Size. *Nat. Nanotechnol.* **2011**, *6* (12), 815–823. <https://doi.org/10.1038/nnano.2011.166>.
- (60) Wei, R.; Liu, S.; Zhang, S.; Min, L.; Zhu, S. Cellular and Extracellular Components in Tumor Microenvironment and Their Application in Early Diagnosis of Cancers <https://www.hindawi.com/journals/acp/2020/6283796/> (accessed Jul 17, 2020). <https://doi.org/10.1155/2020/6283796>.
- (61) Harris, A. L. Hypoxia--a Key Regulatory Factor in Tumour Growth. *Nat. Rev. Cancer* **2002**, *2* (1), 38–47. <https://doi.org/10.1038/nrc704>.
- (62) Brown, J. M.; Wilson, W. R. Exploiting Tumour Hypoxia in Cancer Treatment. *Nat. Rev. Cancer* **2004**, *4* (6), 437–447. <https://doi.org/10.1038/nrc1367>.

- (63) Semenza, G. L. The Hypoxic Tumor Microenvironment: A Driving Force for Breast Cancer Progression. *Biochim. Biophys. Acta* **2016**, *1863* (3), 382–391. <https://doi.org/10.1016/j.bbamcr.2015.05.036>.
- (64) Gilkes, D. M.; Semenza, G. L. Role of Hypoxia-Inducible Factors in Breast Cancer Metastasis. *Future Oncol. Lond. Engl.* **2013**, *9* (11), 1623–1636. <https://doi.org/10.2217/fon.13.92>.
- (65) Behzadi, S.; Serpooshan, V.; Tao, W.; Hamaly, M. A.; Alkawareek, M. Y.; Dreaden, E. C.; Brown, D.; Alkilany, A. M.; Farokhzad, O. C.; Mahmoudi, M. Cellular Uptake of Nanoparticles: Journey Inside the Cell. *Chem. Soc. Rev.* **2017**, *46* (14), 4218–4244. <https://doi.org/10.1039/c6cs00636a>.
- (66) Foroozandeh, P.; Aziz, A. A. Insight into Cellular Uptake and Intracellular Trafficking of Nanoparticles. *Nanoscale Res. Lett.* **2018**, *13*. <https://doi.org/10.1186/s11671-018-2728-6>.
- (67) Kapara, A.; Brunton, V.; Graham, D.; Faulds, K. Investigation of Cellular Uptake Mechanism of Functionalised Gold Nanoparticles into Breast Cancer Using SERS. *Chem. Sci.* **2020**, *11* (22), 5819–5829. <https://doi.org/10.1039/D0SC01255F>.
- (68) Adjei, I. M.; Sharma, B.; Labhasetwar, V. Nanoparticles: Cellular Uptake and Cytotoxicity. In *Nanomaterial: Impacts on Cell Biology and Medicine*; Capco, D. G., Chen, Y., Eds.; Advances in Experimental Medicine and Biology; Springer Netherlands: Dordrecht, 2014; pp 73–91. https://doi.org/10.1007/978-94-017-8739-0_5.
- (69) Huotari, J.; Helenius, A. Endosome Maturation. *EMBO J.* **2011**, *30* (17), 3481–3500. <https://doi.org/10.1038/emboj.2011.286>.
- (70) *The Current Status of Nanomedicine in the USA in Comparison to the Rest of the World*; Committee Meeting on the National Nanotechnology Initiative: A Quadrennial Review; 2019.
- (71) Stone, J.; Jackson, S.; Wright, D. Biological Applications of Gold Nanorods. *Wiley Interdiscip. Rev. Nanomed. Nanobiotechnol.* **2011**, *3* (1), 100–109. <https://doi.org/10.1002/wnan.120>.
- (72) Yang, D.-P.; Cui, D.-X. Advances and Prospects of Gold Nanorods. *Chem. – Asian J.* **2008**, *3* (12), 2010–2022. <https://doi.org/10.1002/asia.200800195>.
- (73) Huang, H.; He, C.; Zeng, Y.; Xia, X.; Yu, X.; Yi, P.; Chen, Z. Preparation and Optical Properties of Worm-like Gold Nanorods. *J. Colloid Interface Sci.* **2008**, *322* (1), 136–142. <https://doi.org/10.1016/j.jcis.2008.03.004>.
- (74) Gui, C.; Cui, D.-X. Functionalized Gold Nanorods for Tumor Imaging and Targeted Therapy. *Cancer Biol. Med.* **2012**, *9* (4), 221–233. <https://doi.org/10.7497/j.issn.2095-3941.2012.04.002>.
- (75) Boisselier, E.; Astruc, D. Gold Nanoparticles in Nanomedicine: Preparations, Imaging, Diagnostics, Therapies and Toxicity. *Chem. Soc. Rev.* **2009**, *38* (6), 1759–1782. <https://doi.org/10.1039/B806051G>.
- (76) Murphy, C. J.; Gole, A. M.; Stone, J. W.; Sisco, P. N.; Alkilany, A. M.; Goldsmith, E. C.; Baxter, S. C. Gold Nanoparticles in Biology: Beyond Toxicity to Cellular Imaging. *Acc. Chem. Res.* **2008**, *41* (12), 1721–1730. <https://doi.org/10.1021/ar800035u>.
- (77) Pitchaimani, A.; Nguyen, T. D. T.; Wang, H.; H. Bossmann, S.; Aryal, S. Design and Characterization of Gadolinium Infused Theranostic Liposomes. *RSC Adv.* **2016**, *6* (43), 36898–36905. <https://doi.org/10.1039/C6RA00552G>.

- (78) Huang, X.; Jain, P. K.; El-Sayed, I. H.; El-Sayed, M. A. Plasmonic Photothermal Therapy (PPTT) Using Gold Nanoparticles. *Lasers Med. Sci.* **2007**, *23* (3), 217. <https://doi.org/10.1007/s10103-007-0470-x>.
- (79) Gormley, A. J.; Larson, N.; Banisadr, A.; Robinson, R.; Frazier, N.; Ray, A.; Ghandehari, H. Plasmonic Photothermal Therapy Increases the Tumor Mass Penetration of HEMA Copolymers. *J. Controlled Release* **2013**, *166* (2), 130–138. <https://doi.org/10.1016/j.jconrel.2012.12.007>.
- (80) Weissleder, R. A clearer vision for *in vivo* imaging https://www.nature.com/articles/nbt0401_316 (accessed Nov 27, 2017). <https://doi.org/10.1038/86684>.
- (81) Smith, A. M.; Mancini, M. C.; Nie, S. Second Window for *in Vivo* Imaging. *Nat. Nanotechnol.* **2009**, *4* (11), 710–711. <https://doi.org/10.1038/nnano.2009.326>.
- (82) Chen, H.; Guan, Y.; Wang, S.; Ji, Y.; Gong, M.; Wang, L. Turn-On Detection of a Cancer Marker Based on Near-Infrared Luminescence Energy Transfer from NaYF₄:Yb,Tm/NaGdF₄ Core–Shell Upconverting Nanoparticles to Gold Nanorods. *Langmuir* **2014**, *30* (43), 13085–13091. <https://doi.org/10.1021/la502753e>.
- (83) Liu, Y.; Yang, M.; Zhang, J.; Zhi, X.; Li, C.; Zhang, C.; Pan, F.; Wang, K.; Yang, Y.; Martinez de la Fuentea, J.; Cui, D. Human Induced Pluripotent Stem Cells for Tumor Targeted Delivery of Gold Nanorods and Enhanced Photothermal Therapy. *ACS Nano* **2016**, *10* (2), 2375–2385. <https://doi.org/10.1021/acsnano.5b07172>.
- (84) Aryal, S.; B.k.c., R.; Dharmaraj, N.; Bhattarai, N.; Kim, C. H.; Kim, H. Y. Spectroscopic Identification of SAu Interaction in Cysteine Capped Gold Nanoparticles. *Spectrochim. Acta. A. Mol. Biomol. Spectrosc.* **2006**, *63* (1), 160–163. <https://doi.org/10.1016/j.saa.2005.04.048>.
- (85) Arunkumar, P.; Raju, B.; Vasantharaja, R.; Vijayaraghavan, S.; Preetham Kumar, B.; Jeganathan, K.; Premkumar, K. Near Infra-Red Laser Mediated Photothermal and Antitumor Efficacy of Doxorubicin Conjugated Gold Nanorods with Reduced Cardiotoxicity in Swiss Albino Mice. *Nanomedicine Nanotechnol. Biol. Med.* **2015**, *11* (6), 1435–1444. <https://doi.org/10.1016/j.nano.2015.03.012>.
- (86) de Dios, A. S.; Díaz-García, M. E. Multifunctional Nanoparticles: Analytical Prospects. *Anal. Chim. Acta* **2010**, *666* (1), 1–22. <https://doi.org/10.1016/j.aca.2010.03.038>.
- (87) Aryal, S.; Grailer, J. J.; Pilla, S.; Steeber, D. A.; Gong, S. Doxorubicin Conjugated Gold Nanoparticles as Water-Soluble and PH-Responsive Anticancer Drug Nanocarriers. *J. Mater. Chem.* **2009**, *19* (42), 7879–7884. <https://doi.org/10.1039/B914071A>.
- (88) Huang, X.; Jain, P. K.; El-Sayed, I. H.; El-Sayed, M. A. Gold Nanoparticles: Interesting Optical Properties and Recent Applications in Cancer Diagnostics and Therapy. *Nanomed.* **2007**, *2* (5), 681–693. <https://doi.org/10.2217/17435889.2.5.681>.
- (89) Kennedy, L. C.; Bickford, L. R.; Lewinski, N. A.; Coughlin, A. J.; Hu, Y.; Day, E. S.; West, J. L.; Drezek, R. A. A New Era for Cancer Treatment: Gold-Nanoparticle-Mediated Thermal Therapies. *Small* **2011**, *7* (2), 169–183. <https://doi.org/10.1002/sml.201000134>.
- (90) Nolsøe, C. P.; Torp-Pedersen, S.; Burcharth, F.; Horn, T.; Pedersen, S.; Christensen, N. E.; Olldag, E. S.; Andersen, P. H.; Karstrup, S.; Lorentzen, T. Interstitial Hyperthermia of Colorectal Liver Metastases with a US-Guided Nd-YAG Laser with a Diffuser Tip: A Pilot Clinical Study. *Radiology* **1993**, *187* (2), 333–337. <https://doi.org/10.1148/radiology.187.2.8475269>.

- (91) Vogl, T.; Mack, M.; Straub, R.; Zangos, S.; Woitaschek, D.; Eichler, K.; Engelmann, K. [Thermal ablation of liver metastases. Current status and prospects]. *Radiol.* **2001**, *41* (1), 49–55.
- (92) Tong, L.; Zhao, Y.; Huff, T. B.; Hansen, M. N.; Wei, A.; Cheng, J.-X. Gold Nanorods Mediate Tumor Cell Death by Compromising Membrane Integrity. *Adv. Mater.* **2007**, *19* (20), 3136–3141. <https://doi.org/10.1002/adma.200701974>.
- (93) Hirsch, L. R.; Stafford, R. J.; Bankson, J. A.; Sershen, S. R.; Rivera, B.; Price, R. E.; Hazle, J. D.; Halas, N. J.; West, J. L. Nanoshell-Mediated near-Infrared Thermal Therapy of Tumors under Magnetic Resonance Guidance. *Proc. Natl. Acad. Sci.* **2003**, *100* (23), 13549–13554. <https://doi.org/10.1073/pnas.2232479100>.
- (94) O’Neal, D. P.; Hirsch, L. R.; Halas, N. J.; Payne, J. D.; West, J. L. Photo-Thermal Tumor Ablation in Mice Using near Infrared-Absorbing Nanoparticles. *Cancer Lett.* **2004**, *209* (2), 171–176. <https://doi.org/10.1016/j.canlet.2004.02.004>.
- (95) Link, S.; El-Sayed, M. A. Shape and Size Dependence of Radiative, Non-Radiative and Photothermal Properties of Gold Nanocrystals. *Int. Rev. Phys. Chem.* **2000**, *19* (3), 409–453. <https://doi.org/10.1080/01442350050034180>.
- (96) Kelly, K. L.; Coronado, E.; Zhao, L. L.; Schatz, G. C. The Optical Properties of Metal Nanoparticles: The Influence of Size, Shape, and Dielectric Environment. *J. Phys. Chem. B* **2003**, *107* (3), 668–677. <https://doi.org/10.1021/jp026731y>.
- (97) Liu, X.; Huang, N.; Li, H.; Wang, H.; Jin, Q.; Ji, J. Multidentate Polyethylene Glycol Modified Gold Nanorods for in Vivo Near-Infrared Photothermal Cancer Therapy. *ACS Appl. Mater. Interfaces* **2014**, *6* (8), 5657–5668. <https://doi.org/10.1021/am5001823>.
- (98) Gobeli, D. A.; Yang, J. J.; El-Sayed, M. A. Laser Multiphoton Ionization-Dissociation Mass Spectrometry. *Chem. Rev.* **1985**, *85* (6), 529–554. <https://doi.org/10.1021/cr00070a002>.
- (99) Dickerson, E. B.; Dreaden, E. C.; Huang, X.; El-Sayed, I. H.; Chu, H.; Pushpanketh, S.; McDonald, J. F.; El-Sayed, M. A. Gold Nanorod Assisted Near-Infrared Plasmonic Photothermal Therapy (PPTT) of Squamous Cell Carcinoma in Mice. *Cancer Lett.* **2008**, *269* (1), 57–66. <https://doi.org/10.1016/j.canlet.2008.04.026>.
- (100) Harris, J. M.; Chess, R. B. Effect of Pegylation on Pharmaceuticals. *Nat. Rev. Drug Discov.* **2003**, *2* (3), 214–221. <https://doi.org/10.1038/nrd1033>.
- (101) Huff, T. B.; Hansen, M. N.; Zhao, Y.; Cheng, J.-X.; Wei, A. Controlling the Cellular Uptake of Gold Nanorods. *Langmuir* **2007**, *23* (4), 1596–1599. <https://doi.org/10.1021/la062642r>.
- (102) Liao, H.; Hafner, J. H. Gold Nanorod Bioconjugates. *Chem. Mater.* **2005**, *17* (18), 4636–4641. <https://doi.org/10.1021/cm050935k>.
- (103) Niidome, T.; Yamagata, M.; Okamoto, Y.; Akiyama, Y.; Takahashi, H.; Kawano, T.; Katayama, Y.; Niidome, Y. PEG-Modified Gold Nanorods with a Stealth Character for in Vivo Applications. *J. Controlled Release* **2006**, *114* (3), 343–347. <https://doi.org/10.1016/j.jconrel.2006.06.017>.
- (104) Chen, X.; Hou, Y.; Tohme, M.; Park, R.; Khankaldyyan, V.; Gonzales-Gomez, I.; Bading, J. R.; Laug, W. E.; Conti, P. S. Pegylated Arg-Gly-Asp Peptide: ⁶⁴Cu Labeling and PET Imaging of Brain Tumor Avβ3-Integrin Expression. *J. Nucl. Med.* **2004**, *45* (10), 1776–1783.
- (105) Maltzahn, G. von; Park, J.-H.; Agrawal, A.; Bandaru, N. K.; Das, S. K.; Sailor, M. J.; Bhatia, S. N. Computationally Guided Photothermal Tumor Therapy Using Long-

- Circulating Gold Nanorod Antennas. *Cancer Res.* **2009**, *69* (9), 3892–3900. <https://doi.org/10.1158/0008-5472.CAN-08-4242>.
- (106) Pitchaimani, A.; Nguyen, T. D. T.; Koirala, M.; Zhang, Y.; Aryal, S. Impact of Cell Adhesion and Migration on Nanoparticle Uptake and Cellular Toxicity. *Toxicol. In Vitro* **2017**, *43*, 29–39. <https://doi.org/10.1016/j.tiv.2017.05.020>.
- (107) Aryal, S.; Hu, C.-M. J.; Zhang, L. Polymer–Cisplatin Conjugate Nanoparticles for Acid-Responsive Drug Delivery. *ACS Nano* **2010**, *4* (1), 251–258. <https://doi.org/10.1021/nn9014032>.
- (108) Huff, T. B.; Tong, L.; Zhao, Y.; Hansen, M. N.; Cheng, J.-X.; Wei, A. Hyperthermic Effects of Gold Nanorods on Tumor Cells. *Nanomed.* **2007**, *2* (1), 125–132. <https://doi.org/10.2217/17435889.2.1.125>.
- (109) Koirala, M. B.; Nguyen, T. D. T.; Pitchaimani, A.; Choi, S.-O.; Aryal, S. Synthesis and Characterization of Biomimetic Hydroxyapatite Nanoconstruct Using Chemical Gradient across Lipid Bilayer. *ACS Appl. Mater. Interfaces* **2015**, *7* (49), 27382–27390. <https://doi.org/10.1021/acsami.5b09042>.
- (110) Ge, Z.; Cahill, D. G.; Braun, P. V. AuPd Metal Nanoparticles as Probes of Nanoscale Thermal Transport in Aqueous Solution. *J. Phys. Chem. B* **2004**, *108* (49), 18870–18875. <https://doi.org/10.1021/jp048375k>.
- (111) Schmidt, A. J.; Alper, J. D.; Chiesa, M.; Chen, G.; Das, S. K.; Hamad-Schifferli, K. Probing the Gold Nanorod–Ligand–Solvent Interface by Plasmonic Absorption and Thermal Decay. *J. Phys. Chem. C* **2008**, *112* (35), 13320–13323. <https://doi.org/10.1021/jp8051888>.
- (112) Huang, J.; Park, J.; Wang, W.; Murphy, C. J.; Cahill, D. G. Ultrafast Thermal Analysis of Surface Functionalized Gold Nanorods in Aqueous Solution. *ACS Nano* **2013**, *7* (1), 589–597. <https://doi.org/10.1021/nn304738u>.
- (113) Pitchaimani, A.; Nguyen, T. D. T.; Maurmann, L.; Key, J.; Bossmann, S. H.; Aryal, S. Gd3 + Tethered Gold Nanorods for Combined Magnetic Resonance Imaging and Photo-Thermal Therapy <https://www.ingentaconnect.com/content/asp/jbn/2017/00000013/00000004/art00006> (accessed May 7, 2020). <https://doi.org/info:doi/10.1166/jbn.2017.2362>.
- (114) Wright, L. B.; Rodger, P. M.; Corni, S.; Walsh, T. R. GolP-CHARMM: First-Principles Based Force Fields for the Interaction of Proteins with Au(111) and Au(100). *J. Chem. Theory Comput.* **2013**, *9* (3), 1616–1630. <https://doi.org/10.1021/ct301018m>.
- (115) Lee, H.; Venable, R. M.; MacKerell, A. D.; Pastor, R. W. Molecular Dynamics Studies of Polyethylene Oxide and Polyethylene Glycol: Hydrodynamic Radius and Shape Anisotropy. *Biophys. J.* **2008**, *95* (4), 1590–1599. <https://doi.org/10.1529/biophysj.108.133025>.
- (116) Phillips, J. C.; Braun, R.; Wang, W.; Gumbart, J.; Tajkhorshid, E.; Villa, E.; Chipot, C.; Skeel, R. D.; Kalé, L.; Schulten, K. Scalable Molecular Dynamics with NAMD. *J. Comput. Chem.* **2005**, *26* (16), 1781–1802. <https://doi.org/10.1002/jcc.20289>.
- (117) Plimpton, S. Fast Parallel Algorithms for Short-Range Molecular Dynamics. *J. Comput. Phys.* **1995**, *117* (1), 1–19. <https://doi.org/10.1006/jcph.1995.1039>.
- (118) Müller-Plathe, F. A Simple Nonequilibrium Molecular Dynamics Method for Calculating the Thermal Conductivity. *J. Chem. Phys.* **1997**, *106* (14), 6082–6085. <https://doi.org/10.1063/1.473271>.

- (119) Iori, F.; Corni, S. Including Image Charge Effects in the Molecular Dynamics Simulations of Molecules on Metal Surfaces. *J. Comput. Chem.* **2008**, *29* (10), 1656–1666. <https://doi.org/10.1002/jcc.20928>.
- (120) Vanommeslaeghe, K.; Raman, E. P.; MacKerell, A. D. Automation of the CHARMM General Force Field (CGenFF) II: Assignment of Bonded Parameters and Partial Atomic Charges. *J. Chem. Inf. Model.* **2012**, *52* (12), 3155–3168. <https://doi.org/10.1021/ci3003649>.
- (121) Miyamoto, S.; Kollman, P. A. Settle: An Analytical Version of the SHAKE and RATTLE Algorithm for Rigid Water Models. *J. Comput. Chem.* **1992**, *13* (8), 952–962. <https://doi.org/10.1002/jcc.540130805>.
- (122) Andersen, H. C. Rattle: A “Velocity” Version of the Shake Algorithm for Molecular Dynamics Calculations. *J. Comput. Phys.* **1983**, *52* (1), 24–34. [https://doi.org/10.1016/0021-9991\(83\)90014-1](https://doi.org/10.1016/0021-9991(83)90014-1).
- (123) Darden, T.; York, D.; Pedersen, L. Particle Mesh Ewald: An $N\log(N)$ Method for Ewald Sums in Large Systems. *J. Chem. Phys.* **1993**, *98*, 10089–10092. <https://doi.org/10.1063/1.464397>.
- (124) Feller, S. E.; Zhang, Y.; Pastor, R. W.; Brooks, B. R. Constant Pressure Molecular Dynamics Simulation: The Langevin Piston Method. *J. Chem. Phys.* **1995**, *103*, 4613–4621. <https://doi.org/10.1063/1.470648>.
- (125) Kell, G. S. Thermodynamic and Transport Properties of Fluid Water. In *The Physics and Physical Chemistry of Water*; Franks, F., Ed.; Water; Springer New York: Boston, MA, 1972; pp 363–412. https://doi.org/10.1007/978-1-4684-8334-5_10.
- (126) Mark, P.; Nilsson, L. Structure and Dynamics of the TIP3P, SPC, and SPC/E Water Models at 298 K. *J. Phys. Chem. A* **2001**, *105* (43), 9954–9960. <https://doi.org/10.1021/jp003020w>.
- (127) Vega, C.; Sanz, E.; Abascal, J. L. F. The Melting Temperature of the Most Common Models of Water. *J. Chem. Phys.* **2005**, *122* (11), 114507. <https://doi.org/10.1063/1.1862245>.
- (128) Grabinski, C.; Schaeublin, N.; Wijaya, A.; D’Couto, H.; Baxamusa, S. H.; Hamad-Schifferli, K.; Hussain, S. M. Effect of Gold Nanorod Surface Chemistry on Cellular Response. *ACS Nano* **2011**, *5* (4), 2870–2879. <https://doi.org/10.1021/nn103476x>.
- (129) Dykman, L.; Khlebtsov, N. Gold Nanoparticles in Biomedical Applications: Recent Advances and Perspectives. *Chem. Soc. Rev.* **2012**, *41* (6), 2256–2282. <https://doi.org/10.1039/C1CS15166E>.
- (130) Sztandera, K.; Gorzkiewicz, M.; Klajnert-Maculewicz, B. Nanocarriers in Photodynamic Therapy—in Vitro and in Vivo Studies. *Wiley Interdiscip. Rev. Nanomed. Nanobiotechnol.* *0* (0), e1509. <https://doi.org/10.1002/wnan.1599>.
- (131) Castano, A. P.; Mroz, P.; Hamblin, M. R. Photodynamic Therapy and Anti-Tumour Immunity. *Nat. Rev. Cancer* **2006**, *6* (7), 535–545. <https://doi.org/10.1038/nrc1894>.
- (132) Zhu, H.; Cheng, P.; Chen, P.; Pu, K. Recent Progress in the Development of Near-Infrared Organic Photothermal and Photodynamic Nanotherapeutics. *Biomater. Sci.* **2018**, *6* (4), 746–765. <https://doi.org/10.1039/C7BM01210A>.
- (133) Eustis, S.; A. El-Sayed, M. Why Gold Nanoparticles Are More Precious than Pretty Gold: Noble Metal Surface Plasmon Resonance and Its Enhancement of the Radiative and Nonradiative Properties of Nanocrystals of Different Shapes. *Chem. Soc. Rev.* **2006**, *35* (3), 209–217. <https://doi.org/10.1039/B514191E>.

- (134) Shanmugam, V.; Selvakumar, S.; Yeh, C.-S. Near-Infrared Light-Responsive Nanomaterials in Cancer Therapeutics. *Chem. Soc. Rev.* **2014**, *43* (17), 6254–6287. <https://doi.org/10.1039/C4CS00011K>.
- (135) Zaharie-Butucel, D.; Potara, M.; Suarasan, S.; Licarete, E.; Astilean, S. Efficient Combined Near-Infrared-Triggered Therapy: Phototherapy over Chemotherapy in Chitosan-Reduced Graphene Oxide-IR820 Dye-Doxorubicin Nanoplatforms. *J. Colloid Interface Sci.* **2019**, *552*, 218–229. <https://doi.org/10.1016/j.jcis.2019.05.050>.
- (136) Huang, X.; El-Sayed, I. H.; Qian, W.; El-Sayed, M. A. Cancer Cell Imaging and Photothermal Therapy in the Near-Infrared Region by Using Gold Nanorods. *J. Am. Chem. Soc.* **2006**, *128* (6), 2115–2120. <https://doi.org/10.1021/ja057254a>.
- (137) Rosensweig, R. E. Heating Magnetic Fluid with Alternating Magnetic Field. *J. Magn. Magn. Mater.* **2002**, *252*, 370–374. [https://doi.org/10.1016/S0304-8853\(02\)00706-0](https://doi.org/10.1016/S0304-8853(02)00706-0).
- (138) Thapa, P.; Li, M.; Bio, M.; Rajaputra, P.; Nkepan, G.; Sun, Y.; Woo, S.; You, Y. Far-Red Light-Activatable Prodrug of Paclitaxel for the Combined Effects of Photodynamic Therapy and Site-Specific Paclitaxel Chemotherapy. *J. Med. Chem.* **2016**, *59* (7), 3204–3214. <https://doi.org/10.1021/acs.jmedchem.5b01971>.
- (139) Huang, P.; Rong, P.; Jin, A.; Yan, X.; Zhang, M. G.; Lin, J.; Hu, H.; Wang, Z.; Yue, X.; Li, W.; Niu, G.; Zeng, W.; Wang, W.; Zhou, K.; Chen, X. Dye-Loaded Ferritin Nanocages for Multimodal Imaging and Photothermal Therapy. *Adv. Mater.* **2014**, *26* (37), 6401–6408. <https://doi.org/10.1002/adma.201400914>.
- (140) Masotti, A.; Vicennati, P.; Boschi, F.; Calderan, L.; Sbarbati, A.; Ortaggi, G. A Novel Near-Infrared Indocyanine Dye–Polyethylenimine Conjugate Allows DNA Delivery Imaging in Vivo. *Bioconjug. Chem.* **2008**, *19* (5), 983–987. <https://doi.org/10.1021/bc700356f>.
- (141) Yen, S. K.; Jańczewski, D.; Lakshmi, J. L.; Dolmanan, S. B.; Tripathy, S.; Ho, V. H. B.; Vijayaragavan, V.; Hariharan, A.; Padmanabhan, P.; Bhakoo, K. K.; Sudhakaran, T.; Ahmed, S.; Zhang, Y.; Tamil Selvan, S. Design and Synthesis of Polymer-Functionalized NIR Fluorescent Dyes–Magnetic Nanoparticles for Bioimaging. *ACS Nano* **2013**, *7* (8), 6796–6805. <https://doi.org/10.1021/nn401734t>.
- (142) James, N. S.; Chen, Y.; Joshi, P.; Ohulchansky, T. Y.; Ethirajan, M.; Henary, M.; Streckowski, L.; Pandey, R. K. Evaluation of Polymethine Dyes as Potential Probes for Near Infrared Fluorescence Imaging of Tumors: Part - 1. *Theranostics* **2013**, *3* (9), 692–702. <https://doi.org/10.7150/thno.5922>.
- (143) Harrison, V. S. R.; Carney, C. E.; Macrenaris, K. W.; Meade, T. J. A Multimeric MR-Optical Contrast Agent for Multimodal Imaging. *Chem. Commun.* **2014**, *50* (78), 11469–11471. <https://doi.org/10.1039/C4CC05651E>.
- (144) Harrison, V. S. R.; Carney, C. E.; MacRenaris, K. W.; Waters, E. A.; Meade, T. J. Multimeric Near IR–MR Contrast Agent for Multimodal In Vivo Imaging. *J. Am. Chem. Soc.* **2015**, *137* (28), 9108–9116. <https://doi.org/10.1021/jacs.5b04509>.
- (145) Weissleder, R.; Ntziachristos, V. Shedding Light onto Live Molecular Targets. *Nat. Med.* **2003**, *9* (1), 123–128. <https://doi.org/10.1038/nm0103-123>.
- (146) Berezin, M. Y.; Lee, H.; Akers, W.; Achilefu, S. Near Infrared Dyes as Lifetime Solvatochromic Probes for Micropolarity Measurements of Biological Systems. *Biophys. J.* **2007**, *93* (8), 2892–2899. <https://doi.org/10.1529/biophysj.107.111609>.

- (147) Conceição, D. S.; Ferreira, D. P.; Ferreira, L. F. V. Photochemistry and Cytotoxicity Evaluation of Heptamethinecyanine Near Infrared (NIR) Dyes. *Int. J. Mol. Sci.* **2013**, *14* (9), 18557–18571. <https://doi.org/10.3390/ijms140918557>.
- (148) Saxena, V.; Sadoqi, M.; Shao, J. Degradation Kinetics of Indocyanine Green in Aqueous Solution. *J. Pharm. Sci.* **2003**, *92* (10), 2090–2097. <https://doi.org/10.1002/jps.10470>.
- (149) Feng, Z.; Yu, X.; Jiang, M.; Zhu, L.; Zhang, Y.; Yang, W.; Xi, W.; Li, G.; Qian, J. Excretable IR-820 for *in Vivo* NIR-II Fluorescence Cerebrovascular Imaging and Photothermal Therapy of Subcutaneous Tumor. *Theranostics* **2019**, *9* (19), 5706–5719. <https://doi.org/10.7150/thno.31332>.
- (150) Chen, Y.; Li, Z.; Wang, H.; Wang, Y.; Han, H.; Jin, Q.; Ji, J. IR-780 Loaded Phospholipid Mimicking Homopolymeric Micelles for Near-IR Imaging and Photothermal Therapy of Pancreatic Cancer. *ACS Appl. Mater. Interfaces* **2016**, *8* (11), 6852–6858. <https://doi.org/10.1021/acsami.6b00251>.
- (151) Kumar, P.; Srivastava, R. IR 820 Stabilized Multifunctional Polycaprolactone Glycol Chitosan Composite Nanoparticles for Cancer Therapy. *RSC Adv.* **2015**, *5* (69), 56162–56170. <https://doi.org/10.1039/C5RA05997F>.
- (152) Srinivasan, S.; Manchanda, R.; Fernandez-Fernandez, A.; Lei, T.; McGoron, A. J. Near-Infrared Fluorescing IR820-Chitosan Conjugate for Multifunctional Cancer Theranostic Applications. *J. Photochem. Photobiol. B* **2013**, *119*, 52–59. <https://doi.org/10.1016/j.jphotobiol.2012.12.008>.
- (153) Prajapati, S. I.; Martinez, C. O.; Bahadur, A. N.; Wu, I. Q.; Zheng, W.; Lechleiter, J. D.; McManus, L. M.; Chisholm, G. B.; Michalek, J. E.; Shireman, P. K.; Keller, C. Near-Infrared Imaging of Injured Tissue in Living Subjects Using IR-820. *Mol. Imaging* **2009**, *8* (1), 45–54.
- (154) James, N. S.; Ohulchanskyy, T. Y.; Chen, Y.; Joshi, P.; Zheng, X.; Goswami, L. N.; Pandey, R. K. Comparative Tumor Imaging and PDT Efficacy of HPPH Conjugated in the Mono- and Di-Forms to Various Polymethine Cyanine Dyes: Part - 2. *Theranostics* **2013**, *3* (9), 703–718. <https://doi.org/10.7150/thno.5923>.
- (155) Pandey, R. K.; James, N.; Chen, Y.; Dobhal, M. P. Cyanine Dye-Based Compounds for Tumor Imaging With and Without Photodynamic Therapy. In *Heterocyclic Polymethine Dyes: Synthesis, Properties and Applications*; Streckowski, L., Ed.; Topics in Heterocyclic Chemistry; Springer: Berlin, Heidelberg, 2008; pp 41–74. https://doi.org/10.1007/7081_2008_113.
- (156) Yen, S. K.; Jańczewski, D.; Lakshmi, J. L.; Dolmanan, S. B.; Tripathy, S.; Ho, V. H. B.; Vijayaragavan, V.; Hariharan, A.; Padmanabhan, P.; Bhakoo, K. K.; Sudhakaran, T.; Ahmed, S.; Zhang, Y.; Tamil Selvan, S. Design and Synthesis of Polymer-Functionalized NIR Fluorescent Dyes–Magnetic Nanoparticles for Bioimaging. *ACS Nano* **2013**, *7* (8), 6796–6805. <https://doi.org/10.1021/nn401734t>.
- (157) Srinivasan, S.; Manchanda, R.; Fernandez-Fernandez, A.; Lei, T.; McGoron, A. J. Near-Infrared Fluorescing IR820-Chitosan Conjugate for Multifunctional Cancer Theranostic Applications. *J. Photochem. Photobiol. B* **2013**, *119*, 52–59. <https://doi.org/10.1016/j.jphotobiol.2012.12.008>.
- (158) Melamed, J. R.; Edelstein, R. S.; Day, E. S. Elucidating the Fundamental Mechanisms of Cell Death Triggered by Photothermal Therapy. *ACS Nano* **2015**, *9* (1), 6–11. <https://doi.org/10.1021/acs.nano.5b00021>.

- (159) Pitchaimani, A.; Nguyen, T. D. T.; Aryal, S. Natural Killer Cell Membrane Infused Biomimetic Liposomes for Targeted Tumor Therapy. *Biomaterials* **2018**, *160*, 124–137. <https://doi.org/10.1016/j.biomaterials.2018.01.018>.
- (160) Hu, C.-M. J.; Kaushal, S.; Cao, H. S. T.; Aryal, S.; Sartor, M.; Esener, S.; Bouvet, M.; Zhang, L. Half-Antibody Functionalized Lipid–Polymer Hybrid Nanoparticles for Targeted Drug Delivery to Carcinoembryonic Antigen Presenting Pancreatic Cancer Cells. *Mol. Pharm.* **2010**, *7* (3), 914–920. <https://doi.org/10.1021/mp900316a>.
- (161) Nguyen, T. D. T.; Pitchaimani, A.; Aryal, S. Engineered Nanomedicine with Alendronic Acid Corona Improves Targeting to Osteosarcoma. *Sci. Rep.* **2016**, *6* (1), 36707. <https://doi.org/10.1038/srep36707>.
- (162) Pridgen, E. M.; Langer, R.; Farokhzad, O. C. Biodegradable, Polymeric Nanoparticle Delivery Systems for Cancer Therapy. *Nanomed.* **2007**, *2* (5), 669–680. <https://doi.org/10.2217/17435889.2.5.669>.
- (163) Aryal, S.; Rayamajhi, S.; Nguyen, T.; Marasini, R. Re-Engineering Immuno-Exosome as Theranostics. In ABSTRACTS OF PAPERS OF THE AMERICAN CHEMICAL SOCIETY (Vol. 258). 1155 16TH ST, NW, WASHINGTON, DC 20036 USA: AMER CHEMICAL SOC. In *Re-engineering immuno-exosome as theranostics.*; AMERICAN CHEMICAL SOCIETY: Boston, MA, 2019; Vol. 258.
- (164) Shi, C.; Wu, J. B.; Pan, D. Review on Near-Infrared Heptamethine Cyanine Dyes as Theranostic Agents for Tumor Imaging, Targeting, and Photodynamic Therapy. *J. Biomed. Opt.* **2016**, *21* (5), 050901. <https://doi.org/10.1117/1.JBO.21.5.050901>.
- (165) Marasini, R.; Pitchaimani, A.; Thanh Nguyen, T. D.; Comer, J.; Aryal, S. The Influence of Polyethylene Glycol Passivation on the Surface Plasmon Resonance Induced Photothermal Properties of Gold Nanorods. *Nanoscale* **2018**, *10* (28), 13684–13693. <https://doi.org/10.1039/C8NR03026J>.
- (166) Pérez-Hernández, M.; del Pino, P.; Mitchell, S. G.; Moros, M.; Stepien, G.; Pelaz, B.; Parak, W. J.; Gálvez, E. M.; Pardo, J.; de la Fuente, J. M. Dissecting the Molecular Mechanism of Apoptosis during Photothermal Therapy Using Gold Nanoprisms. *ACS Nano* **2015**, *9* (1), 52–61. <https://doi.org/10.1021/nn505468v>.
- (167) Bear, A. S.; Kennedy, L. C.; Young, J. K.; Perna, S. K.; Almeida, J. P. M.; Lin, A. Y.; Eckels, P. C.; Drezek, R. A.; Foster, A. E. Elimination of Metastatic Melanoma Using Gold Nanoshell-Enabled Photothermal Therapy and Adoptive T Cell Transfer. *PLOS ONE* **2013**, *8* (7), e69073. <https://doi.org/10.1371/journal.pone.0069073>.
- (168) Zhang, L.; Zhang, L. Lipid–Polymer Hybrid Nanoparticles: Synthesis, Characterization and Applications. *Nano LIFE* **2010**, *01* (01n02), 163–173. <https://doi.org/10.1142/S179398441000016X>.
- (169) Zhang, L.; Chan, J. M.; Gu, F. X.; Rhee, J.-W.; Wang, A. Z.; Radovic-Moreno, A. F.; Alexis, F.; Langer, R.; Farokhzad, O. C. Self-Assembled Lipid–Polymer Hybrid Nanoparticles: A Robust Drug Delivery Platform. *ACS Nano* **2008**, *2* (8), 1696–1702. <https://doi.org/10.1021/nn800275r>.
- (170) Silva, A. D. R.; Stocco, T. D.; Granato, A. E. C.; Harb, S. V.; Afewerki, S.; Bassous, N. J.; Hammer, P.; Webster, T. J.; Marciano, F. R.; Lobo, A. O. Chapter 2 - Recent Advances in Nanostructured Polymer Composites for Biomedical Applications. In *Nanostructured Polymer Composites for Biomedical Applications*; Swain, S. K., Jawaid, M., Eds.; Micro and Nano Technologies; Elsevier, 2019; pp 21–52. <https://doi.org/10.1016/B978-0-12-816771-7.00002-8>.

- (171) Clawson, C.; Ton, L.; Aryal, S.; Fu, V.; Esener, S.; Zhang, L. Synthesis and Characterization of Lipid–Polymer Hybrid Nanoparticles with PH-Triggered Poly(Ethylene Glycol) Shedding. *Langmuir* **2011**, *27* (17), 10556–10561. <https://doi.org/10.1021/la202123e>.
- (172) Aryal, S.; Hu, C.-M. J.; Zhang, L. Polymeric Nanoparticles with Precise Ratiometric Control over Drug Loading for Combination Therapy. *Mol. Pharm.* **2011**, *8* (4), 1401–1407. <https://doi.org/10.1021/mp200243k>.
- (173) Fang, R. H.; Aryal, S.; Hu, C.-M. J.; Zhang, L. Quick Synthesis of Lipid–Polymer Hybrid Nanoparticles with Low Polydispersity Using a Single-Step Sonication Method. *Langmuir* **2010**, *26* (22), 16958–16962. <https://doi.org/10.1021/la103576a>.
- (174) Fang, R. H.; Chen, K. N. H.; Aryal, S.; Hu, C.-M. J.; Zhang, K.; Zhang, L. Large-Scale Synthesis of Lipid–Polymer Hybrid Nanoparticles Using a Multi-Inlet Vortex Reactor. *Langmuir* **2012**, *28* (39), 13824–13829. <https://doi.org/10.1021/la303012x>.
- (175) Aryal, S.; Hu, C.-M. J.; Zhang, L. Combinatorial Drug Conjugation Enables Nanoparticle Dual-Drug Delivery. *Small* **2010**, *6* (13), 1442–1448. <https://doi.org/10.1002/smll.201000631>.
- (176) Marasini, R.; Nguyen, T. D. T.; Aryal, S. Integration of Gadolinium in Nanostructure for Contrast Enhanced-Magnetic Resonance Imaging. *WIREs Nanomedicine Nanobiotechnology* **2020**, *12* (1), e1580. <https://doi.org/10.1002/wnan.1580>.
- (177) Aryal, S.; Prabakaran, M.; Pilla, S.; Gong, S. Biodegradable and Biocompatible Multi-Arm Star Amphiphilic Block Copolymer as a Carrier for Hydrophobic Drug Delivery. *Int. J. Biol. Macromol.* **2009**, *44* (4), 346–352. <https://doi.org/10.1016/j.ijbiomac.2009.01.007>.
- (178) Hu, C.-M. J.; Zhang, L.; Aryal, S.; Cheung, C.; Fang, R. H.; Zhang, L. Erythrocyte Membrane-Camouflaged Polymeric Nanoparticles as a Biomimetic Delivery Platform. *Proc. Natl. Acad. Sci.* **2011**, *108* (27), 10980–10985. <https://doi.org/10.1073/pnas.1106634108>.
- (179) Ruoslahti, E. Peptides as Targeting Elements and Tissue Penetration Devices for Nanoparticles. *Adv. Mater.* **2012**, *24* (28), 3747–3756. <https://doi.org/10.1002/adma.201200454>.
- (180) Owens, D. E.; Peppas, N. A. Opsonization, Biodistribution, and Pharmacokinetics of Polymeric Nanoparticles. *Int. J. Pharm.* **2006**, *307* (1), 93–102. <https://doi.org/10.1016/j.ijpharm.2005.10.010>.
- (181) Suk, J. S.; Xu, Q.; Kim, N.; Hanes, J.; Ensign, L. M. PEGylation as a Strategy for Improving Nanoparticle-Based Drug and Gene Delivery. *Adv. Drug Deliv. Rev.* **2016**, *99* (Pt A), 28–51. <https://doi.org/10.1016/j.addr.2015.09.012>.
- (182) J. Hu, C.-M.; H. Fang, R.; T. Luk, B.; Zhang, L. Polymeric Nanotherapeutics: Clinical Development and Advances in Stealth Functionalization Strategies. *Nanoscale* **2014**, *6* (1), 65–75. <https://doi.org/10.1039/C3NR05444F>.
- (183) Wang, R.; Deng, J.; He, D.; Yang, E.; Yang, W.; Shi, D.; Jiang, Y.; Qiu, Z.; Webster, T. J.; Shen, Y. PEGylated Hollow Gold Nanoparticles for Combined X-Ray Radiation and Photothermal Therapy in Vitro and Enhanced CT Imaging in Vivo. *Nanomedicine Nanotechnol. Biol. Med.* **2019**, *16*, 195–205. <https://doi.org/10.1016/j.nano.2018.12.005>.
- (184) Le Joncour, V.; Laakkonen, P. Seek & Destroy, Use of Targeting Peptides for Cancer Detection and Drug Delivery. *Bioorg. Med. Chem.* **2018**, *26* (10), 2797–2806. <https://doi.org/10.1016/j.bmc.2017.08.052>.

- (185) Li, J.; Chen, Y.; Kawazoe, N.; Chen, G. Ligand Density-Dependent Influence of Arginine–Glycine–Aspartate Functionalized Gold Nanoparticles on Osteogenic and Adipogenic Differentiation of Mesenchymal Stem Cells. *Nano Res.* **2018**, *11* (3), 1247–1261. <https://doi.org/10.1007/s12274-017-1738-5>.
- (186) Laakkonen, P.; Porkka, K.; Hoffman, J. A.; Ruoslahti, E. A Tumor-Homing Peptide with a Targeting Specificity Related to Lymphatic Vessels. *Nat. Med.* **2002**, *8* (7), 751–755. <https://doi.org/10.1038/nm720>.
- (187) Teesalu, T.; Sugahara, K. N.; Kotamraju, V. R.; Ruoslahti, E. C-End Rule Peptides Mediate Neuropilin-1-Dependent Cell, Vascular, and Tissue Penetration. *Proc. Natl. Acad. Sci.* **2009**, *106* (38), 16157–16162. <https://doi.org/10.1073/pnas.0908201106>.
- (188) Fogal, V.; Zhang, L.; Krajewski, S.; Ruoslahti, E. Mitochondrial/Cell-Surface Protein P32/GC1qR as a Molecular Target in Tumor Cells and Tumor Stroma. *Cancer Res.* **2008**, *68* (17), 7210–7218. <https://doi.org/10.1158/0008-5472.CAN-07-6752>.
- (189) Muta, T.; Kang, D.; Kitajima, S.; Fujiwara, T.; Hamasaki, N. P32 Protein, a Splicing Factor 2-Associated Protein, Is Localized in Mitochondrial Matrix and Is Functionally Important in Maintaining Oxidative Phosphorylation. *J. Biol. Chem.* **1997**, *272* (39), 24363–24370. <https://doi.org/10.1074/jbc.272.39.24363>.
- (190) Saha, P.; Datta, K. Multi-Functional, Multicompartmental Hyaluronan-Binding Protein 1 (HABP1/P32/GC1qR): Implication in Cancer Progression and Metastasis. *Oncotarget* **2018**, *9* (12), 10784–10807. <https://doi.org/10.18632/oncotarget.24082>.
- (191) Staton, C. A.; Kumar, I.; Reed, M. W. R.; Brown, N. J. Neuropilins in Physiological and Pathological Angiogenesis. *J. Pathol.* **2007**, *212* (3), 237–248. <https://doi.org/10.1002/path.2182>.
- (192) Yagi, M.; Uchiumi, T.; Takazaki, S.; Okuno, B.; Nomura, M.; Yoshida, S.; Kanki, T.; Kang, D. P32/GC1qR Is Indispensable for Fetal Development and Mitochondrial Translation: Importance of Its RNA-Binding Ability. *Nucleic Acids Res.* **2012**, *40* (19), 9717–9737. <https://doi.org/10.1093/nar/gks774>.
- (193) Dang, C. V. P32 (C1QBP) and Cancer Cell Metabolism: Is the Warburg Effect a Lot of Hot Air? *Mol. Cell. Biol.* **2010**, *30* (6), 1300–1302. <https://doi.org/10.1128/MCB.01661-09>.
- (194) Fogal, V.; Babic, I.; Chao, Y.; Pastorino, S.; Mukthavaram, R.; Jiang, P.; Cho, Y.-J.; Pingle, S. C.; Crawford, J. R.; Piccioni, D. E.; Kesari, S. Mitochondrial P32 Is Upregulated in Myc Expressing Brain Cancers and Mediates Glutamine Addiction. *Oncotarget* **2014**, *6* (2), 1157–1170. <https://doi.org/10.18632/oncotarget.2708>.
- (195) Fogal, V.; Richardson, A. D.; Karmali, P. P.; Scheffler, I. E.; Smith, J. W.; Ruoslahti, E. Mitochondrial P32 Protein Is a Critical Regulator of Tumor Metabolism via Maintenance of Oxidative Phosphorylation. *Mol. Cell. Biol.* **2010**, *30* (6), 1303–1318. <https://doi.org/10.1128/MCB.01101-09>.
- (196) Yenugonda, V.; Nomura, N.; Kouznetsova, V.; Tsigelny, I.; Fogal, V.; Nurmemmedov, E.; Kesari, S.; Babic, I. A Novel Small Molecule Inhibitor of P32 Mitochondrial Protein Overexpressed in Glioma. *J. Transl. Med.* **2017**, *15* (1), 210. <https://doi.org/10.1186/s12967-017-1312-7>.
- (197) von Maltzahn, G.; Ren, Y.; Park, J.-H.; Min, D.-H.; Kotamraju, V. R.; Jayakumar, J.; Fogal, V.; Sailor, M. J.; Ruoslahti, E.; Bhatia, S. N. In Vivo Tumor Cell Targeting with “Click” Nanoparticles. *Bioconjug. Chem.* **2008**, *19* (8), 1570–1578. <https://doi.org/10.1021/bc800077y>.

- (198) Kamaly, N.; Xiao, Z.; M. Valencia, P.; F. Radovic-Moreno, A.; C. Farokhzad, O. Targeted Polymeric Therapeutic Nanoparticles : Design, Development and Clinical Translation. *Chem. Soc. Rev.* **2012**, *41* (7), 2971–3010. <https://doi.org/10.1039/C2CS15344K>.
- (199) Steichen, S. D.; Caldorera-Moore, M.; Peppas, N. A. A Review of Current Nanoparticle and Targeting Moieties for the Delivery of Cancer Therapeutics. *Eur. J. Pharm. Sci.* **2013**, *48* (3), 416–427. <https://doi.org/10.1016/j.ejps.2012.12.006>.
- (200) Adhikari, U.; Scheiner, S. Preferred Configurations of Peptide–Peptide Interactions. *J. Phys. Chem. A* **2013**, *117* (2), 489–496. <https://doi.org/10.1021/jp310942u>.
- (201) Forsting, T.; C. Gottschalk, H.; Hartwig, B.; Mons, M.; A. Suhm, M. Correcting the Record: The Dimers and Trimers of Trans-N -Methylacetamide. *Phys. Chem. Chem. Phys.* **2017**, *19* (17), 10727–10737. <https://doi.org/10.1039/C6CP07989J>.
- (202) Surewicz, W. K.; Mantsch, H. H.; Chapman, D. Determination of Protein Secondary Structure by Fourier Transform Infrared Spectroscopy: A Critical Assessment. *Biochemistry* **1993**, *32* (2), 389–394. <https://doi.org/10.1021/bi00053a001>.
- (203) Geller, D. S.; Gorlick, R. Osteosarcoma: A Review of Diagnosis, Management, and Treatment Strategies. *Clin. Adv. Hematol. Oncol. HO* **2010**, *8* (10), 705–718.
- (204) Henriksen-Lacey, M.; Carregal-Romero, S.; Liz-Marzán, L. M. Current Challenges toward In Vitro Cellular Validation of Inorganic Nanoparticles. *Bioconjug. Chem.* **2017**, *28* (1), 212–221. <https://doi.org/10.1021/acs.bioconjchem.6b00514>.
- (205) Senapati, S.; Shukla, R.; Tripathi, Y. B.; Mahanta, A. K.; Rana, D.; Maiti, P. Engineered Cellular Uptake and Controlled Drug Delivery Using Two Dimensional Nanoparticle and Polymer for Cancer Treatment. *Mol. Pharm.* **2018**, *15* (2), 679–694. <https://doi.org/10.1021/acs.molpharmaceut.7b01119>.
- (206) Rayamajhi, S.; Nguyen, T. D. T.; Marasini, R.; Aryal, S. Macrophage-Derived Exosome-Mimetic Hybrid Vesicles for Tumor Targeted Drug Delivery. *Acta Biomater.* **2019**, *94*, 482–494. <https://doi.org/10.1016/j.actbio.2019.05.054>.
- (207) Seo, S.-J.; Chen, M.; Wang, H.; Kang, M. S.; Leong, K. W.; Kim, H.-W. Extra- and Intra-Cellular Fate of Nanocarriers under Dynamic Interactions with Biology. *Nano Today* **2017**, *14*, 84–99. <https://doi.org/10.1016/j.nantod.2017.04.011>.
- (208) Yu, G.; Jie, K.; Huang, F. Supramolecular Amphiphiles Based on Host–Guest Molecular Recognition Motifs. *Chem. Rev.* **2015**, *115* (15), 7240–7303. <https://doi.org/10.1021/cr5005315>.
- (209) Dehaini, D.; Fang, R. H.; Luk, B. T.; Pang, Z.; Hu, C.-M. J.; Kroll, A. V.; Yu, C. L.; Gao, W.; Zhang, L. Ultra-Small Lipid–Polymer Hybrid Nanoparticles for Tumor-Penetrating Drug Delivery. *Nanoscale* **2016**, *8* (30), 14411–14419. <https://doi.org/10.1039/C6NR04091H>.
- (210) Pang, Hong-Bo; Braun, Gary B.; Friman, Tomas; Aza-Blanc, Pedro; Ruidiaz, Manuel E.; Sugahara, Kazuki N.; Teesalu, Tabet; Ruoslahti, Erkki. An Endocytosis Pathway Initiated through Neuropilin-1 and Regulated by Nutrient Availability | Nature Communications. *Nat. Commun.* **2014**, *5* (4904). <https://doi.org/10.1038/ncomms5904>.
- (211) Dembitzer, F. R.; Kinoshita, Y.; Burstein, D.; Phelps, R. G.; Beasley, M. B.; Garcia, R.; Harpaz, N.; Jaffer, S.; Thung, S. N.; Unger, P. D.; Ghebrehiwet, B.; Peerschke, E. I. GC1qR Expression in Normal and Pathologic Human Tissues: Differential Expression in Tissues of Epithelial and Mesenchymal Origin. *J. Histochem. Cytochem.* **2012**. <https://doi.org/10.1369/0022155412440882>.

- (212) Kim, B.-C.; Hwang, H.-J.; An, H.-T.; Lee, H.; Park, J.-S.; Hong, J.; Ko, J.; Kim, C.; Lee, J.-S.; Ko, Y.-G. Antibody Neutralization of Cell-Surface GC1qR/HABP1/SF2-P32 Prevents Lamellipodia Formation and Tumorigenesis. *Oncotarget* **2016**, *7* (31), 49972–49985. <https://doi.org/10.18632/oncotarget.10267>.
- (213) Jun, Y. W.; Kim, H. R.; Reo, Y. J.; Dai, M.; Ahn, K. H. Addressing the Autofluorescence Issue in Deep Tissue Imaging by Two-Photon Microscopy: The Significance of Far-Red Emitting Dyes. *Chem. Sci.* **2017**, *8* (11), 7696–7704. <https://doi.org/10.1039/C7SC03362A>.
- (214) Hong, G.; Antaris, A. L.; Dai, H. Near-Infrared Fluorophores for Biomedical Imaging. *Nat. Biomed. Eng.* **2017**, *1* (1), 0010. <https://doi.org/10.1038/s41551-016-0010>.
- (215) Escobedo, J. O.; Rusin, O.; Lim, S.; Strongin, R. M. NIR Dyes for Bioimaging Applications. *Curr. Opin. Chem. Biol.* **2010**, *14* (1), 64–70. <https://doi.org/10.1016/j.cbpa.2009.10.022>.
- (216) He, L.; Dong, B.; Liu, Y.; Lin, W. Fluorescent Chemosensors Manipulated by Dual/Triple Interplaying Sensing Mechanisms. *Chem. Soc. Rev.* **2016**, *45* (23), 6449–6461. <https://doi.org/10.1039/C6CS00413J>.
- (217) Yan, J.; Zhu, J.; Zhou, K.; Wang, J.; Tan, H.; Xu, Z.; Chen, S.; Lu, Y.; Cui, M.; Zhang, L. Neutral Merocyanine Dyes: For in Vivo NIR Fluorescence Imaging of Amyloid- β Plaques. *Chem. Commun.* **2017**, *53* (71), 9910–9913. <https://doi.org/10.1039/C7CC05056A>.
- (218) Song, X.; Song, X.; Ren, Y.; Ren, Y.; Zhang, J.; Zhang, J.; Wang, G.; Wang, G.; Han, X.; Han, X.; Zheng, W.; Zheng, W.; Zhen, L.; Zhen, L. Targeted Delivery of Doxorubicin to Breast Cancer Cells by Aptamer Functionalized DOTAP/DOPE Liposomes. *Oncol. Rep.* **2015**, *34* (4), 1953–1960. <https://doi.org/10.3892/or.2015.4136>.
- (219) Yang, Z.; Luo, X.; Zhang, X.; Liu, J.; Jiang, Q. Targeted Delivery of 10-Hydroxycamptothecin to Human Breast Cancers by Cyclic RGD-Modified Lipid–Polymer Hybrid Nanoparticles. *Biomed. Mater.* **2013**, *8* (2), 025012. <https://doi.org/10.1088/1748-6041/8/2/025012>.
- (220) Sugahara, K. N.; Teesalu, T.; Karmali, P. P.; Kotamraju, V. R.; Agemy, L.; Girard, O. M.; Hanahan, D.; Mattrey, R. F.; Ruoslahti, E. Tissue-Penetrating Delivery of Compounds and Nanoparticles into Tumors. *Cancer Cell* **2009**, *16* (6), 510–520. <https://doi.org/10.1016/j.ccr.2009.10.013>.
- (221) Hamzah, J.; Kotamraju, V. R.; Seo, J. W.; Agemy, L.; Fogal, V.; Mahakian, L. M.; Peters, D.; Roth, L.; Gagnon, M. K. J.; Ferrara, K. W.; Ruoslahti, E. Specific Penetration and Accumulation of a Homing Peptide within Atherosclerotic Plaques of Apolipoprotein E-Deficient Mice. *Proc. Natl. Acad. Sci.* **2011**, *108* (17), 7154–7159. <https://doi.org/10.1073/pnas.1104540108>.
- (222) Kazuki N. Sugahara; Tambet Teesalu; Priya Prakash Karmali; Venkata Ramana Kotamraju; Lilach Agemy; Daniel R. Greenwald; Erkki Ruoslahti. Coadministration of a Tumor-Penetrating Peptide Enhances the Efficacy of Cancer Drugs. *Science* **2010**, *328* (5981), 1031–1035. <https://doi.org/10.1126/science.1183057>.
- (223) Peerschke, E. I. B.; Ghebrehiwet, B. CC1qR/CR and GC1qR/P33: Observations in Cancer. *Mol. Immunol.* **2014**, *61* (2), 100–109. <https://doi.org/10.1016/j.molimm.2014.06.011>.
- (224) Chan, J. M.; Zhang, L.; Tong, R.; Ghosh, D.; Gao, W.; Liao, G.; Yuet, K. P.; Gray, D.; Rhee, J.-W.; Cheng, J.; Golomb, G.; Libby, P.; Langer, R.; Farokhzad, O. C. Spatiotemporal Controlled Delivery of Nanoparticles to Injured Vasculature. *Proc. Natl. Acad. Sci.* **2010**, *107* (5), 2213–2218. <https://doi.org/10.1073/pnas.0914585107>.

- (225) Gu, W.; An, J.; Meng, H.; Yu, N.; Zhong, Y.; Meng, F.; Xu, Y.; Cornelissen, J. J. L. M.; Zhong, Z. CD44-Specific A6 Short Peptide Boosts Targetability and Anticancer Efficacy of Polymersomal Epirubicin to Orthotopic Human Multiple Myeloma. *Adv. Mater.* **2019**, *31* (46), 1904742. <https://doi.org/10.1002/adma.201904742>.
- (226) Luo, G.; Yu, X.; Jin, C.; Yang, F.; Fu, D.; Long, J.; Xu, J.; Zhan, C.; Lu, W. LyP-1-Conjugated Nanoparticles for Targeting Drug Delivery to Lymphatic Metastatic Tumors. *Int. J. Pharm.* **2010**, *385* (1), 150–156. <https://doi.org/10.1016/j.ijpharm.2009.10.014>.
- (227) Ibrahim, M. A.; Hazhirkarzar, B.; Dublin, A. B. Magnetic Resonance Imaging (MRI) Gadolinium. In *StatPearls*; StatPearls Publishing: Treasure Island (FL), 2020.
- (228) MRI in Practice, 5th Edition | Wiley <https://www.wiley.com/en-us/MRI+in+Practice%2C+5th+Edition-p-9781119392002> (accessed Apr 21, 2020).
- (229) Hahn, F. J.; Chu, W. K.; Coleman, P. E.; Anderson, J. C.; Dobry, C. A.; Imray, T. J.; Hahn, P. Y.; Lee, S. H. Artifacts and Diagnostic Pitfalls on Magnetic Resonance Imaging: A Clinical Review. *Radiol. Clin. North Am.* **1988**, *26* (4), 717–735.
- (230) Wahsner, J.; Gale, E. M.; Rodríguez-Rodríguez, A.; Caravan, P. Chemistry of MRI Contrast Agents: Current Challenges and New Frontiers. *Chem. Rev.* **2019**, *119* (2), 957–1057. <https://doi.org/10.1021/acs.chemrev.8b00363>.
- (231) Pierre, V. C.; Allen, M. J.; Caravan, P. Contrast Agents for MRI: 30+ Years and Where Are We Going? *JBIC J. Biol. Inorg. Chem.* **2014**, *19* (2), 127–131. <https://doi.org/10.1007/s00775-013-1074-5>.
- (232) Young, I. R.; Clarke, G. J.; Baffles, D. R.; Pennock, J. M.; Doyle, F. H.; Bydder, G. M. Enhancement of Relaxation Rate with Paramagnetic Contrast Agents in NMR Imaging. *J. Comput. Tomogr.* **1981**, *5* (6), 543–547. [https://doi.org/10.1016/0149-936X\(81\)90089-8](https://doi.org/10.1016/0149-936X(81)90089-8).
- (233) Thanh Nguyen, T. D.; Pitchaimani, A.; Ferrel, C.; Thakkar, R.; Aryal, S. Nano-Confinement-Driven Enhanced Magnetic Relaxivity of SPIONs for Targeted Tumor Bioimaging. *Nanoscale* **2018**, *10* (1), 284–294. <https://doi.org/10.1039/C7NR07035G>.
- (234) Morana, G.; Cugini, C.; Scatto, G.; Zanato, R.; Fusaro, M.; Dorigo, A. Use of Contrast Agents in Oncological Imaging: Magnetic Resonance Imaging. *Cancer Imaging* **2013**, *13* (3), 350–359. <https://doi.org/10.1102/1470-7330.2013.9018>.
- (235) Cervadoro, A.; Cho, M.; Key, J.; Cooper, C.; Stigliano, C.; Aryal, S.; Brazdeikis, A.; Leary, J. F.; Decuzzi, P. Synthesis of Multifunctional Magnetic NanoFlakes for Magnetic Resonance Imaging, Hyperthermia, and Targeting. *ACS Appl. Mater. Interfaces* **2014**, *6* (15), 12939–12946. <https://doi.org/10.1021/am504270c>.
- (236) Fornasiero, D.; Bellen, J. C.; Baker, R. J.; Chatterton, B. E. Paramagnetic Complexes of Manganese(II), Iron(III), and Gadolinium(III) as Contrast Agents for Magnetic Resonance Imaging. The Influence of Stability Constants on the Biodistribution of Radioactive Aminopolycarboxylate Complexes. *Invest. Radiol.* **1987**, *22* (4), 322–327. <https://doi.org/10.1097/00004424-198704000-00008>.
- (237) Bulte, J. W. M.; Kraitchman, D. L. Iron Oxide MR Contrast Agents for Molecular and Cellular Imaging. *NMR Biomed.* **2004**, *17* (7), 484–499. <https://doi.org/10.1002/nbm.924>.
- (238) Garcia, J.; Liu, S. Z.; Louie, A. Y. Biological Effects of MRI Contrast Agents: Gadolinium Retention, Potential Mechanisms and a Role for Phosphorus. *Philos. Trans. R. Soc. Math. Phys. Eng. Sci.* **2017**. <https://doi.org/10.1098/rsta.2017.0180>.
- (239) Grobner, T. Gadolinium – a Specific Trigger for the Development of Nephrogenic Fibrosing Dermopathy and Nephrogenic Systemic Fibrosis? *Nephrol. Dial. Transplant.* **2006**, *21* (4), 1104–1108. <https://doi.org/10.1093/ndt/gfk062>.

- (240) High, W. A.; Ayers, R. A.; Chandler, J.; Zito, G.; Cowper, S. E. Gadolinium Is Detectable within the Tissue of Patients with Nephrogenic Systemic Fibrosis. *J. Am. Acad. Dermatol.* **2007**, *56* (1), 21–26. <https://doi.org/10.1016/j.jaad.2006.10.047>.
- (241) Fur, M. L.; Caravan, P. The Biological Fate of Gadolinium-Based MRI Contrast Agents: A Call to Action for Bioinorganic Chemists. *Metallomics* **2019**, *11* (2), 240–254. <https://doi.org/10.1039/C8MT00302E>.
- (242) Kidney Disease Statistics for the United States | NIDDK <https://www.niddk.nih.gov/health-information/health-statistics/kidney-disease> (accessed Aug 11, 2020).
- (243) Center for Drug Evaluation and Research. Drug Safety and Availability - FDA Drug Safety Communication: FDA warns that gadolinium-based contrast agents (GBCAs) are retained in the body; requires new class warnings <https://www.fda.gov/Drugs/DrugSafety/ucm589213.htm> (accessed Jan 23, 2019).
- (244) Gadolinium-containing contrast agents | European Medicines Agency <https://www.ema.europa.eu/medicines/human/referrals/gadolinium-containing-contrast-agents> (accessed Jan 23, 2019).
- (245) Knobloch, G.; Colgan, T.; Wiens, C. N.; Wang, X.; Schubert, T.; Hernando, D.; Sharma, S. D.; Reeder, S. B. Relaxivity of Ferumoxytol at 1.5 T and 3.0 T. *Invest. Radiol.* **2018**, *53* (5), 257–263. <https://doi.org/10.1097/RLI.0000000000000434>.
- (246) Sun, C.; Lee, J. S. H.; Zhang, M. Magnetic Nanoparticles in MR Imaging and Drug Delivery. *Adv. Drug Deliv. Rev.* **2008**, *60* (11), 1252–1265. <https://doi.org/10.1016/j.addr.2008.03.018>.
- (247) Shen, Z.; Wu, A.; Chen, X. Iron Oxide Nanoparticle Based Contrast Agents for Magnetic Resonance Imaging. *Mol. Pharm.* **2017**, *14* (5), 1352–1364. <https://doi.org/10.1021/acs.molpharmaceut.6b00839>.
- (248) Sharma, P.; Holliger, N.; Pfromm, P. H.; Liu, B.; Chikan, V. Size-Controlled Synthesis of Iron and Iron Oxide Nanoparticles by the Rapid Inductive Heating Method. *ACS Omega* **2020**, *5* (31), 19853–19860. <https://doi.org/10.1021/acsomega.0c02793>.
- (249) Daldrup-Link, H. E. Ten Things You Might Not Know about Iron Oxide Nanoparticles. *Radiology* **2017**, *284* (3), 616–629. <https://doi.org/10.1148/radiol.2017162759>.
- (250) Enochs, W. S.; Petherick, P.; Bogdanova, A.; Mohr, U.; Weissleder, R. Paramagnetic Metal Scavenging by Melanin: MR Imaging. *Radiology* **1997**, *204* (2), 417–423. <https://doi.org/10.1148/radiology.204.2.9240529>.
- (251) Koepsell, H. Role of Organic Cation Transporters in Drug–Drug Interaction. *Expert Opin. Drug Metab. Toxicol.* **2015**, *11* (10), 1619–1633. <https://doi.org/10.1517/17425255.2015.1069274>.
- (252) Ye, Q.; Zhou, F.; Liu, W. Bioinspired Catecholic Chemistry for Surface Modification. *Chem. Soc. Rev.* **2011**, *40* (7), 4244–4258. <https://doi.org/10.1039/C1CS15026J>.
- (253) Li, Y.; Huang, Y.; Wang, Z.; Carniato, F.; Xie, Y.; Patterson, J. P.; Thompson, M. P.; Andolina, C. M.; Ditri, T. B.; Millstone, J. E.; Figueroa, J. S.; Rinehart, J. D.; Scadeng, M.; Botta, M.; Gianneschi, N. C. Polycatechol Nanoparticle MRI Contrast Agents. *Small* **2016**, *12* (5), 668–677. <https://doi.org/10.1002/sml.201502754>.
- (254) Iron(III) complexes as contrast agents for image enhancement in magnetic resonance imaging <http://www.freepatentsonline.com/6294152.pdf> (accessed Apr 19, 2020).
- (255) Cardoso, B. de P.; Vicente, A. I.; Ward, J. B. J.; Sebastião, P. J.; Chávez, F. V.; Barroso, S.; Carvalho, A.; Keely, S. J.; Martinho, P. N.; Calhorda, M. J. Fe(III) SalEen Derived

- Schiff Base Complexes as Potential Contrast Agents. *Inorganica Chim. Acta* **2015**, *432*, 258–266. <https://doi.org/10.1016/j.ica.2015.04.026>.
- (256) Miao, Y.; Xie, F.; Cen, J.; Zhou, F.; Tao, X.; Luo, J.; Han, G.; Kong, X.; Yang, X.; Sun, J.; Ling, J. Fe³⁺@polyDOPA-b-Polysarcosine, a T1-Weighted MRI Contrast Agent via Controlled NTA Polymerization. *ACS Macro Lett.* **2018**, *7* (6), 693–698. <https://doi.org/10.1021/acsmacrolett.8b00287>.
- (257) Fe-HBED Analogs: A Promising Class of Iron-Chelate Contrast Agents for Magnetic Resonance Imaging <https://www.hindawi.com/journals/cmami/2019/8356931/> (accessed Mar 15, 2020).
- (258) Kneepkens, E.; Fernandes, A.; Nicolay, K.; Gröll, H. Iron(III)-Based Magnetic Resonance-Imageable Liposomal T1 Contrast Agent for Monitoring Temperature-Induced Image-Guided Drug Delivery. *Invest. Radiol.* **2016**, *51* (11), 735–745. <https://doi.org/10.1097/RLI.0000000000000297>.
- (259) Marotti, M.; Schmiedl, U.; White, D.; Ramos, E.; Johnson, T.; Engelstad, B. Metal Chelates as Urographic Contrast Agents for Magnetic Resonance Imaging. *RöFo - Fortschritte Auf Dem Geb. Röntgenstrahlen Bildgeb. Verfahr.* **1987**, *147* (01), 89–93. <https://doi.org/10.1055/s-2008-1048448>.
- (260) Boehm-Sturm, P.; Haeckel, A.; Hauptmann, R.; Mueller, S.; Kuhl, C. K.; Schellenberger, E. A. Low-Molecular-Weight Iron Chelates May Be an Alternative to Gadolinium-Based Contrast Agents for T1-Weighted Contrast-Enhanced MR Imaging. *Radiology* **2017**, *286* (2), 537–546. <https://doi.org/10.1148/radiol.2017170116>.
- (261) Fan, Q.; Cheng, K.; Hu, X.; Ma, X.; Zhang, R.; Yang, M.; Lu, X.; Xing, L.; Huang, W.; Gambhir, S. S.; Cheng, Z. Transferring Biomarker into Molecular Probe: Melanin Nanoparticle as a Naturally Active Platform for Multimodality Imaging. *J. Am. Chem. Soc.* **2014**, *136* (43), 15185–15194. <https://doi.org/10.1021/ja505412p>.
- (262) Kelloff, G. J.; Krohn, K. A.; Larson, S. M.; Weissleder, R.; Mankoff, D. A.; Hoffman, J. M.; Link, J. M.; Guyton, K. Z.; Eckelman, W. C.; Scher, H. I.; O'Shaughnessy, J.; Cheson, B. D.; Sigman, C. C.; Tatum, J. L.; Mills, G. Q.; Sullivan, D. C.; Woodcock, J. The Progress and Promise of Molecular Imaging Probes in Oncologic Drug Development. *Clin. Cancer Res.* **2005**, *11* (22), 7967–7985. <https://doi.org/10.1158/1078-0432.CCR-05-1302>.
- (263) Zhang, L.; Radovic-Moreno, A. F.; Alexis, F.; Gu, F. X.; Basto, P. A.; Bagalkot, V.; Jon, S.; Langer, R. S.; Farokhzad, O. C. Co-Delivery of Hydrophobic and Hydrophilic Drugs from Nanoparticle-Aptamer Bioconjugates. *ChemMedChem* **2007**, *2* (9), 1268–1271. <https://doi.org/10.1002/cmdc.200700121>.
- (264) Nasongkla, N.; Bey, E.; Ren, J.; Ai, H.; Khemtong, C.; Guthi, J. S.; Chin, S.-F.; Sherry, A. D.; Boothman, D. A.; Gao, J. Multifunctional Polymeric Micelles as Cancer-Targeted, MRI-Ultrasensitive Drug Delivery Systems. *Nano Lett.* **2006**, *6* (11), 2427–2430. <https://doi.org/10.1021/nl061412u>.
- (265) Chan, J. M.; Zhang, L.; Yuet, K. P.; Liao, G.; Rhee, J.-W.; Langer, R.; Farokhzad, O. C. PLGA-Lecithin-PEG Core-Shell Nanoparticles for Controlled Drug Delivery. *Biomaterials* **2009**, *30* (8), 1627–1634. <https://doi.org/10.1016/j.biomaterials.2008.12.013>.
- (266) Aryal, S.; Bhattarai, S. R.; K.c., R. B.; Khil, M. S.; Lee, D.-R.; Kim, H. Y. Carbon Nanotubes Assisted Biomimetic Synthesis of Hydroxyapatite from Simulated Body Fluid. *Mater. Sci. Eng. A* **2006**, *426* (1), 202–207. <https://doi.org/10.1016/j.msea.2006.04.004>.

- (267) Cüneyt Tas, A. Synthesis of Biomimetic Ca-Hydroxyapatite Powders at 37°C in Synthetic Body Fluids. *Biomaterials* **2000**, *21* (14), 1429–1438. [https://doi.org/10.1016/S0142-9612\(00\)00019-3](https://doi.org/10.1016/S0142-9612(00)00019-3).
- (268) Jun, Y.; Lee, J.-H.; Cheon, J. Chemical Design of Nanoparticle Probes for High-Performance Magnetic Resonance Imaging. *Angew. Chem. Int. Ed.* **2008**, *47* (28), 5122–5135. <https://doi.org/10.1002/anie.200701674>.
- (269) Thomsen, H. S.; Morcos, S. K. Risk of Contrast-Medium-Induced Nephropathy in High-Risk Patients Undergoing MDCT – A Pooled Analysis of Two Randomized Trials. *Eur. Radiol.* **2008**, *19* (4), 891. <https://doi.org/10.1007/s00330-008-1206-4>.
- (270) Davenport, M. S.; Cohan, R. H.; Caoili, E. M.; Ellis, J. H. Repeat Contrast Medium Reactions in Premedicated Patients: Frequency and Severity. *Radiology* **2009**, *253* (2), 372–379. <https://doi.org/10.1148/radiol.2532090465>.
- (271) Kooiman, J.; Pasha, S. M.; Zondag, W.; Sijpkens, Y. W. J.; van der Molen, A. J.; Huisman, M. V.; Dekkers, O. M. Meta-Analysis: Serum Creatinine Changes Following Contrast Enhanced CT Imaging. *Eur. J. Radiol.* **2012**, *81* (10), 2554–2561. <https://doi.org/10.1016/j.ejrad.2011.11.020>.
- (272) McDonald, R. J.; McDonald, J. S.; Kallmes, D. F.; Jentoft, M. E.; Paolini, M. A.; Murray, D. L.; Williamson, E. E.; Eckel, L. J. Gadolinium Deposition in Human Brain Tissues after Contrast-Enhanced MR Imaging in Adult Patients without Intracranial Abnormalities. *Radiology* **2017**, *285* (2), 546–554. <https://doi.org/10.1148/radiol.2017161595>.
- (273) Murata, N.; Gonzalez-Cuyar, L. F.; Murata, K.; Fligner, C.; Dills, R.; Hippe, D.; Maravilla, K. R. Macrocyclic and Other Non-Group 1 Gadolinium Contrast Agents Deposit Low Levels of Gadolinium in Brain and Bone Tissue: Preliminary Results From 9 Patients With Normal Renal Function. *Invest. Radiol.* **2016**, *51* (7), 447–453. <https://doi.org/10.1097/RLI.0000000000000252>.
- (274) Research, C. for D. E. and. FDA Drug Safety Communication: FDA Identifies No Harmful Effects to Date with Brain Retention of Gadolinium-Based Contrast Agents for MRIs; Review to Continue. *FDA* **2019**.
- (275) NCHR Report: The Health Risks of MRIs with Gadolinium-Based Contrast Agents. *National Center for Health Research*, 2019.
- (276) Winterbourn, C. C. Toxicity of Iron and Hydrogen Peroxide: The Fenton Reaction. *Toxicol. Lett.* **1995**, *82–83*, 969–974. [https://doi.org/10.1016/0378-4274\(95\)03532-X](https://doi.org/10.1016/0378-4274(95)03532-X).
- (277) Welch, K. D.; Davis, T. Z.; Van Eden, M. E.; Aust, S. D. Deleterious Iron-Mediated Oxidation of Biomolecules 1 This Article Is Part of a Series of Reviews on “Iron and Cellular Redox Status.” The Full List of Papers May Be Found on the Homepage of the Journal. 6 6Guest Editor: Mario Comporti. *Free Radic. Biol. Med.* **2002**, *32* (7), 577–583. [https://doi.org/10.1016/S0891-5849\(02\)00760-8](https://doi.org/10.1016/S0891-5849(02)00760-8).
- (278) Snyder, E. M.; Asik, D.; Abozeid, S. M.; Burgio, A.; Bateman, G.; Turowski, S. G.; Spornyak, J. A.; Morrow, J. R. A Class of FeIII Macrocyclic Complexes with Alcohol Donor Groups as Effective T1 MRI Contrast Agents. *Angew. Chem. Int. Ed.* **2020**, *59* (6), 2414–2419. <https://doi.org/10.1002/anie.201912273>.
- (279) Lee, B. P.; Messersmith, P. b.; Israelachvili, J. n.; Waite, J. h. Mussel-Inspired Adhesives and Coatings. *Annu. Rev. Mater. Res.* **2011**, *41* (1), 99–132. <https://doi.org/10.1146/annurev-matsci-062910-100429>.

- (280) Zeng, H.; Hwang, D. S.; Israelachvili, J. N.; Waite, J. H. Strong Reversible Fe³⁺-Mediated Bridging between Dopa-Containing Protein Films in Water. *Proc. Natl. Acad. Sci.* **2010**, *107* (29), 12850–12853. <https://doi.org/10.1073/pnas.1007416107>.
- (281) Ju, K.-Y.; Lee, J. W.; Im, G. H.; Lee, S.; Pyo, J.; Park, S. B.; Lee, J. H.; Lee, J.-K. Bio-Inspired, Melanin-Like Nanoparticles as a Highly Efficient Contrast Agent for T1-Weighted Magnetic Resonance Imaging. *Biomacromolecules* **2013**, *14* (10), 3491–3497. <https://doi.org/10.1021/bm4008138>.
- (282) Starmans, L. W. E.; Hummelink, M. A. P. M.; Rossin, R.; Kneepkens, E. C. M.; Lamerichs, R.; Donato, K.; Nicolay, K.; Gröll, H. 89Zr- and Fe-Labeled Polymeric Micelles for Dual Modality PET and T1-Weighted MR Imaging. *Adv. Healthc. Mater.* **2015**, *4* (14), 2137–2145. <https://doi.org/10.1002/adhm.201500414>.
- (283) Caravan, P.; Farrar, C. T.; Frullano, L.; Uppal, R. Influence of Molecular Parameters and Increasing Magnetic Field Strength on Relaxivity of Gadolinium- and Manganese-Based T1 Contrast Agents. *Contrast Media Mol. Imaging* **2009**, *4* (2), 89–100. <https://doi.org/10.1002/cmml.267>.
- (284) Caravan, P. Strategies for Increasing the Sensitivity of Gadolinium Based MRI Contrast Agents. *Chem. Soc. Rev.* **2006**, *35* (6), 512–523. <https://doi.org/10.1039/B510982P>.
- (285) Richardson, N.; Davies, J. A.; Radüchel, B. Iron(III)-Based Contrast Agents for Magnetic Resonance Imaging. *Polyhedron* **1999**, *18* (19), 2457–2482. [https://doi.org/10.1016/S0277-5387\(99\)00151-5](https://doi.org/10.1016/S0277-5387(99)00151-5).
- (286) Aryal, S.; Stigliano, C.; Key, J.; Ramirez, M.; Anderson, J.; Karmonik, C.; Fung, S.; Decuzzi, P. Paramagnetic Gd³⁺ Labeled Red Blood Cells for Magnetic Resonance Angiography. *Biomaterials* **2016**, *98*, 163–170. <https://doi.org/10.1016/j.biomaterials.2016.05.002>.

Appendix A - Supporting information from Chapter 2

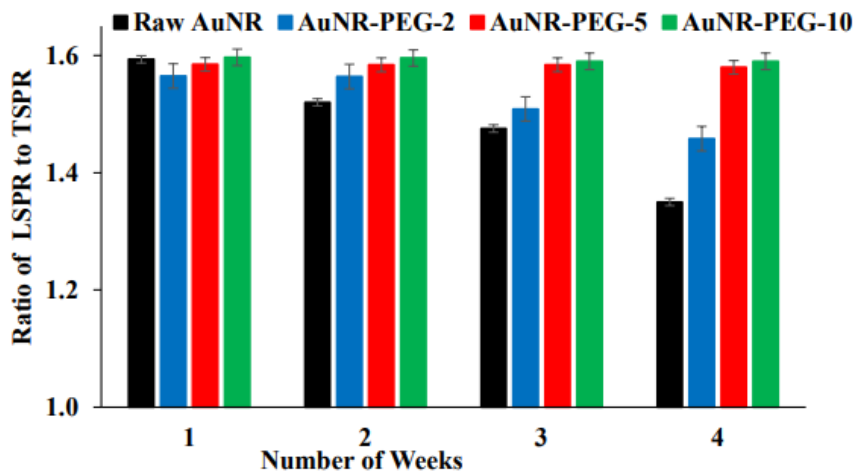


Figure 2.S1. Stability of Raw and PEG-functionalized AuNRs at 4 °C. The ratio of maximum longitudinal surface plasmon resonance (LSPR) to the transverse surface plasmon resonance (TSPR) of both Raw and PEG-functionalized AuNRs was taken to calculate aspect ratio. The stability was observed while storing at 4°C and the surface plasmon resonance was measured by UV-Vis spectrum over the period. This graph shows higher stability of PEG functionalization of AuNRs as compared to that of Raw AuNR.

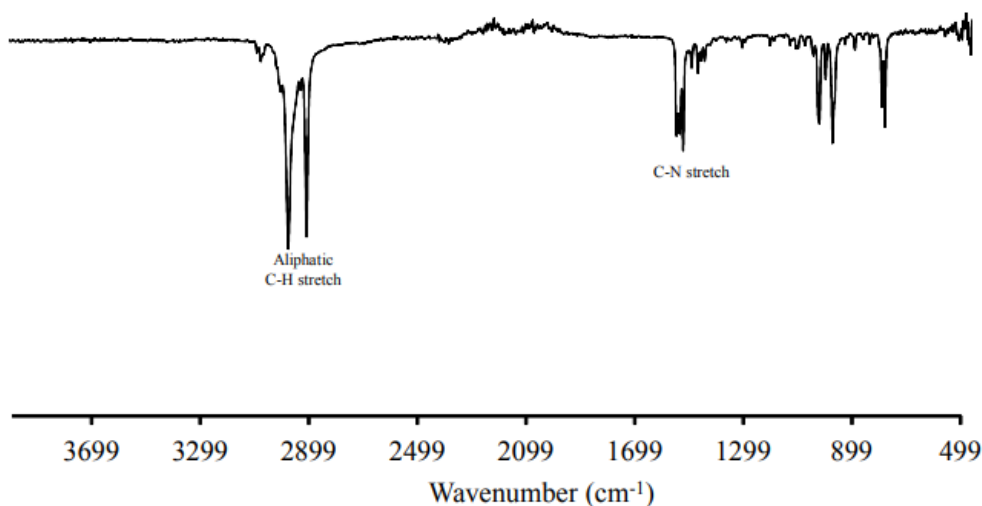


Figure 2.S2. FT-IR spectrum of Cetyltrimethylammonium bromide (CTAB).

Appendix B - Supporting information from Chapter 4

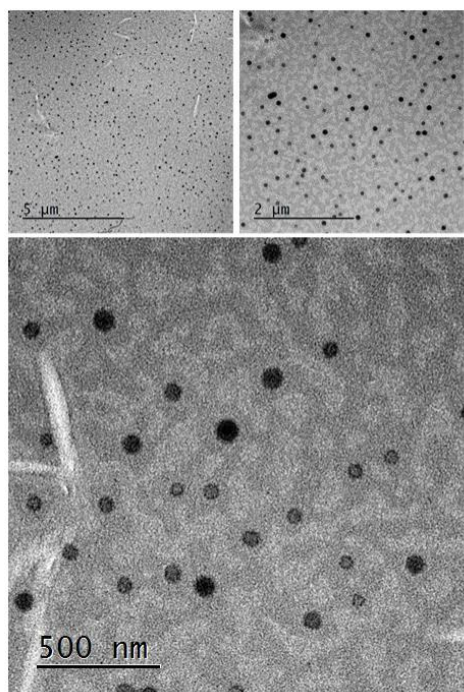


Figure 4.S1. Representative transmission electron microscopy images of LyP-1 NPs with different magnifications.

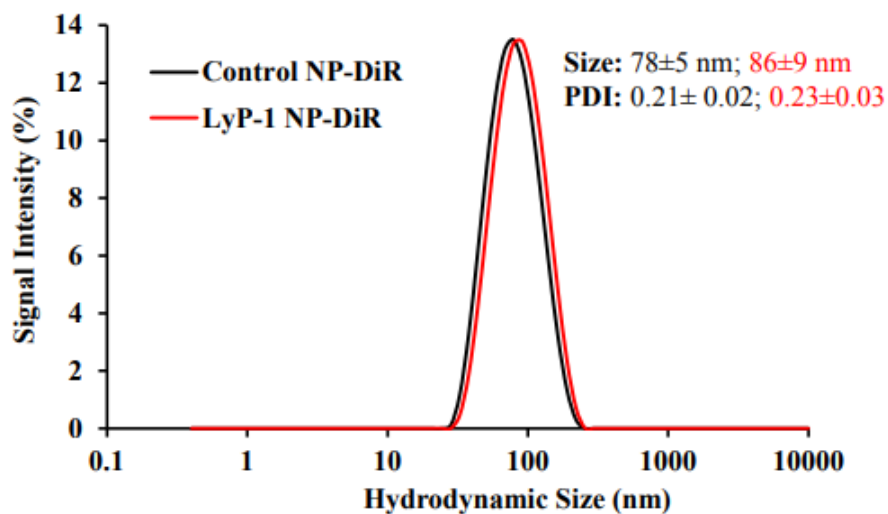


Figure 4.S2. Dynamic light scattering showing the average hydrodynamic size of Control NP-DiR and LyP-1 NP-DiR.

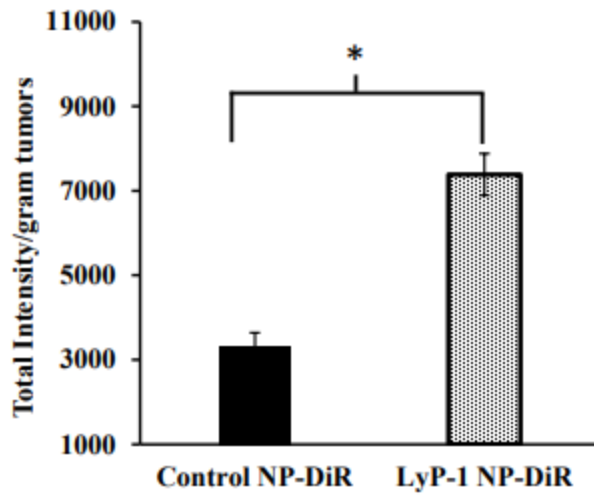


Figure 4.S3. Quantification of tumor accumulation of Control NP-DiR and LyP-1 NP-DiR after 48 hr post-injection. p value= 0.0169* student F-test). Data represent mean \pm SD, $n = 3$.

Appendix C - Supporting information from Chapter 5

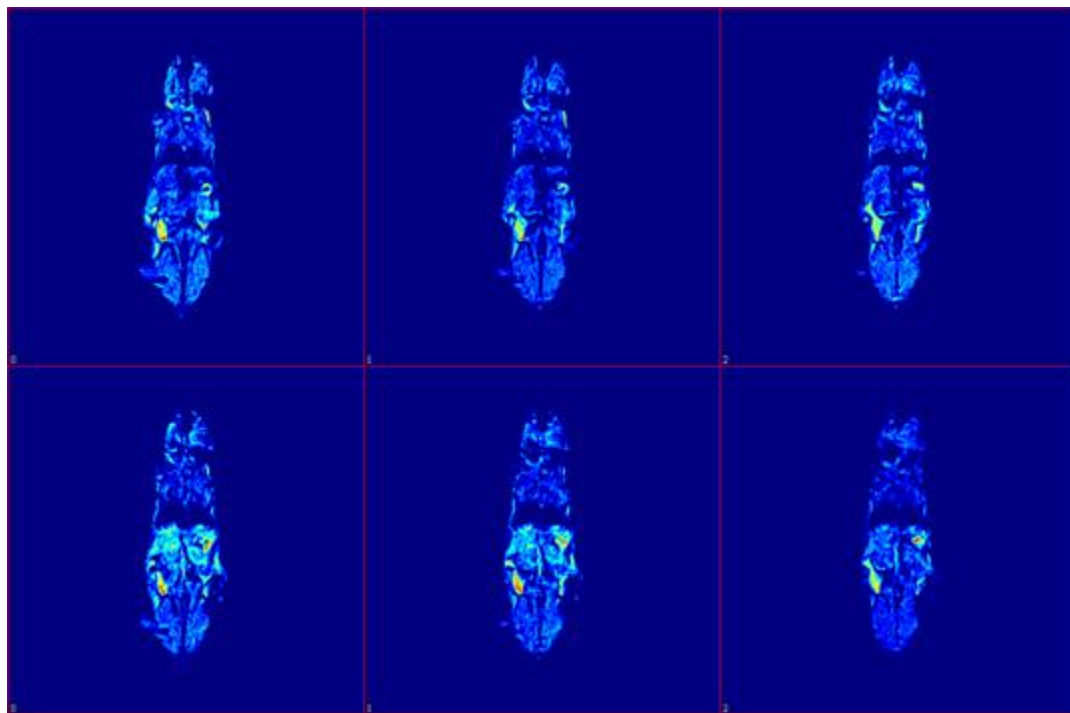


Figure 5.S1. Coronal slices (1, 2, 3 from left to right) of pre-injection (upper panel) and at-injection (lower panel) of Fe-PLGA NPs showing the contrast enhancement of in abdominal aorta in mice during dynamic imaging at 3 T.

Appendix D - List of abbreviation

Name	Abbreviation
1,1'-Diocetadecyl-3,3,3',3'-Tetramethylindotricarbocyanine Iodide	DiR
1,2-distearoyl-sn-glycero-3-phosphoethanolamine	DSPE
1,2-distearoyl-sn-glycero-3-phosphoethanolamine-N-[carboxy(polyethylene glycol)-2000] (sodium salt)	DSPE-PEG-COOH
1-ethyl-3-(3-dimethylaminopropyl)carbodiimide hydrochloride	EDC
American Type Cell Culture	ATCC
3-(4,5-dimethylthiazol-2-yl)-2,5-diphenyl tetrazolium bromide	MTT
4',6-diamidino-2-phenylindole	DAPI
Alendronic acid	ALE
Alendronic acid conjugated lipid	ALE-lipid
Alpha Minimum Essential Medium	α -MEM
Analysis of variance	ANOVA
dimethyl sulfoxide	DMSO
Bicinchoninic acid assay	BCA
1,2-distearoyl-sn-glycero-3-phosphoglycerol, sodium salt	DSPG
Carbon dioxide	CO ₂
Chemical Abstract Service	CAS
Nanometer	nm
Corrected total cell fluorescence	CTCF
Contrast-enhanced MRI	Ce-MRI
Computed Tomography	CT
Confocal Laser Scanning Microscope	CLSM
Contrast-enhanced magnetic resonance imaging	Ce-MRI
Computed tomography	CT
Positron emission tomography	PET
Dimethyl sulfoxide	DMSO
Doxorubicin	DOX
Dulbecco's Modified Eagle Medium	DMEM
Dynamic Light Scattering	DLS
Echo time	TE
Tumor microenvironment	TME
Enhanced Permeability and Retention effect	EPR effect
Fast slow angle shot	FLASH
Fetal bovine serum	FBS
Field of view	FOV
Area under the curve	AUC
Transforming growth factor- β	TGF- β

Fluorescence-activated cell sorting	FACS
Food and Drug Administration	FDA
Fourier-transform infrared spectroscopy	FT-IR
Gadobenate dimeglumine	Gd-BOPTA
Ferric chloride	FeCl ₃
Gadolinium	Gd
Gadolinium (III) acetate hydrate	Gd(OAc) ₃
Gadolinium-based contrast agent	GBCA
Gadolinium lipid	Gd-lipid or Gd-L
Gadopentetate dimeglumine	Gd-DTPA
Transverse surface plasmon resonance	TSPR
Gold nanorods	AuNRs
Photothermal Therapy	PTT
Kilo Dalton	kDa
Gold chloride trihydrate	HAuCl ₄ .3H ₂ O
Cetyl tri-methyl ammonium bromide	CTAB
Polyethylene glycol carboxylic thiols	HOOC-PEG-SH
Hydrochloric acid	HCl
Sodium borohydride	NaBH ₄
Nitric acid	HNO ₃
Inductively coupled plasma mass spectrometry	ICP-MS
Injected dose	ID
Institutional Animal Care and Use Committee	IACUC
Institutional Biosafety Committee	IBC
Centimeter	cm
Iron	Fe
Micro gram	μg
Mili liter	mL
Longitudinal relaxation time	T ₁
Longitudinal relaxivity	r ₁
Longitudinal surface plasmon resonance	LSPR
Magnetic Resonance Imaging	MRI
positron emission tomography	PET
Molar	M
Molecular weight	MW
Molecular weight cut off	MWCO
Mononuclear phagocyte system	MPS
Nanoparticle	NP
Micro liter	μL
Silver Nitrate	AgNO ₃

Near-infrared	NIR
Nephrogenic systemic fibrosis	NSF
N-hydroxysuccinimide	NHS
Phosphate buffered saline	PBS
Poly(lactic-co-glycolic acid)	PLGA
Polydispersity index	PDI
Polyethylene glycol	PEG
Polyethylene glycolated	PEGylated
Repetition time	TR
Reticuloendothelial system	RES
Rhodamine dye	RhB
Superparamagnetic iron oxide nanoparticle	SPION
Transmission Electron Micrograph	TEM
Transverse relaxation time	T ₂
Transverse relaxivity	r ₂
Triethylamine	TEA
Ultraviolet-visible spectroscopy	UV-Vis
United State of America	USA
Forward-looking Infrared	FLIR

Appendix E - List of publications

1. **Marasini, R.**, Nguyen, T. D.T, Rayamajhi, S., & Aryal, S. (2020). Synthesis and Characterization of a Tumor-seeking LyP-1 Peptide Integrated Lipid–polymer Composite Nanoparticle. *Materials Advances*, **1**, 469-480. (**Chapter 4**)
2. Rayamajhi, S., **Marasini, R.**, Nguyen, T. D.T & Aryal, S. (2020). Strategic reconstruction of macrophage-derived extracellular vesicles as a magnetic resonance imaging contrast agent. *Biomaterials Science*, **8**, 2887-2904.
3. Nguyen TDT, **Marasini R**, Rayamajhi, S., Aparicio, C., Biller, D., & Aryal S. (2020) Erythrocyte membrane concealed paramagnetic polymeric nanoparticle for contrast-enhanced magnetic resonance imaging. *Nanoscale*, **12** (6), 4137-4149.
4. **Marasini, R.**, Nguyen, T. D.T & Aryal, S. (2020). Integration of gadolinium in nanostructure for contrast-enhanced magnetic resonance imaging. *Wiley Interdisciplinary Reviews: Nanomedicine and Nanobiotechnology*, **12**(1), e1580.
5. Rayamajhi, S., Marchitto, J., Nguyen, T. D.T, **Marasini, R.**, Celia, C., & Aryal, S. (2020). pH-responsive cationic liposome for endosomal escape mediated drug delivery. *Colloids and Surfaces B: Biointerfaces*, 110804.
6. Rayamajhi, S., Nguyen, T. D.T, **Marasini, R.** & Aryal, S. (2019). Macrophage-derived exosome-mimetic hybrid vesicles for tumor-targeted drug delivery. *Acta Biomaterialia*, **94**, 482-494.
7. Abello J, Nguyen TDT, **Marasini R**, Aryal S, & Weiss ML. (2019). Biodistribution of Gadolinium- and Near Infrared-Labeled Human Umbilical Cord Mesenchymal Stromal Cell-Derived Exosomes in Tumor Bearing Mice. *Theranostics*, **9**(8), 2325-2345.
8. Pitchaimani, A., Nguyen, T. D. T., **Marasini, R.**, Eliyapura, A., Azizi, T., Jaber-Douraki, M., & Aryal, S. (2019). Biomimetic Natural Killer Membrane Camouflaged Polymeric Nanoparticle for Targeted Bioimaging. *Advanced Functional Materials*, 1806817.
9. **Marasini, R.**, Pitchaimani, A., Nguyen, T. D.T, Comer, J., & Aryal, S. (2018). Influence of Polyethylene Glycol Passivation on the Surface Plasmon Resonance Induced Photothermal Properties of Gold Nanorods. *Nanoscale*, **10**(28), 13684-12693. (**Chapter -2**)
10. **Marasini, R.** & Joshi, S. (2013) Antibacterial and antifungal activity of medicinal orchids growing in Nepal. *Journal of Nepal Chemical Society*, **29**,104-109.

Appendix F - Copyright permissions



Marketplace™

Royal Society of Chemistry - License Terms and Conditions

This is a License Agreement between Ramesh Marasini/ Kansas State University ("You") and Royal Society of Chemistry ("Publisher") provided by Copyright Clearance Center ("CCC"). The license consists of your order details, the terms and conditions provided by Royal Society of Chemistry, and the CCC terms and conditions.

All payments must be made in full to CCC.

Order Date	10-Aug-2020	Type of Use	Republish in a thesis/dissertation
Order license ID	1054501-1	Publisher	RSC Pub
ISSN	2040-3372	Portion	Chapter/article

LICENSED CONTENT

Publication Title	Nanoscale	Country	United Kingdom of Great Britain and Northern Ireland
Author/Editor	National Center for Nanoscience and Technology., Royal Society of Chemistry (Great Britain)	Rightsholder	Royal Society of Chemistry
Date	12/31/2008	Publication Type	e-Journal
Language	English	URL	http://www.rsc.org/Publishing/Journals/NR/index.asp

REQUEST DETAILS

Portion Type	Chapter/article	Rights Requested	Main product and any product related to main product
Page range(s)	13684-13693	Distribution	United States
Total number of pages	10	Translation	Original language of publication
Format (select all that apply)	Electronic	Copies for the disabled?	No
Who will republish the content?	Academic institution	Minor editing privileges?	No
Duration of Use	Life of current edition	Incidental promotional use?	No
Lifetime Unit Quantity	Up to 499	Currency	USD

NEW WORK DETAILS

Title	Design Strategies and application of stimuli-responsive nanoparticles for cancer diagnosis and therapy	Institution name	Kansas State University
Instructor name	Ramesh Marasini	Expected presentation date	2020-09-02

ADDITIONAL DETAILS

REUSE CONTENT DETAILS

Title, description or numeric reference of the portion(s)	Entire content of paper to be used as a dissertation chapter	Title of the article/chapter the portion is from	The influence of polyethylene glycol passivation on the surface plasmon resonance induced photothermal properties of gold nanorods
Editor of portion(s)	N/A		
Volume of serial or monograph	10		
Page or page range of portion	13684-13693	Author of portion(s)	N/A
		Issue, if republishing an article from a serial	N/A
		Publication date of portion	2008-12-31

PUBLISHER SPECIAL TERMS AND CONDITIONS

The Royal Society of Chemistry (RSC) hereby grants permission for the use of your paper(s) specified below in the printed and microfilm version of your thesis. You may also make available the PDF version of your paper(s) that the RSC sent to the corresponding author(s) of your paper(s) upon publication of the paper(s) in the following ways: in your thesis via any website that your university may have for the deposition of theses, via your university's Intranet or via your own personal website. We are however unable to grant you permission to include the PDF version of the paper(s) on its own in your institutional repository. The Royal Society of Chemistry is a signatory to the STM Guidelines on Permissions (available on request). Please note that if the material specified below or any part of it appears with credit or acknowledgement to a third party then you must also secure permission from that third party before reproducing that material. Please ensure that the thesis states the following: Reproduced by permission of The Royal Society of Chemistry and include a link to the paper on the Royal Society of Chemistry's website. Please ensure that your co-authors are aware that you are including the paper in your thesis.

CCC Republication Terms and Conditions

1. Description of Service; Defined Terms. This Republication License enables the User to obtain licenses for republication of one or more copyrighted works as described in detail on the relevant Order Confirmation (the "Work(s)"). Copyright Clearance Center, Inc. ("CCC") grants licenses through the Service on behalf of the rightsholder identified on the Order Confirmation (the "Rightsholder"). "Republishing", as used herein, generally means the inclusion of a Work, in whole or in part, in a new work or works, also as described on the Order Confirmation. "User", as used herein, means the person or entity making such republication.
2. The terms set forth in the relevant Order Confirmation, and any terms set by the Rightsholder with respect to a particular Work, govern the terms of use of Works in connection with the Service. By using the Service, the person transacting for a republication license on behalf of the User represents and warrants that he/she/it (a) has been duly authorized by the User to accept, and hereby does accept, all such terms and conditions on behalf of User, and (b) shall inform User of all such terms and conditions. In the event such person is a "freelancer" or other third party independent of User and CCC, such party shall be deemed jointly a "User" for purposes of these terms and conditions. In any event, User shall be deemed to have accepted and agreed to all such terms and conditions if User republishes the Work in any fashion.
3. Scope of License; Limitations and Obligations.
 - 3.1. All Works and all rights therein, including copyright rights, remain the sole and exclusive property of the Rightsholder. The license created by the exchange of an Order Confirmation (and/or any invoice) and payment by User of the full amount set forth on that document includes only those rights expressly set

forth in the Order Confirmation and in these terms and conditions, and conveys no other rights in the Work(s) to User. All rights not expressly granted are hereby reserved.

- 3.2. General Payment Terms: You may pay by credit card or through an account with us payable at the end of the month. If you and we agree that you may establish a standing account with CCC, then the following terms apply: Remit Payment to: Copyright Clearance Center, 29118 Network Place, Chicago, IL 60673-1291. Payments Due: Invoices are payable upon their delivery to you (or upon our notice to you that they are available to you for downloading). After 30 days, outstanding amounts will be subject to a service charge of 1-1/2% per month or, if less, the maximum rate allowed by applicable law. Unless otherwise specifically set forth in the Order Confirmation or in a separate written agreement signed by CCC, invoices are due and payable on "net 30" terms. While User may exercise the rights licensed immediately upon issuance of the Order Confirmation, the license is automatically revoked and is null and void, as if it had never been issued, if complete payment for the license is not received on a timely basis either from User directly or through a payment agent, such as a credit card company.
- 3.3. Unless otherwise provided in the Order Confirmation, any grant of rights to User (i) is "one-time" (including the editions and product family specified in the license), (ii) is non-exclusive and non-transferable and (iii) is subject to any and all limitations and restrictions (such as, but not limited to, limitations on duration of use or circulation) included in the Order Confirmation or invoice and/or in these terms and conditions. Upon completion of the licensed use, User shall either secure a new permission for further use of the Work(s) or immediately cease any new use of the Work(s) and shall render inaccessible (such as by deleting or by removing or severing links or other locators) any further copies of the Work (except for copies printed on paper in accordance with this license and still in User's stock at the end of such period).
- 3.4. In the event that the material for which a republication license is sought includes third party materials (such as photographs, illustrations, graphs, inserts and similar materials) which are identified in such material as having been used by permission, User is responsible for identifying, and seeking separate licenses (under this Service or otherwise) for, any of such third party materials; without a separate license, such third party materials may not be used.
- 3.5. Use of proper copyright notice for a Work is required as a condition of any license granted under the Service. Unless otherwise provided in the Order Confirmation, a proper copyright notice will read substantially as follows: "Republished with permission of [Rightsholder's name], from [Work's title, author, volume, edition number and year of copyright]; permission conveyed through Copyright Clearance Center, Inc. " Such notice must be provided in a reasonably legible font size and must be placed either immediately adjacent to the Work as used (for example, as part of a by-line or footnote but not as a separate electronic link) or in the place where substantially all other credits or notices for the new work containing the republished Work are located. Failure to include the required notice results in loss to the Rightsholder and CCC, and the User shall be liable to pay liquidated damages for each such failure equal to twice the use fee specified in the Order Confirmation, in addition to the use fee itself and any other fees and charges specified.
- 3.6. User may only make alterations to the Work if and as expressly set forth in the Order Confirmation. No Work may be used in any way that is defamatory, violates the rights of third parties (including such third parties' rights of copyright, privacy, publicity, or other tangible or intangible property), or is otherwise illegal, sexually explicit or obscene. In addition, User may not conjoin a Work with any other material that may result in damage to the reputation of the Rightsholder. User agrees to inform CCC if it becomes aware of any infringement of any rights in a Work and to cooperate with any reasonable request of CCC or the Rightsholder in connection therewith.

4. Indemnity. User hereby indemnifies and agrees to defend the Rightsholder and CCC, and their respective employees and directors, against all claims, liability, damages, costs and expenses, including legal fees and expenses, arising out of any use of a Work beyond the scope of the rights granted herein, or any use of a Work which has been altered in any unauthorized way by User, including claims of defamation or infringement of rights of copyright, publicity, privacy or other tangible or intangible property.
5. Limitation of Liability. UNDER NO CIRCUMSTANCES WILL CCC OR THE RIGHTSHOLDER BE LIABLE FOR ANY DIRECT, INDIRECT, CONSEQUENTIAL OR INCIDENTAL DAMAGES (INCLUDING WITHOUT LIMITATION DAMAGES FOR LOSS OF BUSINESS PROFITS OR INFORMATION, OR FOR BUSINESS INTERRUPTION) ARISING OUT OF THE USE OR INABILITY TO USE A WORK, EVEN IF ONE OF THEM HAS BEEN ADVISED OF THE POSSIBILITY OF SUCH DAMAGES. In any event, the total liability of the Rightsholder and CCC (including their respective employees and directors) shall not exceed the total amount actually paid by User for this license. User assumes full liability for the actions and omissions of its principals, employees, agents, affiliates, successors and assigns.
6. Limited Warranties. THE WORK(S) AND RIGHT(S) ARE PROVIDED "AS IS". CCC HAS THE RIGHT TO GRANT TO USER THE RIGHTS GRANTED IN THE ORDER CONFIRMATION DOCUMENT. CCC AND THE RIGHTSHOLDER DISCLAIM ALL OTHER WARRANTIES RELATING TO THE WORK(S) AND RIGHT(S), EITHER EXPRESS OR IMPLIED, INCLUDING WITHOUT LIMITATION IMPLIED WARRANTIES OF MERCHANTABILITY OR FITNESS FOR A PARTICULAR PURPOSE. ADDITIONAL RIGHTS MAY BE REQUIRED TO USE ILLUSTRATIONS, GRAPHS, PHOTOGRAPHS, ABSTRACTS, INSERTS OR OTHER PORTIONS OF THE WORK (AS OPPOSED TO THE ENTIRE WORK) IN A MANNER CONTEMPLATED BY USER; USER UNDERSTANDS AND AGREES THAT NEITHER CCC NOR THE RIGHTSHOLDER MAY HAVE SUCH ADDITIONAL RIGHTS TO GRANT.
7. Effect of Breach. Any failure by User to pay any amount when due, or any use by User of a Work beyond the scope of the license set forth in the Order Confirmation and/or these terms and conditions, shall be a material breach of the license created by the Order Confirmation and these terms and conditions. Any breach not cured within 30 days of written notice thereof shall result in immediate termination of such license without further notice. Any unauthorized (but licensable) use of a Work that is terminated immediately upon notice thereof may be liquidated by payment of the Rightsholder's ordinary license price therefor; any unauthorized (and unlicensable) use that is not terminated immediately for any reason (including, for example, because materials containing the Work cannot reasonably be recalled) will be subject to all remedies available at law or in equity, but in no event to a payment of less than three times the Rightsholder's ordinary license price for the most closely analogous licensable use plus Rightsholder's and/or CCC's costs and expenses incurred in collecting such payment.
8. Miscellaneous.
 - 8.1. User acknowledges that CCC may, from time to time, make changes or additions to the Service or to these terms and conditions, and CCC reserves the right to send notice to the User by electronic mail or otherwise for the purposes of notifying User of such changes or additions; provided that any such changes or additions shall not apply to permissions already secured and paid for.
 - 8.2. Use of User-related information collected through the Service is governed by CCC's privacy policy, available online here:<https://marketplace.copyright.com/rs-ui-web/mp/privacy-policy>

- 8.3. The licensing transaction described in the Order Confirmation is personal to User. Therefore, User may not assign or transfer to any other person (whether a natural person or an organization of any kind) the license created by the Order Confirmation and these terms and conditions or any rights granted hereunder; provided, however, that User may assign such license in its entirety on written notice to CCC in the event of a transfer of all or substantially all of User's rights in the new material which includes the Work(s) licensed under this Service.
- 8.4. No amendment or waiver of any terms is binding unless set forth in writing and signed by the parties. The Rightsholder and CCC hereby object to any terms contained in any writing prepared by the User or its principals, employees, agents or affiliates and purporting to govern or otherwise relate to the licensing transaction described in the Order Confirmation, which terms are in any way inconsistent with any terms set forth in the Order Confirmation and/or in these terms and conditions or CCC's standard operating procedures, whether such writing is prepared prior to, simultaneously with or subsequent to the Order Confirmation, and whether such writing appears on a copy of the Order Confirmation or in a separate instrument.
- 8.5. The licensing transaction described in the Order Confirmation document shall be governed by and construed under the law of the State of New York, USA, without regard to the principles thereof of conflicts

8/10/2020 <https://marketplace.copyright.com/rs-ui-web/mp/license/1c28560f-c985-4072-8679-15f2c8f21e96/84033f65-0c11-4c0b-a976-10318b04989f>
of law. Any case, controversy, suit, action, or proceeding arising out of, in connection with, or related to such licensing transaction shall be brought, at CCC's sole discretion, in any federal or state court located in the County of New York, State of New York, USA, or in any federal or state court whose geographical jurisdiction covers the location of the Rightsholder set forth in the Order Confirmation. The parties expressly submit to the personal jurisdiction and venue of each such federal or state court. If you have any comments or questions about the Service or Copyright Clearance Center, please contact us at 978-750-8400 or send an e-mail to support@copyright.com.

v 1.1